Hinrich Grothe

DIPLOMARBEIT

Analytical Characterization of Macromolecular Ice Nuclei from Birch Pollen Grains

Ausgeführt am

Institut für Materialchemie,

Institut für Chemische Technologien und Analytik

der Technischen Universität Wien

unter Anleitung von

Ao.Univ.Prof. Dipl.-Chem. Dr.rer.nat. Hinrich Grothe,

Univ.Prof. Mag.pharm. Dr.rer.nat. Günter Allmaier,

Associate Prof. Mag.rer.nat. Dr.rer.nat. Martina Marchetti-Deschmann

durch

Teresa Magdalena Seifried BSc.

Singerstaße 30

1010 Wien

25.10.2017

Teresa Magdalena Seifried

Abstract

In the atmosphere, liquid water can be supercooled down to -38°C, since freezing does not only depend on thermodynamics but is steered by kinetics. The phase transition from liquid to solid occurs either homogenously where just water molecules are involved or heterogeneously, catalyzed by foreign particles, so-called ice nuclei (IN). IN trigger the formation of ice clouds, which are of interest due to their importance for climate and weather. The influence of biological IN on atmospheric processes is still not fully understood and many questions are still remaining. How exactly do biological IN (BIN) influence cloud formation? How does the transport process of BIN into the free troposphere work? Which chemical properties and structures do BIN have? This thesis focuses on the later of these questions. *Betula pendula* birch pollen, known to be ice nucleation active, were analyzed to characterize their IN. For the analyses birch pollen washing water (BP-WW) was used. Since many different substances are present in birch pollen, solid phase extraction was performed to reduce sample complexity. Results revealed that IN within birch pollen may have amphiphilic properties. Since Pummer et al. (2012) it is known that IN from birch pollen are within a macromolecular size range. In this thesis we used centrifugal filtration to get information about the size of IN. When using a filter with a 30 kDa cut-off, the retentate remained ice nucleation active, whereas the filtrate did not, indicating that IN are larger than 30 kDa. Results from the analysis of BB-WW with the *Agilent* Bioanalyzer 2100 revealed that there are different proteinaceous substances in varying sizes present in the pollen. However, ice nucleation activity of those separated substances could not be tested. For the separation of different substances within BP-WW, fractions obtained from SPE and centrifugal filtration, capillary electrophoresis (CE-UV) was used. Many various components were found to be present in birch pollen. However, IN could not be detected with this method. According to LC-ESI-MS and Tandem-MS (ESI-MS/MS and ESI-MS^3) experiments, the flavanol quercetin linked with two hexose sugars was found to be present in birch pollen. It is thought to be responsible for the yellow color of the pollen. However, results verified that this flavonoid is not ice nucleation active and thus no IN from birch pollen.

Zusammenfassung

Wasser kann in der Atmosphäre bis zu -38°C unterkühlt werden, da der Gefrierprozess nicht nur von der Thermodynamik, sondern auch von kinetischen Effekten abhängt. Der Phasenübergang von flüssig auf fest erfolgt entweder homogen (nur Wassermoleküle sind am Prozess beteiligt) oder heterogen, wobei Fremdstoffpartikel, sogenannte Eiskeime, den Vorgang katalysieren. Eiskeime können die Bildung von Eiswolken, welche eine große Bedeutung für Klima und Wetter haben, auslösen. Der Einfluss biologischer Eiskeime auf atmosphärische Prozesse ist noch nicht eindeutig geklärt und viele Fragen stehen offen: Wie beeinflussen biologische Eiskeime die Wolkenbildung? Wie funktioniert der Transport von biologischen Eiskeimen von der Erdoberfläche in die freie Troposphäre? Welche chemischen Eigenschaften und Strukturen haben biologische Eiskeime? Diese Arbeit beschäftigt sich mit der letztgenannten Frage. *Betula pendula* Birkenpollen, welche eisnukleationsaktiv sind, wurden zur Charakterisierung ihrer Eiskeime analysiert. Für die Versuche wurde Birkenpollenwaschwasser verwendet. Da sich sehr viele verschiedene Substanzen in Birkenpollen befinden, wurde zuerst eine Festphasenextraktion durchgeführt, um die Komplexizität der Probe zu reduzieren. Die Ergebnisse zeigen, dass Eiskeime von Birkenpollen vermutlich amphiphile Eigenschaften aufweisen. Seit Pummer et al. (2012) ist bekannt, dass die Größe der Eiskeime von Birkenpollen im makromolekularen Bereich liegt. In dieser Arbeit wurde die Zentrifugenfiltration genutzt, um Informationen über die Größe der Eiskeime zu erhalten. Bei Verwendung eines Filters mit einem cut-off von 30 kDa, bleibt der Rückstand bzw. das Retentat eisnukleationsaktiv, wobei das Filtrat seine Aktivität verliert. Dieses Ergebnis deutet darauf hin, dass Eiskeime größer als 30 kDa sind. Resultate der Analyse von Birkenpollenwaschwasser mit dem *Agilent* Bioanalyzer 2100 zeigen, dass verschiedene proteinartige Substanzen unterschiedlicher Größe in Birkenpollen anwesend sind. Die Eisnukleationsaktivität dieser konnte jedoch nicht analysiert werden. Zur Separation verschiedener Substanzen im Birkenpollenwaschwasser, in den Fraktionen erhalten durch Festphasenextraktion und Zentrifugenfiltration, wurde die Kapillarelektrophorese verwendet. Die Elektropherogramme zeigen diverse Substanzen mit unterschiedlichen Migrationszeiten, was darauf hinweist, dass viele verschiedenen Komponenten in Birkenpollen vorhanden sind. Die Eiskeime konnten jedoch mit dieser Methode nicht detektiert werden. LC-ESI-MS- und Tandem-MS (ESI-MS/MS and ESI-MS^3) Experimente zeigen die Präsenz des Flavanols Quercetin, gekoppelt mit zwei Zuckerhexosen in Birkenpollen. Die Vermutung, dass es sich dabei um den gelben Farbstoff der Birkenpollen handelt, liegt nahe. Allerdings machen die Ergebnisse sichtbar, dass dieses Flavonoid nicht eisnukleationsaktiv ist und somit kein Eiskeim von Birkenpollen ist.

Danksagung

An dieser Stelle möchte ich mich bei meinen BetreuerInnen Ao.Univ.Prof. Dipl.-Chem. Dr.rer.nat. Hinrich Grothe, Associate Prof. Mag.rer.nat. Dr.rer.nat. Martina Marchetti-Deschmann und Univ.Prof. Mag.pharm. Dr.rer.nat. Günter Allmaier für die Ermöglichung dieser Arbeit, die produktiven, monatlichen Meetings und ihre Unterstützung, die sie mir während dieser Zeit entgegengebracht haben, bedanken. Weiters danke ich ihnen für die Aufnahme in die jeweiligen Arbeitsgruppen.

Ein weiterer Dank gilt Assistant Prof. Mag.rer.nat. Dr.rer.nat.Victor Weiss, Univ.Ass. Dipl.-Ing. Laura Felgitsch und OR Mag.pharm. Dr.rer.nat. Ernst Pittenauer für die Geräteeinschulungen und dass sie mir während meiner praktischen Arbeit immer mit Rat und Tat zur Seite standen.

Ebenfalls möchte ich mich bei beiden Arbeitsgruppen für die schöne Zeit und die gute Zusammenarbeit bedanken. Besonders bei Rudolf Bednar, der mir immer mit seinen Ratschlägen weitergeholfen hat.

Für die finanzielle Unterstützung während der Durchführung dieser Arbeit möchte ich dem FWF (P26040) danken.

Ganz besonders danken möchte ich meiner Familie, die mich immer unterstützt, mir zur Seite steht und Rückhalt gibt!

Table of content

Abbreviations

ACN	Acetonitrile
BIN	Biological ice nucleus/nuclei
BPC	Base peak chromatogram
BP-WW	Birch pollen washing water
CCN	Cloud condensation nucleus
CE	Capillary electrophoresis
CID	Collision induced dissociation
DMSO	Dimethyl sulfoxide
DTT	Dithiothreitol
EOID	Electron optical ion detector
ESI	Electrospray Ionization
FWHM	Full width at half maximum
HPLC	High performance liquid chromatography
ICP	Ice nucleation protein
IN	Ice nucleus/nuclei
INA	Ice nucleation activity
IR	Infrared
LC	Liquid chromatography
m/z	Mass-to-charge ratio
MWCO	Molecular weight cut-offs
MS	Mass spectrometry
MS/MS	Tandem mass spectrometry
MS^n	Multi-stage mass spectrometry
QIT	Quadrupole Ion Trap
RH	Relative humidity

SPE	Solid phase extraction
UHQ	Ultra high quality
UV	Ultra violet
Vis	Visible

1. Introduction

1.1. The Climate

The Earth's climate and its changes are frequently discussed topics in public media since an increase of the Earth's surface temperature has been observed over the last decades. In 1824 Jean Baptiste Joseph Fourier suggested the theory that gas molecules concur to the warming of the atmosphere (Fourier, 1824). In 1896, Svante Arrhenius proposed that the change in temperature of the atmosphere correlates with the amount of atmospheric CO_2 (Arrhenius, 1896). He claimed that the temperature of the Earth increases due to the increase of emitted CO_2 coming from fossil fuel burning and other processes. Since 1958, systematic research of the atmospheric greenhouse effect started (Keeling, 1958). Since 1988, the International Panel on Climate Change is collecting scientific data about climate change from all over the world.

Different drivers influence the climate. Clouds and aerosols are one of these drivers. Aerosols can scatter, reflect and absorb light, depending on their physical properties. Bright aerosols like sulfate aerosol reflect light, cooling the atmosphere (Nasa and Dunbar, 1996). On the other hand, dark aerosols like soot, absorb light resulting in a warming effect (Ramanathan et al., 2001). In addition, aerosols can influence cloud formation. High- and mid-level clouds, ice clouds, are able to scatter and reflect incoming sunlight back to space. Thus, ice clouds have a cooling effect on the global climate. In contrast, low-level clouds are able to reflect IR radiation coming from the ground causing warming. However, the Intergovernmental Panel on Climate Change (IPCC) reports that the influence of the cloud and aerosol system on the climate is quite uncertain and the level of confidence is low (Ipcc et al., 2013).

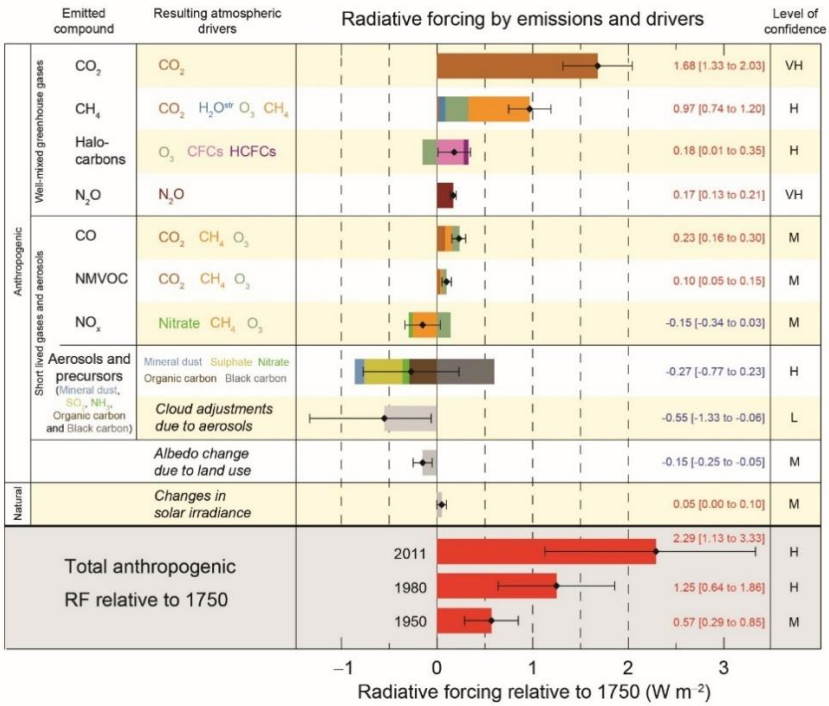

Figure 1: Main drivers of climate change. The level of confidence is showed to the far right (VH: very high, H: high, M: medium, L: low). (source: Ipcc et al. (2013))

Cloud microphysics and the influence of different aerosols to (ice-) cloud formation are still not fully understood. Therefore, further investigations are needed to be able to understand their contribution to the Earth's climate system.

There is a distinction between weather and climate. Weather is the state of the atmosphere at a specific location and time. Parameters like temperature, pressure, relative humidity, wind, precipitation etc. influence weather conditions (Ipcc et al., 2013).

The definition of climate from IPCC is written as follows:

"Climate in a narrow sense is usually defined as the average weather, or more rigorously, as the statistical description in terms of the mean and variability of relevant quantities over a period of time ranging from months to thousands or millions of years. The relevant quantities are most often surface variables such as temperature, precipitation and wind. Classically the period for averaging these variables is 30 years, as defined by the World Meteorological Organization. Climate in a wider sense also includes not just the mean conditions, but also the associated statistics (frequency, magnitude, persistence, trends, etc.), often combining parameters to describe phenomena such as droughts." [1]

The Earth's climate system is of great complexity. It is affected by many different factors consisting of the atmosphere, hydrosphere, land area and all living things. However, a major

[1] IPCC Fifth Assessment Report: Climate Change 2013 (AR5) p.123

factor determining the climate system is the solar radiation and its energy. Figure 2 displays the global energy budget.

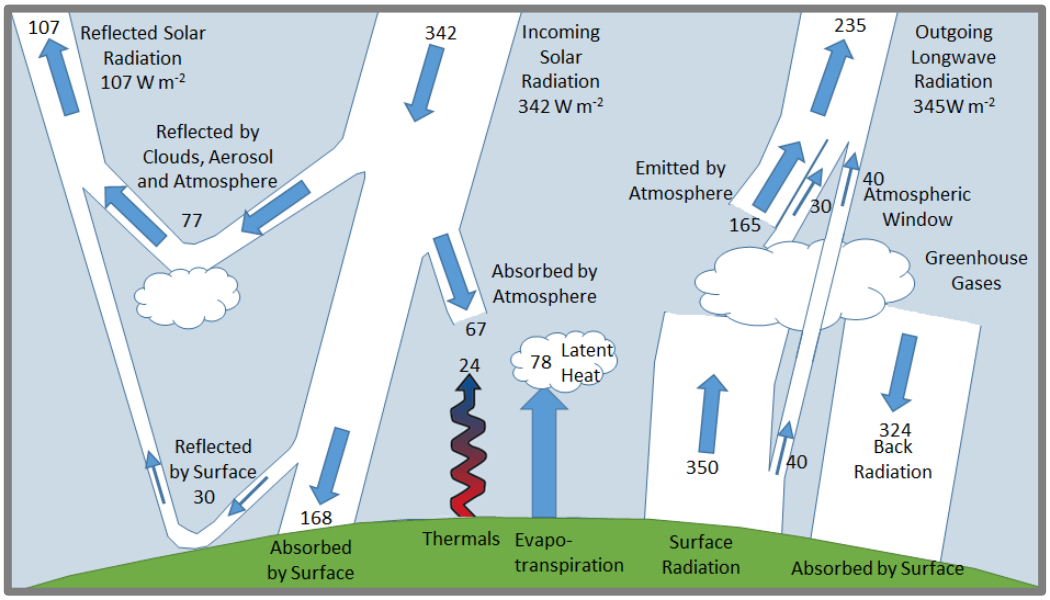

Figure 2: Estimate of the Earth's annual and global mean energy budget. Units are W m^{-2}. (adapted from: Kiehl and Trenberth (1997))

Figure 2 explains the heat and radiation flows. The IPCC states in its fourth report that there are three main variables changing the radiation balance (Ipcc et al., 2007):

1. Change of incoming solar radiation
2. Change of emitted blackbody radiation from the Earth
3. Change of solar radiation reflectance, also called albedo. Such change can be attained through changes in e.g. existence of clouds

1.2. The Atmosphere

Clouds appear in the Earth's atmosphere. The atmosphere is of unique importance as it makes life, as we know it, possible. The atmosphere consists of different gases, mainly N_2 (78%), O_2 (21%) and Ar (0,9%). The remaining 0,1% consist of different trace gases, including water vapor (relative humidity, RH, variable) which is the most abundant greenhouse gas, CO_2 (~400 ppm) and others. These gaseous components are held on the Earth's surface by the gravity field of the planet. Although trace gases make up just a small part, they are really important as they can influence cloud formation and are able to absorb IR radiation (Seinfeld and Pandis, 2006).

The variation of pressure and density with height in the atmosphere is described by the barometric formula. The formula states that pressure and thus density decrease exponentially

with higher altitude. Consequently, most of the atmosphere's mass (ca. 80%) is in the lower region of the atmosphere. Equation 1 shows the barometric formula.

$$p_{(h)} = p_0 \cdot \exp\left[-\frac{M \cdot g}{R \cdot T} \cdot h\right]$$

Equation 1

$p_{(h)}$ ..... Pressure at an altitude h [Pa]

p_0 ..... Pressure at sea level 101300 [Pa]

M ..... Mean molar mass of atmospheric gases 0,02896 $[\frac{kg}{mol}]$

g ..... Gravity 9,80665 $[\frac{m}{s^2}]$

R ..... Universal gas constant 8,314 $[\frac{J}{K \cdot mol}]$

T ..... Temperature assumed constant at 288,15 [K]

h ..... Altitude [m]

The atmosphere is divided into five layers according to temperature. Starting from the lowest: Troposphere, Stratosphere, Mesosphere, Thermosphere, Exosphere.

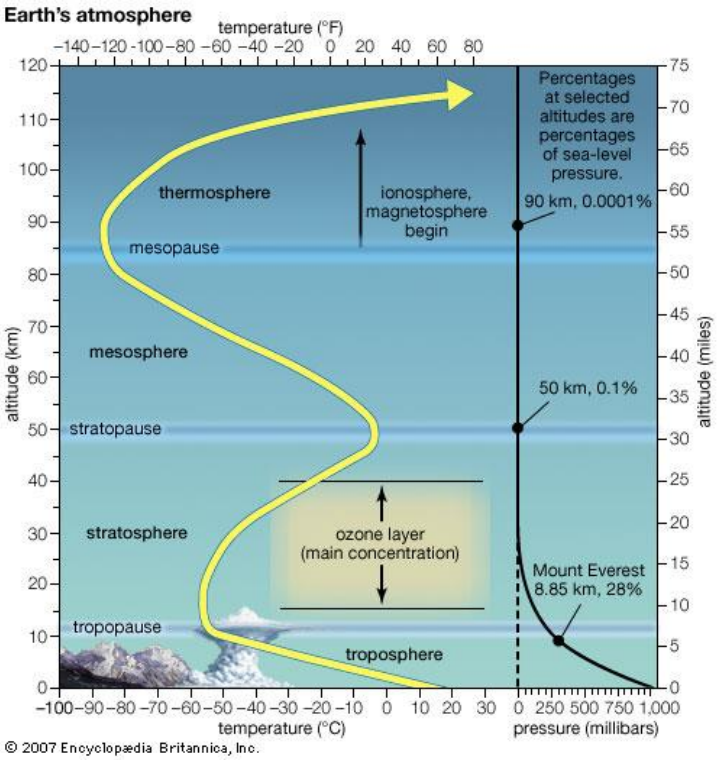

Figure 3: Layers of the atmosphere with the temperature gradient. (source: Pielke (2017))

1. Troposphere

The troposphere is the lowest layer of the atmosphere and thus the layer with the highest density, containing about 80% of atmosphere's total mass. The troposphere starts from the Earth's surface up to between 10 - 15 km, depending on the latitude and time of the year. The highest temperature within the troposphere is at the planet's surface due to black body emissions from the Earth. As altitude increases, temperature decreases almost linearly.

The troposphere is the layer, where most of the weather takes place. Warm air from the Earth's surface tends to rise, leading to rapid vertical mixing of air masses. Due to such convection of air, clouds can develop (Sigalotti et al., 2014). The end of the troposphere is characterized by the tropopause, a region of stable temperature.

2. Stratosphere

The stratosphere is extending from the end of the tropopause up to around 50 km. Temperature rises with increasing altitude. This increase in temperature is due to the fact that oxygen and ozone molecules absorb ultraviolet (UV) radiation from the sun, converting the UV energy into heat. This process takes places in the ozone layer and is called Chapman Cycle.

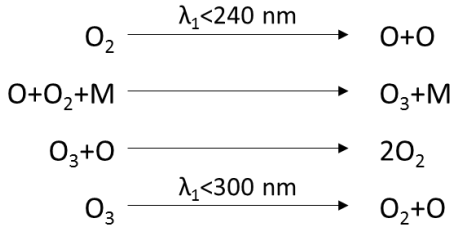

Figure 4: Chapman cycle

Due to the increase of temperature within the stratosphere, vertical mixing of air masses is restrained. In contrast to the troposphere, the stratosphere is characterized by very stable atmospheric conditions. Subsequently, clouds are rare within this layer (Seinfeld and Pandis, 2006). However, Polar Stratospheric Clouds (PSCs) can be formed in very cold polar nights. The stratopause marks the end of the stratosphere.

3. Mesosphere

The mesosphere starts from the stratopause and extends to about 80 - 90 km. Temperature increases with higher altitude reaching about -90°C at the mesopause, which is the coldest place on our planet.

4. Thermosphere

The thermosphere extends from around 90 to 600 km. As indicated by the name, this layer is characterized by high temperatures reached through the absorption of x-rays and UV radiation by nitrogen (N_2) and oxygen (O_2). However, the temperature within this layer is not well defined since pressure is so low that the mean free path of molecules exceeds kilometers, resulting in rare collisions and energy transfer. At the upper thermosphere the ionosphere starts, where atoms and molecules are ionized by photoionization (Seinfeld and Pandis, 2006).

5. Exosphere

The outer layer of the atmosphere is the exosphere. The “air” in that layer is very thin and gas molecules can escape the gravity field. Mainly hydrogen and helium are present in this layer. Depending on the solar activity the exosphere ends at about 1000 km.

1.3. Clouds

Clouds cover around 70% of our planet’s surface (Gutro, 2004). They are significant entities in the Earth’s atmosphere. First, they influence the radiation balance of the Earth due to their ability to reflect and scatter electromagnetic radiation. They occur depending on the nature of the cloud and the altitude (Lohmann et al., 2016a). Secondly, clouds play a key role in the hydrological cycle, as they transfer water in form of precipitation of rain or snow from the atmosphere back to the Earth’s surface. Further, rain drops and snow are able to scavenge aerosol particles. This process is called wet deposition. Aerosol particles are transported from the atmosphere back to the ground through precipitation. Moreover, within cloud droplets aqueous-phase chemical reactions occur. Furthermore, clouds enable vertical and horizontal transport of mass and heat in the atmosphere (Seinfeld and Pandis, 2006).

Clouds can be classified according to their shape and altitude. According to Ahrens (2007) clouds can be divided into four groups: Cirro, Alto, Strato and Nimbo. Clouds appear in different altitudes of the atmosphere, which can be vertically divided into 3 “etages”: low, middle and high (Wmo, 1975). Strato clouds are located in the low-level, Alto in the mid-level and Cirro in the high-level. Clouds which extend over more etages are called Nimbo. The World Meteorological Organization (WMO) defined 10 different cloud types called “genera” (Wmo, 1975). Table 1 shows the altitudes where different cloud types are found.

Table 1: The ten cloud types according to WMO and their occurrence in different altitudes.

Etage	Genera	Polar Regions	Temperate Regions	Tropical Regions
Low-Level	Stratocumulus (Sc) Stratus (St) Cumulus (Cu) Cumulonimbus (Cb)	to 2 km	to 2 km	to 2 km
Mid-Level	Altocumulus (Ac) Altostratus (As) Nimbostratus (Ns)	2-4 km	2-7 km	2-8 km
High-Level	Cirrus (Ci) Cirrocumulus (Cc) Cirrostratus (Cs)	3-8 km	5-13 km	6-18 km

The altitudes where different cloud types are found depend on the region.

In Figure 5 the different clouds are pictured.

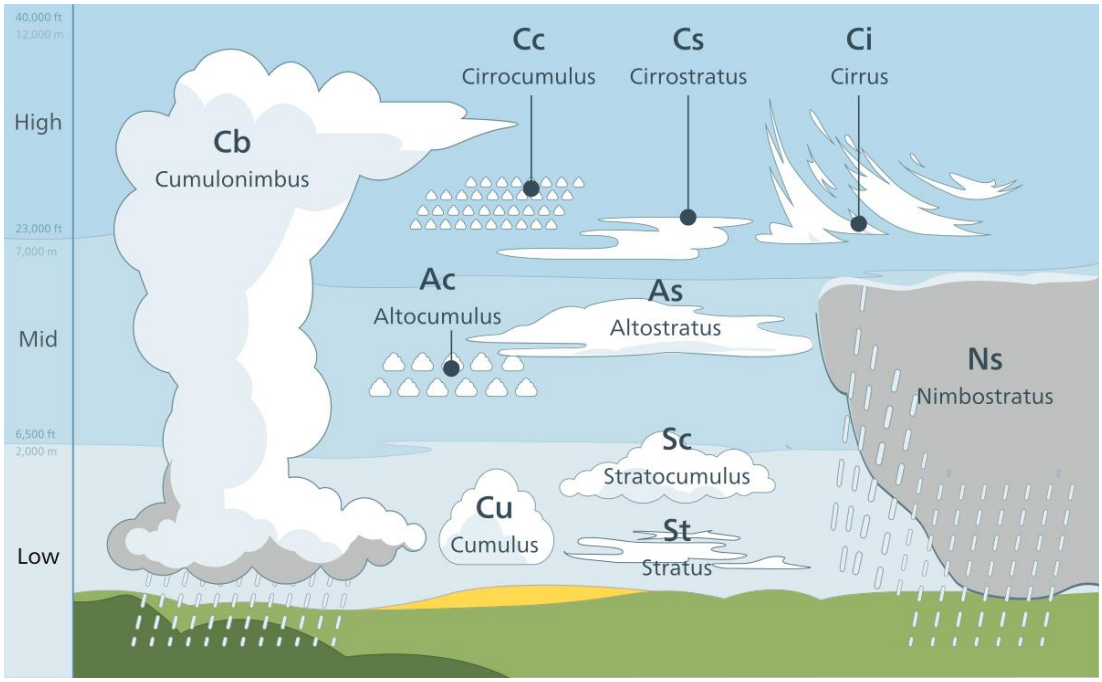

Figure 5: Schematic illustration of different cloud types. (source: Bruyn (2012))

Another way to characterize clouds is to look at their microphysical properties. Clouds can be divided into warm clouds, mixed-phase clouds and ice clouds. They can be differentiated by the phase state of their droplets. Warm clouds consist entirely of liquid droplets, whereas only

ice crystals are present in ice clouds. Mixed-phase clouds consist, as the name already indicates, of both liquid and frozen water droplets (Lohmann et al., 2016a). Warm clouds can have temperatures above as well as below 0°C, as long as water droplets are in the liquid phase. They exist down to -38°C, where homogenous freezing of water starts. The temperature of mixed-phase clouds is between 0°C and -38°C. Ice clouds can have all temperatures below 0°C (Lohmann et al., 2016a). For the formation of clouds, the saturation ratio is a crucial factor. It is defined as:

$$S = \frac{p_{H_2O}}{p^S_{H_2O}(T)}$$

Equation 2

S ..... Saturation ratio

p_{H_2O} ..... Partial pressure of water [Pa]

$p^S_{H_2O}(T)$ ..... Saturation vapor pressure of water in equilibrium with its liquid phase at temperature T [Pa]

Vapor is subsaturated if S<1, saturated if S=1 and supersaturated if S>1 (Seinfeld and Pandis, 2006).

Warm clouds, e.g. cumulus (Cu), form due to the fact that water vapor coming from the Earth's surface condenses (relative humidity must be over 100%). This can happen either directly (supersaturation of air is necessary) or on cloud condensation nuclei (CCN). Warm air from the Earth's surface is ascending. Since pressure decreases with altitude, the air parcel expands and cools down (adiabatic cooling) (Gabler et al., 2007).

Ice clouds, e.g. cirrus (Ci), occur at high altitudes in the upper troposphere. They form either directly from water vapor or through freezing of supercooled water droplets (ice nucleation).

1.4. Ice nucleation

The phase transition from solid to liquid water occurs at 0°C at atmospheric pressure (101325 Pa). However, this is only true for the melting process. In contrast, freezing of water does not only depend on thermodynamics but is steered by kinetics (Oxtoby, 1999). Thus, freezing does not necessarily have to start at 0°C and water can be supercooled to temperatures between -36°C and -38°C. In general, the phase transition can be homogeneous or heterogeneous.

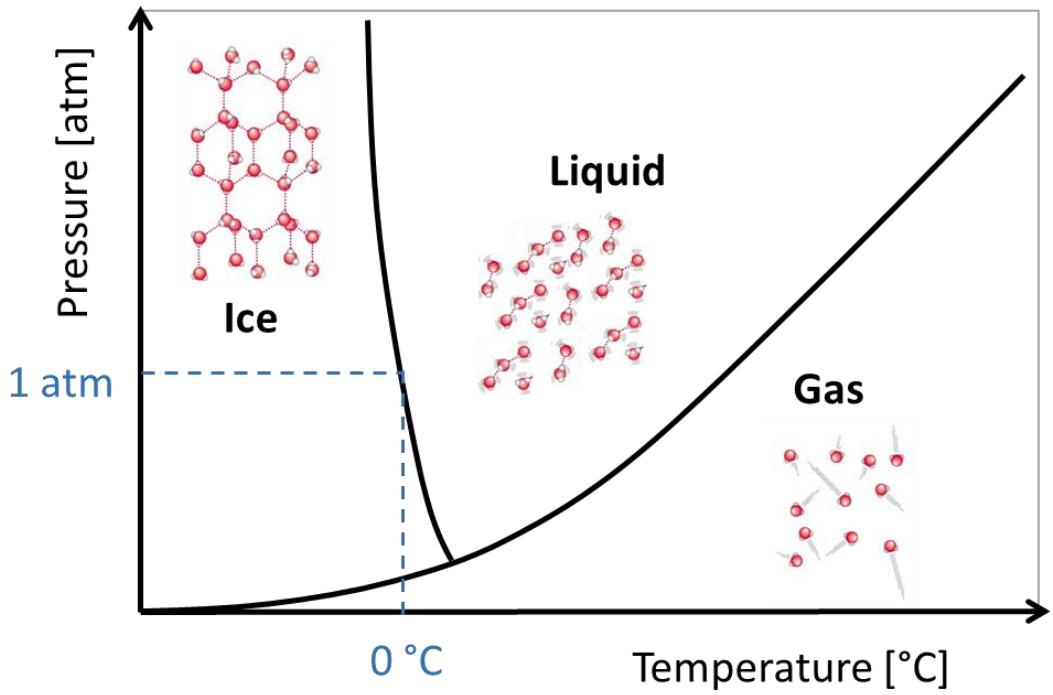

Figure 6: Phase diagram of water.

Homogeneous ice nucleation starts at temperatures between -36°C and -38°C. In this process, no other molecules are involved in comparison to heterogeneous ice nucleation, where foreign particles, so called ice nuclei (IN) play a key role. These IN act as catalysts in the freezing process. Heterogeneous ice nucleation takes places at temperatures above -38°C.

There are different phases of solid water. The structure can vary depending on the ambient conditions. The main solid phase of water in the biosphere is hexagonal ice (I_h) (Pruppacher et al., 1997). In this thesis I_h will be denoted as 'ice'. Beside this solid phase of water, many more have been identified, but are neglected due to the scope of this thesis.

1.4.1. Homogeneous ice nucleation

Liquid water can be supercooled several degrees below the melting point, if cooling is done very slowly, there are no impurities in the water and the water is standing still. In the atmosphere liquid droplets can stay liquid till temperatures down to -38°C. This happens through the fact that water molecules have to be arranged into ordered molecular ice structures that form a cluster, a so-called ice embryo. At -5°C 50.000 water molecules need to get together until the ice embryo is stable enough and can grow further. Whereas, at -20°C just a few hundred are needed (Zachariassen and Kristiansen, 2000). The ice embryo needs to overstep the critical radius at the prevailing temperature in order to form an ice crystal. The Gibbs free energy for homogenous nucleation is shown in Equation 3.

$$\Delta G_{cl} = -\frac{4\pi r^3 kT}{3v} lnS + 4\pi r^2 \sigma$$

volume term ΔG_V surface term ΔG_S

Equation 3

ΔG_{cl} ..... Gibbs free energy of forming a cluster [J]

v ..... Specific volume of ice [m^3 kg^{-1}]

r ..... Radius of cluster [m]

k ..... Boltzmann constant 1,38 x 10^{-23} [J K^{-1}]

T ..... Temperature [K]

S ..... Saturation ratio (Equation 2)

R_v ..... Gas constant of water vapor 461,5 [J kg^{-1} K^{-1}]

σ ..... Interfacial energy [N m^{-1}]

Equation 3 consist of two terms: a negative volume driven term (ΔG_V) and a positive surface driven term (ΔG_S). The volume term is proportional to the third power of r. The term is negative due to intermolecular ordering. The surface driven term is proportional to r^2. It is positive because work needs to be invested since a new surface forms as the ice crystal grows.

In Figure 7, the total free energy (ΔG_{cl}) has a local maximum. This maximum indicates the energy barrier which needs to be exceeded to form a spherical ice cluster. The energy barrier is given in Equation 4.

$$\Delta G^* = \frac{16\pi}{3} \frac{v^2 \sigma^3}{[kTlnS]^2}$$

Equation 4

ΔG^* ..... Gibbs free energy barrier [J]

The height of the barrier depends on σ^3 and $\ln S^{-2}$. Thus, a small interfacial energy (between ice nucleus and the environment) and a large supersaturation lead to a small Gibbs free energy barrier, making nucleation possible.

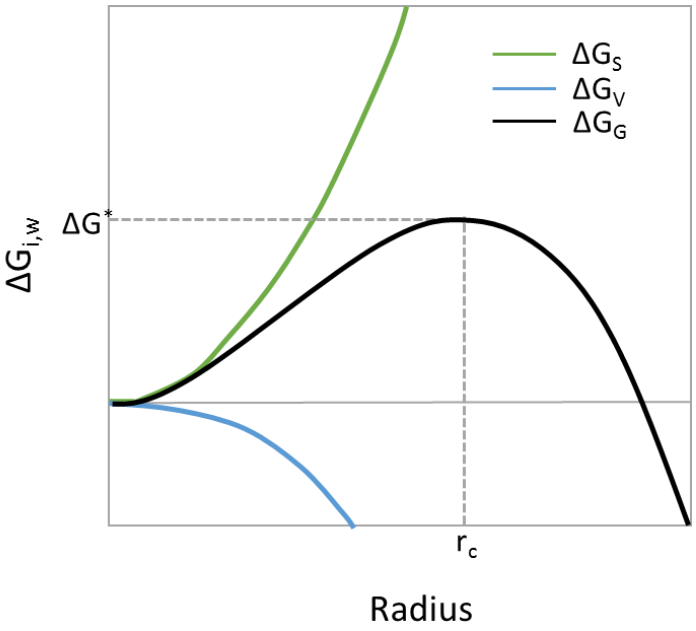

Figure 7: Change in Gibbs free energy of forming a cluster for homogenous nucleation. (adapted from:Lohmann et al. (2016a))

For small radii the surface term dominates and the total Gibbs free energy is positive. The maximum is not exceeded and the formation of ice crystals will not occur. For larger radii the volume term dominates and the free energy is negative. The critical radius (r_c) of the ice cluster is exceeded and freezing takes place. Furthermore, the critical radius depends on the temperature. With a decrease in temperature, the critical radius decreases.

Homogeneous freezing is a stochastic process and thereby occurs with a certain probability and depends on the volume of the droplet. More volume raises the possibility of fluctuations and cluster formation. It can be described by the nucleation rate J_{hom} as seen in Equation 5.

$$ln\frac{n_{tot}-n_{ice}}{n_{tot}} = \ln(1-f_{ice}) = -J_{hom}Vt$$

Equation 5

n_{tot} ..... Total number of droplets

n_{ice} ..... Number of frozen droplets

J_{hom} ..... Nucleation rate [cm^{-3} s^{-1}]

V ..... Droplet volume [cm^3]

t ..... Observation time [s]

1.4.2. Heterogeneous ice nucleation

If the freezing process includes an ice nucleus, it is referred to as heterogeneous ice nucleation. IN are particles which lower the energy barrier for forming ice crystals, enabling freezing at higher temperatures. Thus, they act as catalysts in the freezing process. In the atmosphere, aerosol particles can act as IN, triggering cloud glaciation. Not all aerosols are IN. Certain properties must be fulfilled so that ice-like structures can be formed (Lohmann et al., 2016b). Fletcher (1969) claimed that just particular areas of IN are catalyzing the freezing process, so called "active sites". "*Active sites […] are usually associated with defects such as steps and cracks" (Marcolli, 2014).*

There are different IN known such as soot, mineral dust, biological material, different bacteria, fungi, plankton, pollen of diverse plants and others. The role of biological IN in atmospheric processes is still not fully understood. In this thesis, we work with birch pollen, which act as IN. It was first found by Diehl et al. (2001) and (2002) that birch pollen have the ability to catalyze heterogeneous ice nucleation. It was thought that the whole pollen grain and the surface morphology was responsible for ice nucleation activity. However, it was showed that IN are much smaller than the whole grain and that they can be washed off from the pollen's surface with water. The small size and stability of the suspension leads to the conclusion that those IN are specific macromolecules (Pummer et al., 2012)

There are different modes of heterogeneous ice nucleation found in the literature (Figure 8).

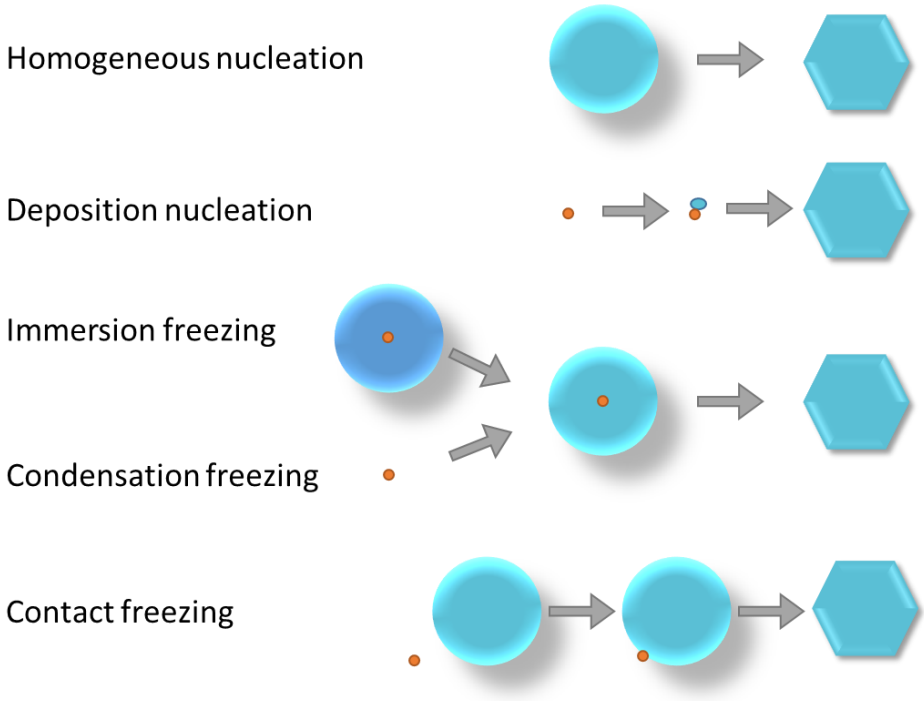

Figure 8: Schematic illustration of the different modes of heterogeneous nucleation. The small, orange spheres represents the IN, the blue, big spheres droplets and the hexagons ice crystals.

Deposition nucleation: Water vapor directly deposit on the ice nucleus. First, the water vapor is adsorbed and then converted to ice.

Immersion freezing: The ice nucleus is suspended in the liquid droplet. Due to cooling of the droplet, freezing starts.

Condensation freezing: Water vapor is condensed on the particle's surface and form a liquid droplet, which can freeze.

Contact freezing: The ice nucleus collides with a supercooled droplet, which freezes immediately.

In mid-level clouds, contact and immersion freezing are dominating (Murry et al., 2012). In this thesis, the freezing experiments (see chapter 2.1) are based on immersion freezing.

Immersion freezing has two principals: 1) stochastic and 2) singular.

1) The time dependent stochastic process is further divided into a.) the single component stochastic (SCS) and b.) the multi component stochastic (MCS) process.

1a) In the single component stochastic process, every single drop of an array has the same composition. Hence, all droplets freeze at the same temperature and have the same time dependent probability of freezing. Equation 6 displays the fraction of frozen droplets in a time interval Δt (Murray et al., 2012).

$$\frac{\Delta n_{ice}}{N} = 1 - exp(-J_{het} s \Delta t)$$

Equation 6

$\frac{\Delta n_{ice}}{N}$ ..... Fraction of frozen droplets

J_{het} ..... Heterogeneous nucleation coefficient [cm^{-2} s^{-1}]

s ..... Nucleant surface area

Δt ..... time interval [s]

1b) If the droplets do not contain the same material and consist of different particle types, the MCS description can be used. "*The droplets have a distribution of ice nucleating abilities"* (Murray et al., 2012).

$$\frac{\Delta n_{ice}}{N} = 1 - exp\left(-\sum_i J_i s_i \Delta t\right)$$

Equation 7

J_i ..... nucleation rate coefficient of an ice nucleus of type i [cm^{-2} s^{-1}]

1c) Another stochastic model is introduced by Niedermeier et al. (2011). It is called the "soccer ball" model. Each particle has several specific active sites. For detailed information see (Niedermeier et al., 2011).

2) Using the time independent singular description, freezing of a certain IN happens at a specific particle surface site at a specific temperature (Murray et al., 2012).

$$f_{ice}(T) = \frac{n_{ice}(T)}{N_{tot}} = 1 - exp(-n_s(T)s)$$

Equation 8

$f_{ice}(T)$ ..... Fraction of droplets freezing at temperature T

$n_{ice}(T)$ ..... Number of frozen droplets at temperature T

N_{tot} ..... Total number of droplets

$n_s(T)$ ..... Number of nucleation sites per surface area

1.5. Aerosols

In addition to different gases (chapter 1.2), the atmosphere consists of aerosol particles, coming from various origins. The concentration and composition of aerosol particles strongly depend on the time of the year, meteorological conditions and the location. For example, over land, soil minerals and anthropogenic pollutants are mainly present, whereas silicate minerals and sea salt are more frequently found over oceans (Schlesinger and Bernhardt, 2013).

Aerosol particles can be divided into primary and secondary particles. Primary particles are directly emitted into the atmosphere. They are emitted from e.g. combustion, physical erosion of rocks, dust regions and others. Secondary particles are formed only in the atmosphere by gas to particle conversion (Agranovski, 2010). Aerosol particles are of great importance as they influence cloud formation. Some of them can act as CCN or IN in heterogeneous nucleation processes. Birch pollen, which are analyzed in this thesis, belong to the primary biological aerosol particles (PBAP). They make up 23% of total aerosol mass in rural regions and 17% over the oceans (Bowers et al., 2012). As already mentioned in chapter 1.4.2, Diehl et al. (2001) and (2002) investigated that birch pollen are efficient IN. Hence, they can trigger cloud glaciation. However, ice clouds are located at high altitudes. Thus, the question arises if birch pollen (diameter: ~22 µm) are too heavy to reach such heights. Studies showed that the concentration of BIN is enhanced during and after rainfall (Huffman et al., 2013, Rathnayake et al., 2017). Pollen grains are able to absorb water during rain. Thus, the osmotic pressure inside the pollen rises (D'amato et al., 2007, Rathnayake et al., 2017). The high osmotic pressure can lead either to a rupture of the pollen wall and a suspension of fine-sized pollen fragments is released in the environment or the water suspension from the inside of the pollen is released through the pollen's pores. These small components of pollen can then spread into the atmosphere by e.g. wind. Thus, IN from pollen could indeed play a crucial role in the formation process of ice clouds. However, the transport process from the canopy through the planetary boundary layer into the free troposphere is still unknown. Figure 9 shows the bursting of birch pollen (Pöhlker et al., 2013).

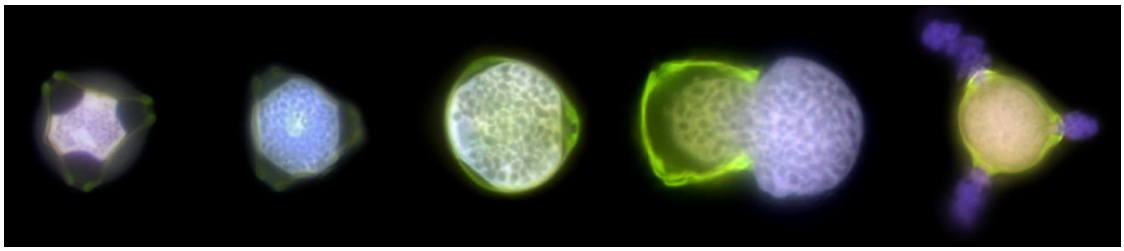

Figure 9: Bursting of birch pollen (source: Pöhlker et al. (2013)

1.6. Birch pollen

As mentioned in the previous chapter 1.5, fragments of birch pollen can be distributed in the atmosphere with the ability to act as ice nuclei and hence, influence cloud formation.

In general, pollen grains are the male gametophytes (sexual reproductive cells) of seed plants (*spermatophytina*). To achieve fertilization, pollen grains need to be delivered to the ovules in the pistil, the female reproductive part. The transfer can be achieved by wind, water, insects or animals. Pollen grains are formed in the anther, which is an element of the male reproductive part (stamen). They contain a tube cell consisting of a vegetative nucleus and male gametes.

Once the pollen grains land on the stigma, an element of the pistil, a pollen tube is formed through the pistil to the ovules by the vegetative nucleus. Hence, the male gametes can be transported to the ovules, where fertilization occurs (Twell et al., 2006). For the protection of the genetic material inside the pollen grain, a rigid wall exists. This wall can be divided into the exine (outer wall) and the intine (inner wall). The exine is composed of sporopollenin. The composition of sporopollenin depends on the species of the pollen. However, dicarboxylic acids, fatty acids and n-alkanes are found to be main components of the sporopollenin (Dominguez et al., 1999). The inner wall, the intine, consists mainly of pectin and cellulose.

The question arises, which components are ice nucleation active?

1.7. IN from birch pollen

IN from different origins (see chapter 1.4.2) can differ in their chemical structure, including polysaccharides (Hiranuma et al., 2015), proteins (Kajava and Lindow, 1993) and others. One enlightened structure of an IN is a protein from the bacterium *Pseudomonas syringe*, better known under the name Snomax® (used for artificial snow production). The ice nucleation protein (ICP) arranges water molecules on the surface of the ICP in an ice-like structure and freezing can occur at higher temperatures (-1.8 to -3.8 C) (Maki et al., 1974).

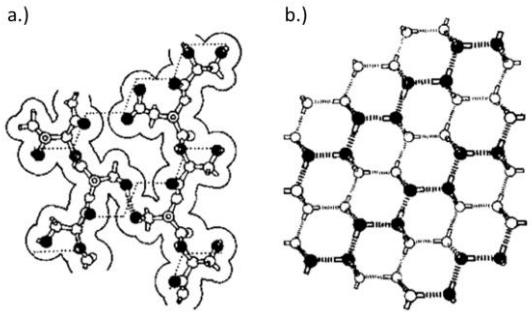

Figure 10: a.) Ice nucleating protein from the bacteria Pseudomonas syringe. b.) Fragment of an ice structure. (source: Kajava and Lindow (1993)

The structure of IN origin from birch pollen is still not elucidated. However, some experiments were carried out in the past and thus, some properties of the IN from birch pollen are already known. Since Pummer et al. (2012), it is known that IN from birch pollen grains are in the macromolecular size range. Pummer's experiments indicate that the size of IN is between 100 and 300 kDa (Pummer, 2013). Furthermore, the stability of IN against oxidants was investigated. For IN to survive in the atmosphere and thus can possibly have an influence on cloud glaciation, they must be resistant to oxidants present in the atmosphere like e.g. ozone (O_3). Oxidation experiments with O_3 and NO_2 showed that IN from *Betula* birch pollen do have a high oxidation stability (Pummer, 2013) Different studies were carried out on the characterization of IN from birch pollen. Pummer et al. (2015) suggested that IN consist of

polysaccharides. However, this suggestion was never proofed. Another study from Dreischmeier et al. (2017) claims that IN from birch pollen are anionic polysaccharides. In the study, they pointed out that proteins do not play a role as ice nucleating particles within birch pollen. However, the FT-IR spectrum in the publication shows indeed an amide I band (Figure 5). Thus, proteins or polyketides should not be taken out of consideration.

1.8. Aim of this thesis

The impact of biological IN (BIN) on atmospheric processes is still not fully understood and questions are still remaining. How exactly do BIN influence cloud formation? How does the transport process of BIN into the free troposphere work? To get answers to these questions, first the chemical properties and the structure of BIN needs to be elucidated. This thesis focuses on the characterization of IN from *Betula pendula* birch pollen. For the analysis, birch pollen washing water (BP-WW) was used. In a first step the sample complexity of BP-WW was reduced performing solid phase extraction (SPE) and centrifugal filtration. Furthermore, capillary electrophoresis, chip-based gel capillary electrophoresis (*Agilent* Bioanalyzer 2100) and liquid chromatography were used for separation of different compounds present in birch pollen. For the determination of substances, mass spectrometry was performed. Fractions obtained from the analytical techniques mentioned above were further analyzed for their ice nucleation activity.

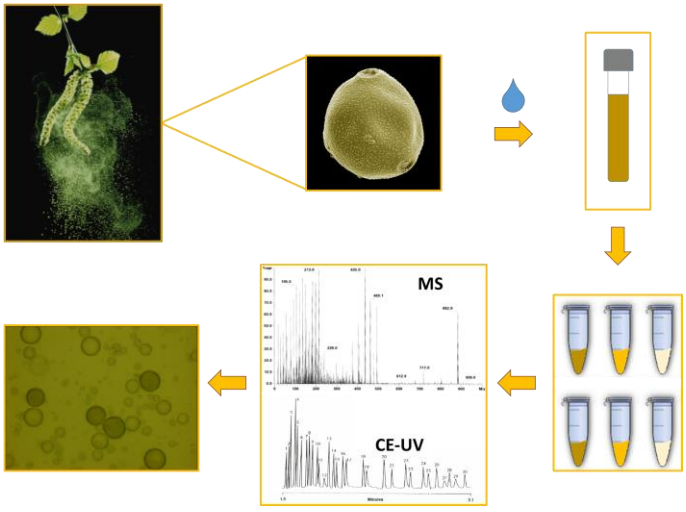

Figure 11: Schematic illustration of this thesis.

2. Methods

2.1. Freezing experiments – VODCA

To investigate the freezing behavior of different samples and get their freezing curves the cryo-microscopy setup VODCA - **V**ienna **O**ptical **D**roplet **C**rystallization **A**nalyzer is used.

2.1.1. Cryo-microscopy - VODCA

A liquid sample of interest is mixed with oil, resulting in a water-in-oil emulsion, where droplets are not in contact with each other. This white emulsion represents the cloud. If the sample is ice nucleation active, its IN are suspended in the liquid droplet. Hence, the freezing occurs in the immersion freezing mode as described in 1.4.2. By decreasing the temperature, freezing of droplets occur. The freezing is seen by the change of the color of the droplets to a dark one (Figure 12).

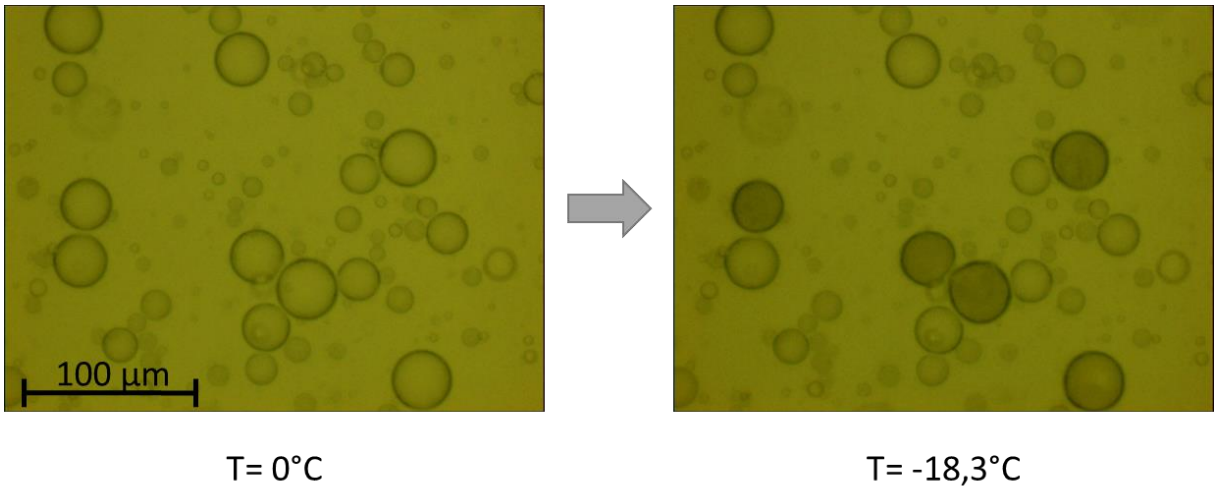

Figure 12: Freezing of droplets observed by the change of the droplet color to a darker one.

The main components of the setup are an optical light microscope, a camera connected to a computer, a power supply and a cryo-cell, including a Peltier-element. A more detailed description of the setup is found in chapter 3.4. The materials and instruments used are listed in Table 2 and Table 3. The freezing process occurs within the cryo-cell. The cryo-cell is a closable can including a sample carrier (cover glass) (A), a single stage Peltier-element (B) and a copper cooling block (C). In the lid of the cell is a glass window to be able to observe freezing events.

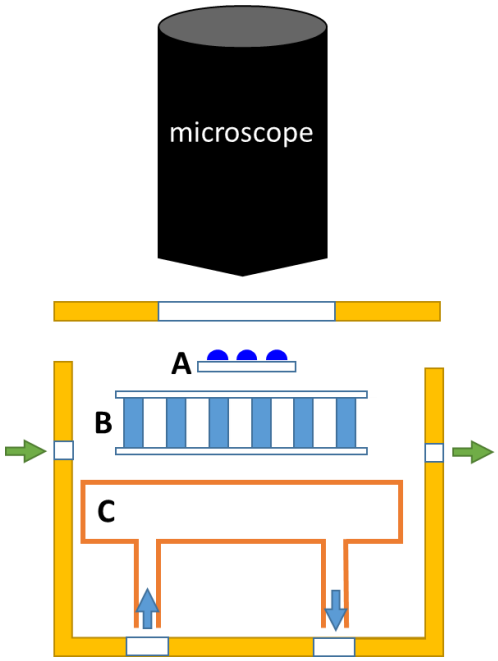

Figure 13: Schematic illustration of the cryo-cell.

The cover glass, with the sample (water-in-oil emulsion) on it, is placed on the Peltier-element. The Peltier-element allows cooling the system due to thermoelectricity effects. It consists of both n- and p-doped semiconductors and two ceramic plates on top and bottom. Heat is transferred from the top of the element to the bottom, where it is connected to the copper cooling block. The heat flux is proportional to the Peltier coefficient of the material and the applied current flow (Kiss and Infante Ferreira, 2016).

$$\dot{Q} = \pi * I$$

Equation 9

$\dot{Q}$ ..... Heat flux

π ..... Peltier coefficient of the material x

I ..... Current flow

The temperature difference between the warm and the cold side of the Peltier-element is referred to as delta T. The Peltier-element used in this thesis had a delta T of 70°C.

To cool the copper cooling block, distilled water cooled with ice, is pumped through the element.

2.2. UV/Vis spectroscopy

UV/Vis spectroscopy uses the interaction between an analyte and electromagnetic radiation in the ultraviolet (200-400 nm) and visible (400-800 nm) region, resulting in a absorption spectrum (Gey, 2008b).

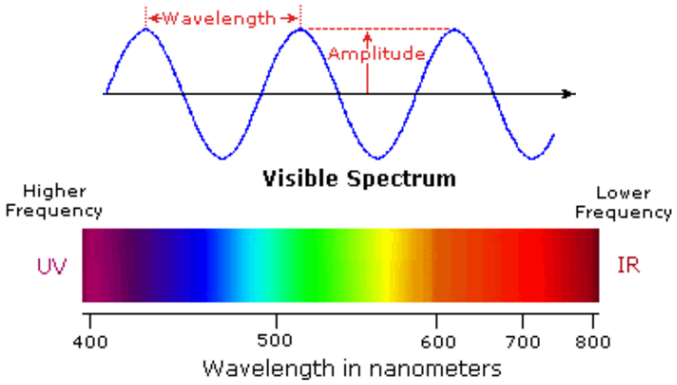

Figure 14: Electromagnetic spectrum. (source: Reusch (2013))

During absorption, the atom or molecule interact with the incoming electromagnetic radiation and valence electrons are excited from the ground level to the excited electronic level (electronic transition). For an atom or molecule to be able to absorb the incoming electromagnetic radiation, the resonance condition must be fulfilled. The energy difference between the energy levels and the energy of the photons must be equal (Equation 10).

$$\Delta E = h \cdot \nu$$

Equation 10

ΔE ..... Energy difference between the energy levels

h ..... Planck's constant 6.626 x 10^{-34} [m^2 kg s^{-1}]

ν ..... Frequency [Hz]

Additionally, the selection rule must be taken into account. Not all electron transfers are allowed. Figure 15 shows typical absorption regions of different electron transfers. Figure 16 shows examples.

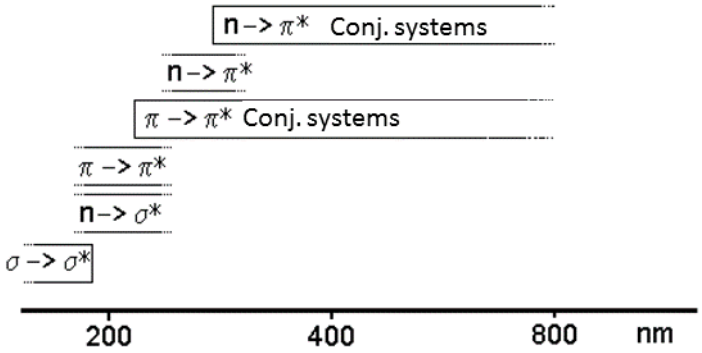

Figure 15: Typical absorption regions of different electron transfers. (source: Lehmann (2009))

Transition	Chromophore	Example	λ_{max}[nm]
n → π*	—N=N—	$H_3C—N=N—CH_3$	347
	—N=O	$(H_3C)_3C—NO$	300; 665
π → π* (conj.)	Polyene	Dihydro-β-carotin	415
π → π*	—C≡C—	HC≡CH	173
	C=C	$H_2C=CH_2$	165
n → σ*+	—N—	$C_2H_5—NH_2$	210
	—Hal	$H_3C—I$	258
σ → σ*	—C—H	CH_4	122
	—C—C—	$H_3C—CH_3$	130

Figure 16: Absorption regions of different electron transitions with examples. (source:Wesener (2005))

For the measurement of absorption in the UV/Vis range, a photometer is used. There are single beam- as well as double beam photometers available (Lottspeich and Engels, 2012e). A schematic illustration of a single- as well as a double-beam photometer is showed below in Figure 17.

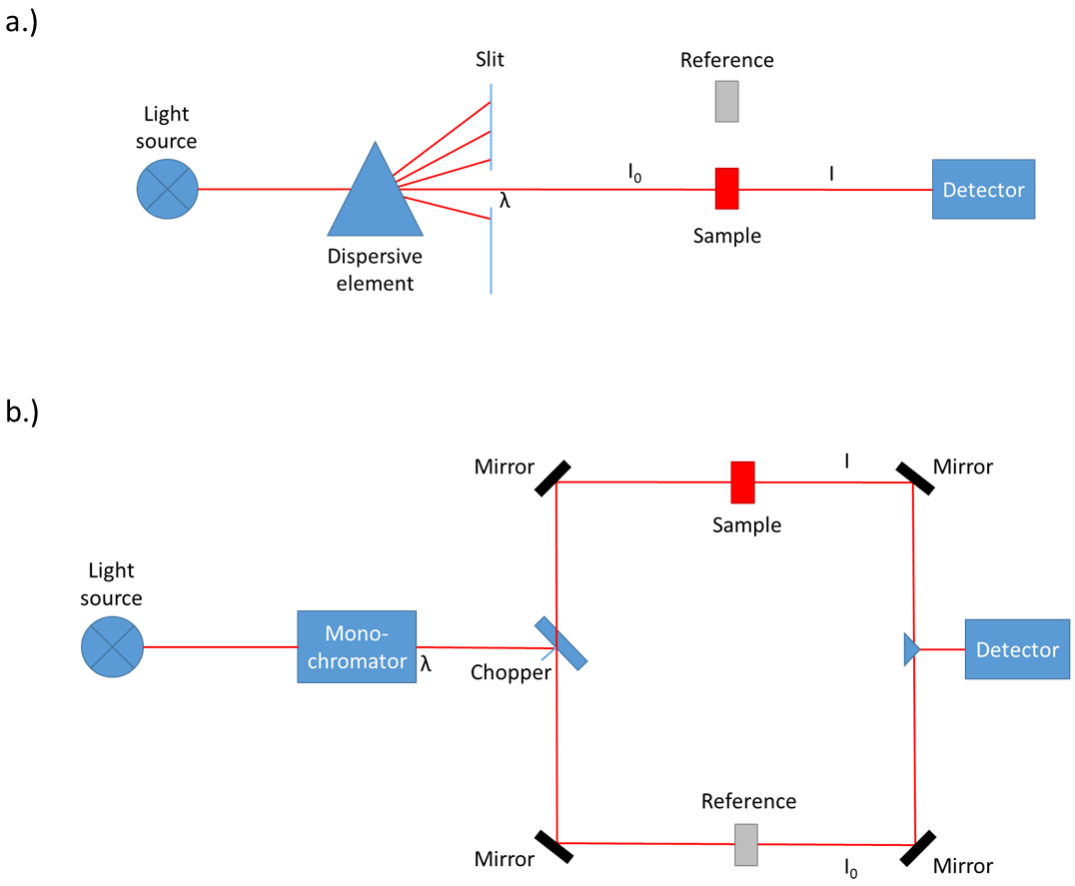

Figure 17: Schematic illustration of a.) a single beam photometer and b.) a double-beam photometer.

2.3. Solid phase extraction

Solid phase extraction (SPE) is a common, simple technique for sample preparation or analyte concentration (Gey, 2008a). It separates different dissolved or suspended components of a liquid sample by polarity, using the affinity of the components to a solid stationary phase, also called sorbens. The sorbens, which has a certain polarity, is placed in a plastic cartridge. As the liquid sample passes through, compounds with the same polarity will interact and retain on the sorbens while other substances pass through the cartridge. After the sample is loaded, elution steps with solvents (mobile phase) follow.

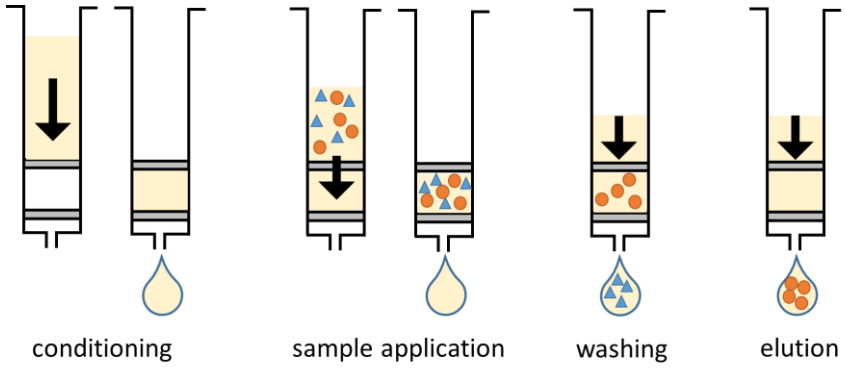

Figure 18: Schematic procedure of solid phase extraction.

The choice of sorbens depends on the properties of analytes of interest.

There are four methods for SPE:

- **Normal phase SPE with polar adsorbens**
  The sorbens is more polar than the mobile phase. Usually silica gel is used as a stationary phase. Typical adsorbents are aldehydes and alcohols.
- **Normal phase SPE with polar modified silica gel**
  Analytes with a moderate or strong polarity are used. The sorbens are e.g. amino modified silica gel.
- **Reverse phase SPE with non-polar modified silica gel**
  The sorbens is less polar than the mobile phase. Octadecyl modified silica gel is used as a sorbens to extract moderate polar and non-polar analytes in e.g. aqueous solutions. This method is often used in environmental chemistry.
- **Ion exchange SPE with ionic modified silica gel**
  Aqueous acids and bases can be extracted either with cation exchange materials for bases or anion exchange functions for acids (Kicinski, 1996).

In this thesis, reverse phase SPE utilizing C_{18} modified silica particles was used.

2.4. Electrophoresis

Electrophoresis separates charged species in a solution or carrier matrices (e.g. agarose gel) under the influence of an electric field. Separation of different substances takes place since different analytes migrate with different velocities due to charge and size/shape of the analyte particle (Lottspeich and Engels, 2012b).

Two forces act on the charged analyte in an electric field: an accelerating force F_e (Equation 11) and a frictional force F_{fr} (Equation 12).

$$F_e = q \cdot E \qquad \text{with} \qquad q = z \cdot e$$

Equation 11

$$F_{fr} = f_c \cdot v \qquad \text{with} \qquad f_c = 6 \cdot \pi \cdot \eta \cdot r$$

Equation 12

F_e ..... Accelerating force [N]

F_{fr} ..... Frictional Force [N]

q ..... Charge of particle [C]

f_c ..... Coefficient of friction

E ..... Electrical field strength [V m^{-1}]

v ..... Migration velocity of the particles [m s^{-1}]

z ..... Charge number

η ..... Dynamic viscosity [kg $s^{-1}m^{-1}$]

e ..... Elementary charge 1,602*10^{-19} [C]

r ..... Stokes radius [m]

The accelerating force F_e acts on the charge of the particle. The friction force F_{fr} has a retarding impact. The coefficient of friction depends on the viscosity of the solution or the porosity of the matrix. At the equilibrium of these two forces, the charged analyte migrates with a constant velocity in the electric field (Gey, 2008c).

$$F_e = F_{fr} \rightarrow q \cdot E = f_c \cdot v \rightarrow v = \frac{q \cdot E}{f_c} = u \cdot E$$

Equation 13

u ..... Electrophoretic mobility [m^2 s^{-1} V^{-1}]

The resulting migration velocity is proportional to the electrophoretic mobility (u) and the electrical field strength (E). The electrophoretic mobility is unique for each molecule. It depends on the particle properties, such as charge, shape and size, the electrical field strength and solvent properties like ionic strength, viscosity, pH and temperature (Birdi, 2014).

The electrophoretic mobility in Equation 13 is valid for small, spherical particles. However, for non-spherical particles, like peptides and proteins, Equation 14 can be considered (Lottspeich and Engels, 2012b).

$$u = \frac{q}{M^{2/3}}$$

Equation 14

2.1.1. Capillary electrophoresis

When using capillary electrophoresis (CE), separation takes place in thin capillaries. The general setup consists of a capillary, a high voltage power supply, two electrodes, two buffer reservoirs and an on-column detector. Figure 19 displays a schematic illustration.

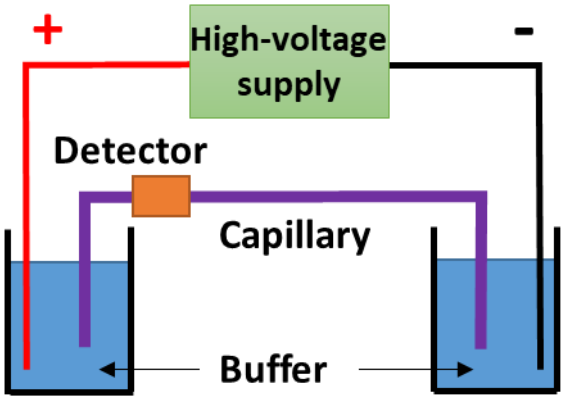

Figure 19: Schematic illustration of a capillary electrophoresis system.

Capillaries consist most commonly of fused silica, sometimes with modified inner walls. The inner diameter is usually between 50 and 100 µm. Its small diameter is crucial for enabling efficient heat dissipation. Furthermore, on the outside the capillary is coated with polyimide to enhance mechanical stability. Using an optical detector, the non-UV transparent polyimide coating needs to be removed at the spot where the detector is placed. Besides optical detectors like absorption or fluorescence detectors, others can be used e.g. mass spectrometers or conductivity detectors (Lottspeich and Engels, 2012c).

When using a fused silica capillary and a background electrolyte (BGE) with a slightly basic pH, silanol groups of the inner wall of the capillary deprotonate and immobilized negative charges are produced. These negative charges attract positive ions which are moreover attracted by the cathode when voltage is applied (Figure 18). By this an electroosmotic flow (EOF) is produced which is either counteracting or adding positively to the electrophoretic velocity of the charged analyte particles (Lottspeich and Engels, 2012c).

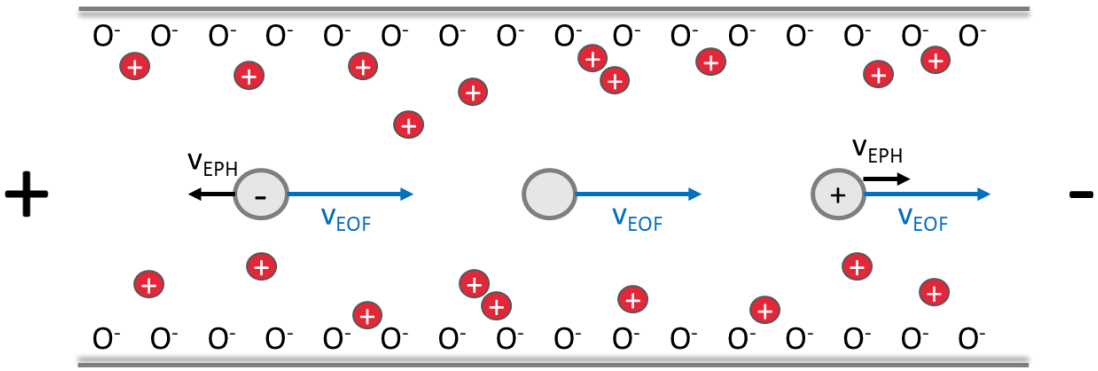

Figure 20: Principle of capillary electrophoresis: Migration of charged and neutral analytes within a capillary. (v_{EOF} electroosmotic velocity, v_{EPH} electrophoretic velocity) (source: Lottspeich and Engels (2012c))

The velocity of the EOF depends on the pH value of the BGE electrolyte. In case of very basic conditions, i.e. pH 9-10, the EOF can even exceeds the electrophoretic velocity of the analytes. Thus, not only positive ions are transported to the cathode but also neutral and negatively charged particles (Lottspeich and Engels, 2012c).

2.1.2. *Agilent* Bioanalyzer P80 Assay

The Bioanalyzer can be described as a chip based capillary gel electrophoresis. It can be used for sizing, quantification and quality control of proteinaceous components, DNA and RNA due to electrophoretic separation on the chip. Different kits for proteins, DNA and RNA are available.

In this thesis, the *Agilent* Bioanalyzer P80 Assay, a protein assay, was used. Proteins in a size range from 5 to 80 kDa are analyzed. The principle for capillary gel-electrophoresis on the chip, as commercialized in protein assays run on a Bioanalyzer, is similar to conventional SDS-PAGE, a standard method for protein analysis (Bousse et al., 2001).

Figure 21 shows a schematic illustration of the chip used in the Bioanalyzer P80 Assay. One chip consists of 16 wells. The different wells are connected through a network of micro channels, made of glass. The micro channels are filled with the separation buffer, containing the sieving material and the fluorescent dye.

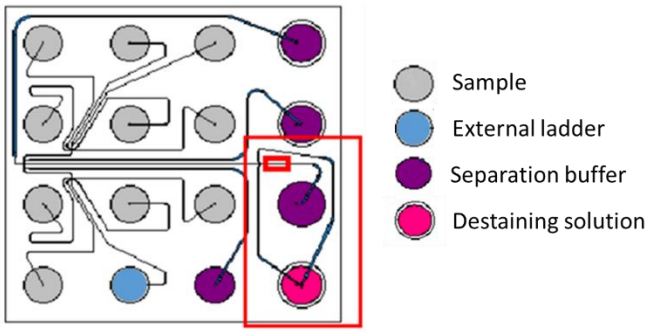

Figure 21: Schematic illustration of the chip used for the Agilent Bioanalyzer. (source: Kishawi (2008))

Before the sample is loaded onto the chip, proteins are denatured by adding dithiothreitol (DTT) and the sample buffer, containing sodium dodecyl sulfate (SDS) and the fluorescent dye, to the sample and heating it for 5 min at 95°C. The proteins form protein-SDS-micelles, in which the fluorescent dye is intercalated. Additionally, the sample buffer contains an upper and a lower marker as in internal standard to observe and correct migration variance. The detection of proteins with the *Agilent* Bioanalyzer 2100 is based on fluorescence. The *Agilent* Bioanalyzer 2100 has two excitation sources: 458-482 nm excitation with LED and 620-645 nm excitation with laser (Kishawi, 2008).

After the chip is loaded, it is placed into the *Agilent* Bioanalyzer 2100. 16 electrodes located in the cover lid of the instrument are then immersed in each well of the chip. The charged denatured protein-SDS-micelles are migrating through the micro channels binding additional fluorescent dye. Due to the SDS treatment of the proteins, they have a constant mass to charge ratio, thus separation is solely based on size. At the end of the separation channel, before the detection, a dilution step for the SDS-protein-dye-gel solution follows, whereby SDS is diluted below the critical micellar concentration and only protein-containing complexes survive. For the dilution, the destaining solution, containing sieving gel, is used. This step helps avoiding a high background and a better signal to noise ratio for the actual analyte of interest. Figure 22 displays a schematic illustration of the staining, destaining and detection process.

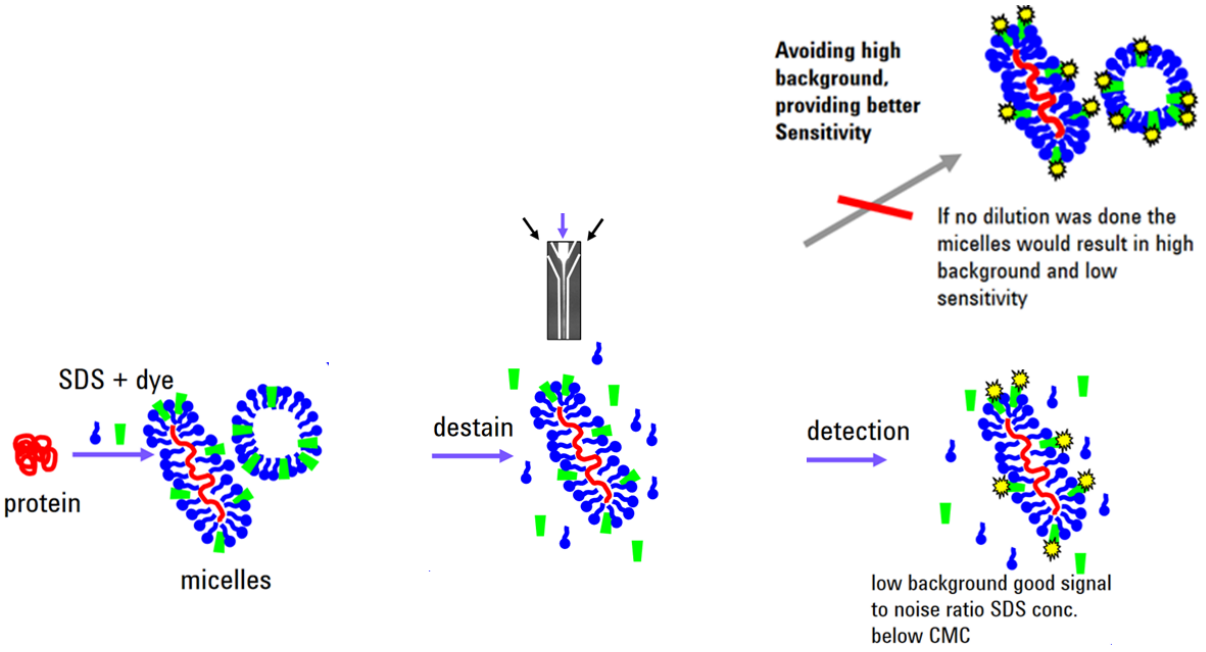

Figure 22: Schematic illustration of staining, destaining and detection. (source: Kishawi (2008))

2.2. Liquid chromatography

Liquid chromatography is a technique to separate, characterize, and purify various components in a mixture. Different components interact different with a stationary and a mobile phase depending on polarity. When Using high pressure, the process is called high performance liquid chromatography (HPLC).

The stationary phase is placed in a chromatographic column with a length usually between 5 and 30 cm and an inner diameter between 1 and 4 mm. The material of the stationary phase can be e.g. silica gel, aluminum oxide, polyamide etc. and must be adjusted to the analyte of interest. The sample is injected into the system with a six-way valve. The typical injection volume ranges between 1 and 50 µl. The sample containing mobile phase passes through the column and separation takes place due to interactions between the analyte and the stationary phase. Some analytes will interact stronger and thus, retain longer compared to others which pass faster through the column. Substances which do not interact at all with the stationary phase are called “dead time”. The mobile phase, e.g. methanol, acetonitrile, hexane, etc., may comprise of one solvent or a mixture. When using two mobile phases, an eluent gradient may be used. The composition of the mobile phase is changed from a low eluting power to a high one during a run. Hence, separation efficiency can be enhanced. To detect the analytes, various detectors can be used such us UV/Vis -, fluorescence -, electrochemical detector and mass spectrometry to name a few. Figure 23 shows a scheme of HPLC.

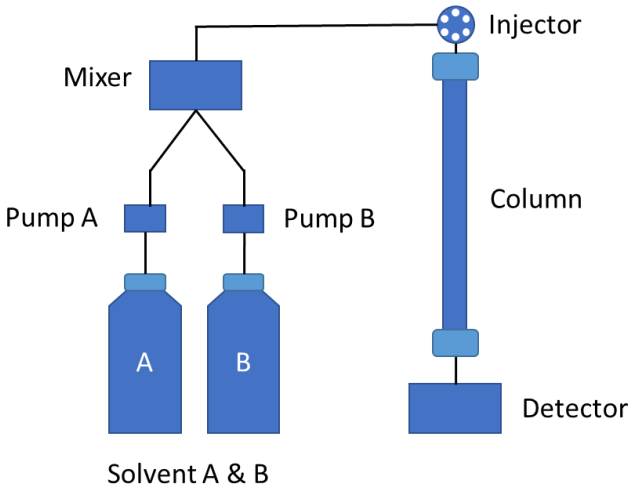

Figure 23: Schematic illustration of HPLC.

Selectivity in LC depends on the interactions between the mobile phase and the analytes as well as the stationary phase. High selectivity can be reached due to the ability to vary the properties of the mobile and the stationary phase. Depending on the polarity of the stationary phase compared to the mobile phase it is differentiated between normal phase chromatography and reverse phase chromatography. In case of normal phase chromatography, the stationary phase is polar (often silica gel SiO_2) and the mobile phase is relatively non-polar, such as hexane. Separation occurs due to adsorptive interactions between analytes and free silanol groups. Nowadays this method plays a minor role and is displaced by gas chromatography (GC). In reverse phase chromatography, the mobile phase is polar. Often a mixture of water and methanol or acetonitrile is used. For the non-polar stationary phase silanes with alkyl groups with different lengths (C_2 to C_{18}) are used. Analogue to SPE, reverse phase chromatography was used in this thesis.

2.5. Mass spectrometry

Mass spectrometry is an analytical technique to measure mass-to-charge ratios (*m/z*) of differently charged chemical species, to get information about mass, elemental composition and/or structure.

The sample is first ionized (negative or positive) in the ion source and transferred into the gas phase. In this first step, also fragmentation may occur. Afterwards, the ions are separated in the mass analyzer due to different *m/z* values. The detector measures the ion current and a mass spectrum is generated which displays the relative abundance of ions against the *m/z* (Pottiez, 2015). Figure 24 shows the basic setup of a mass spectrometer.

Figure 24: Schematic illustration of a mass spectrometer.

Ion source:

There are different ionization techniques that can basically be classified in hard and soft ionization techniques. In this thesis, Electrospray Ionization (ESI), a soft ionization technique, was used. Thus, this method will be explained.

In ESI, the fragmentation of the molecular ion in the ion source is low. It is suited for coupling of separation techniques like capillary electrophoresis (CE) or liquid chromatography (LC) to mass spectrometry (Hoffmann and Stroobant, 2007b) In this thesis LC-ESI-MS as well as tandem MS was performed.

For ionization in ESI the sample must be in a liquid phase. Ionization takes place at atmospheric pressure. The sample is injected to a capillary, where a voltage (3-6 kV) is applied between the capillary and the counter electrode. Hence, an electric field results and a liquid drop of charges (either mainly negative or positive, depending on the direction of the field) emerge at the tip of the capillary. By applying high voltage, the drop changes from a spherical shape to a “Taylor cone”. Just before the counter electrode, droplets are formed. During the movement of these droplets to the mass analyzer, neutral solvent molecules are evaporated by applying a heated, inert drying gas (often N_2). Thus, droplets get smaller and the surface charge per unit volume increases (Budzikiewicz and Schäfer, 2012). Hence, the droplets are reaching the Rayleigh-limit, which is described by the repelling Coulomb force of same charges and the surface tension of the solvent (Lottspeich and Engels, 2012d). The coulomb repulsion of same charges gets so high, that new, small droplets (daughter droplets) are formed (Coulomb explosion) (Budzikiewicz and Schäfer, 2012).

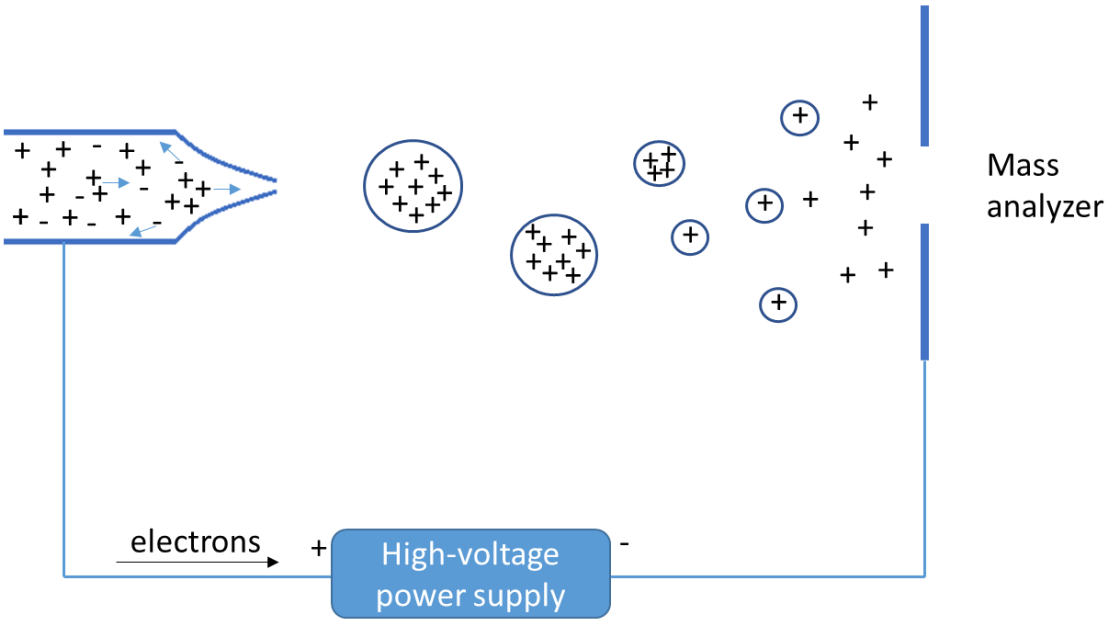

Figure 25: Scheme of the electrospray ionization (ESI) process for positive ions (charged-residue model).

There are two concepts for ionization: the charged-residue model (Dole et al., 1968) and the ion evaporation model (Iribarne and Thomson, 1976).

The charged-residue model:

Due to a series of coulomb explosion, the initially formed droplets form small droplets in the size of 1 nm, containing only one analyte molecule. Desolvation occurs by the curtain gas (e.g. N_2) (Lottspeich and Engels, 2012d).

Ion evaporation model:

Charged ions are directly ejected from the droplet into the gas phase (Lottspeich and Engels, 2012a).

Ions formed within the ESI process can be single or multiply charged. However, molecules with a mass below 1000 g/mol are usually single charged, whereas bigger molecules can have multiple charges (Hoffmann and Stroobant, 2007b).

Mass analyzer:

For the separation of ions, according to their *m/z* values, different mass analyzer (all under high vacuum) can be used. Quadrupole ion trap (QIT) was used in this thesis. Therefore, it will be explained in more detail.

An ion trap, also known as Paul trap, is a 3-dimensional ion trap trapping ions in a three-dimensional quadrupole field (Hoffmann and Stroobant, 2007c). The general setup of QITs consists of one ring electrode and two end cap electrodes. Both end cap electrodes have holes, allowing ions to enter and leave the trap (March, 1997). A schematic illustration of a QIT is seen in Figure 26.

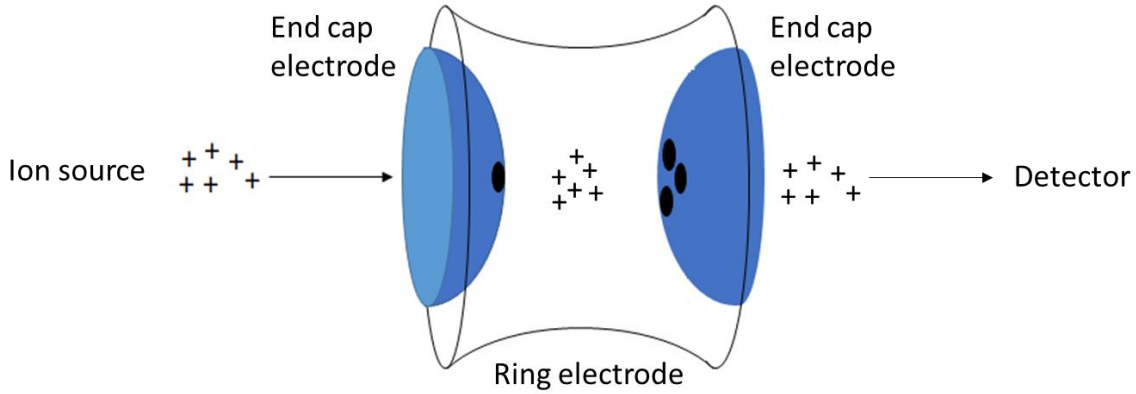

Figure 26: Schematic picture of a quadrupole ion trap (QIT).

In contrast to the end cap electrodes, which are held at ground, a high voltage RF (radio frequency) potential is applied to the ring electrode (March, 1997), resulting in a quadrupole field (Lottspeich and Engels, 2012d).

Ions, coming from the ion source, are passing through the end cap electrode getting captured in the ion trap between the end cap electrodes and the ring electrode on a stable orbit. Not only one specific ion with a certain *m/z* value gets trapped, but ions with different masses (Lottspeich and Engels, 2012d). A high mass range can be achieved by varying the alternating voltage (AC voltage) of the ring electrode. The number of analytes with different *m/z* values that can be trapped simultaneously is described by the Mathieu's equation. Details can be found in (Hoffmann and Stroobant, 2007c).

Since the ions are coming with a high velocity from the ion source and therefore high inner energy, helium gas is applied for cooling and slowing down the analyte ions. In this way, it can be prevented that ions just pass through the ion trap without getting trapped (Hoffmann and Stroobant, 2007c). Typically, ions are trapped for 0,1 to 10 ms. To prevent an overload of the QIT, the transfer line between the ion source and the trap is blocked by applying an electrical potential (Lottspeich and Engels, 2012d).

According to different *m/z* values, ions are ejected towards the detector (Hoffmann and Stroobant, 2007c). The ejection of ions can be achieved by increasing the amplitude of AC voltage or by using multi-pole fields (Lottspeich and Engels, 2012d).

Furthermore, tandem MS and multistage MS (MS^n) can be performed in the QIT. Selective masses are isolated and then excited for collision induced dissociation (CID). The advantage of performing MS/MS and MS^n in the QIT is that precursor ion selection and fragmentation occur in the same space (Hoffmann and Stroobant, 2007c). Therefore, QIT is a tandem-in-time instrument and no additional mass analyzers are needed for MS^n measurements.

At the end caps an alternating voltage, specific to an isolated *m/z* value is applied leading to excitation of the isolated ions. The excited ions take up energy from the dipolar field and start to collide with the introduced collision gas (He). The internal energy of the analyte ions increases and fragmentation occurs. Since the applied voltage for excitation is specific for an isolated m/z value, product ions are not fragmented and secondary fragmentation is supressed.

Detectors:

For detection of analyte ions an electron optical ion detector (EOID), called Daly detector, was used. With the Daly detector, both negative and positive ions can be detected. Ions coming from the mass analyzer are accelerated due to an applied high potential at the electrode (conversion dynode). Two conversion dynodes are used. When the ions hit the dynodes, secondary emission of electrons occur which will then move towards the phosphorescent screen (or scintillation depending on the system). There, electrons are converted into photons. A photomultiplier is then detecting the photons and an electric current result (Hoffmann and Stroobant, 2007a).

3. Experimental

3.1. Materials

Table 2: Materials used in the experiments.

Product	Abbreviation	Comment	Product#	Company
Ultra-pure water (ultra-high-quality water) produced with Millipore® F2MA54197E/ SIMSV0001	UHQ	Specific resistivity ≥ 17,5 MΩcm (25°C)	F2MA54197E/ SIMSV0001	Millipore S.A.S.
Betula pendula pollen (birch pollen)	BP	-	012515101	ThermoFisher Scientific, Allergon AB, Sweden
0,2 µm cellulose acetate membrane filter	-	-	5147-0061	VWR
C18 Supelco Discovery® DSC-18 SPE Cartridge	-	Bed wt. 500 mg, volume 6 ml	52604-U	Sigma-Aldrich
Methanol	MeOH	Purity: 99,9%	106035	Merck
n-hexane	-	Purity: ≥99,0%	83962.320	VWR
Brand® UV-cuvette micro 70 µl	-	-	7592 20	Sigma-Aldrich
3, 30, 100 and 300 kDa Pall Nanosep® centrifugal devices		Omega membrane: modified polyethersulfone on polyethylene substrate		Sigma-Aldrich
Boric acid	BH_3O_3	Purity: ≥99,5%	15660	Fluka
Sodium hydroxide pellets	NaOH	Purity: 99,5-100,5 %	106482	Merck
Sodium dodecyl sulfate	SDS	Purity: ≥99,5%	A2263,1000	AppliChem

0,2 µm cellulose acetate/surfactant-free membrane filter	-	-	16534K	Sigma Aldrich
Dimethyl sulfoxide	DMSO	Purity: 99,9%	D8418-50ML	Sigma Aldrich
Benzoic acid	-	Purity: ≥99,0 %	12350	Fluka
LiChrosolv water for chromatography	-	-	Z0331233 431	Merck
Acetonitrile	AcN	Purity: 99,9%	83640.290	VWR
Formic acid	FA	Purity: 98,0%	1.00264.1000	Merck

3.2. Instrumentation

Table 3: Instruments used in the experiments.

Instrument	Company
Sigma 2-16P centrifuge	Sigma Laborzentrifugen (Osterode am Harz, Germany)
Olympus BX51M optical light microscope	Olympus (Tokio, Japan)
Hengtech MDC320 microscope camera	Hengtech (Viernheim, Germany)
DC Power supply Rigol DP800A	Rigol Technologies (Beijing, China)
Quick-cool QC-31-1.4-3.7M Peltier-element	Quick-OHM Küpper & Co (Wuppertal, Germany)
Thermocouple PCE-T312 (type K)	PCE Instruments (Meschede, Germany)
Thermocouple measurement device NI USB-TC01	National Instruments (Austin, TX, USA)
EHEIM universal water pump	EHEIM (Deizisau, Germany)
Vacuum centrifuge Univapo 100H with Unicryo MC2L -60°C coldtrap	Uniequip (Planegg, Germany)
Implen Nanophotometer classic	Implen (Munich, Germany)
Sigma 1-14 centrifuge	Sigma Laborzentrifugen (Osterode am Harz, Germany)

Agilent Bioanalyzer 2100	Agilent Technologies (Santa Clara, CA, USA)
Capillary Electrophoresis CE G1600AX	Agilent Technologies (Santa Clara, CA, USA)
FE20/EL20 Benchtop pH Meter	Mettler Toledo (Schwarzenbach, Switzerland)
Sigma 3-30K centrifuge with rotor no. 12154	Sigma Laborzentrifugen (Osterode am Harz, Germany)
Hitachi LaChrom Elite® HPLC-System with L2200 autosampler module and L2300 column oven	VWR (Radnor, PA, USA)
Column: LiChrospher 100 RP18 endcapped; ø 2 mm, length: 125 mm, particle size: 5 µm, pore size: 100 Å	Merck Millipore (Darmstadt, Deutschland)
Bruker Daltonics Esquire 3000^{plus} ion trap mass spectrometer	Bruker Daltonics (Billerica, MA, USA)

3.3. Sample preparation

For the analysis, birch pollen washing water (BP-WW) was prepared. Materials and instruments used are listed in chapter 3.1 and 3.2. The ultra-pure water is abbreviated with UHQ.

Preparation of BP-WW:

- 500 mg birch pollen were provided in a 15 ml plastic vessel
- 10 ml of UHQ were added (carefully to prevent dust formation)
- The mixture was left for 5 hours and shaken 2 to 3 times
- The suspension was centrifuged for 5 min with 1120 *xg*
- The supernatant was decanted and filtrated with a 0,2 µm syringe filter

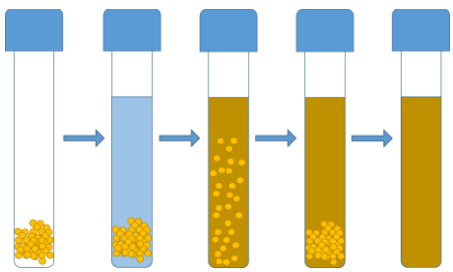

Figure 27: Schematic illustration of the preparation of BP-WW.

The BP-WW obtained was further used for analysis.

3.4. Freezing experiments - VODCA

For the measurements of the freezing behavior of BP-WW itself and other fractions obtained from SPE and centrifugal filtration, the setup VODCA, as described in 2.1, was used. The setup consists of an optical light microscope, a camera connected to a computer, a power supply, a cryo-cell, including a Peltier-element, a reservoir with water, ice and a pump, a gas supply (N_2) and dry air is used. Figure 28 shows the experimental setup.

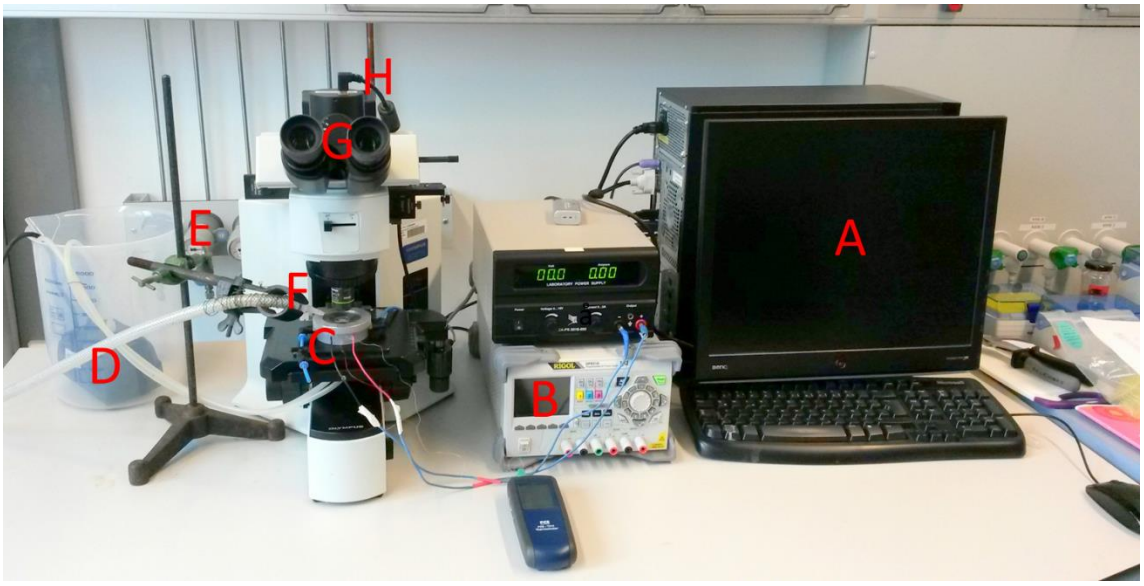

Figure 28: Cryo-microscopy setup VODCA including A) a computer, B) power supply, C) cryo-cell, D) pump and ice water bath, E) gas supply (N_2), F) dry air, G) microscope and H) a camera.

The water-in-oil emulsion sample as described in chapter 2.1 was prepared on a cover glass, which was put onto the Peltier-element. By increasing the current flow, the top of the Peltier-element and hence, the cover glass containing sample was cooled down. Cooling started from temperatures above 0°C. The freezing event was overserved with a microscope and a camera, connected to the computer. The freezing of the droplets was seen by the change of the color of the droplets to a dark one (Figure 12). Between the measurements the cryo-cell was flooded with N_2 to keep the cell dry. Dry air is directed onto the glass of the cell in order to avoid fogging. Measurements took place at four different positions at the cover glass.

With the camera and the software *LabVIEW* videos were recorded during the measurement as well as pictures were taken at certain temperatures.

Detailed procedure:

- On the cover glass 2 µl of the sample were mixed with 4 µl of an oil mixture (90 wt% paraffin and 10 wt% lanolin) using a pipette tip and put onto the Peltier-element in the cryo-cell
- The lid of the cryo-cell was closed, dry air was directed onto the lid and with the program LabView a cooling rate is defined to decrease temperature and initiate freezing
- Videos and pictures were taken during the freezing process (LabView)
- Before the next measurement, the cryo-cell was flooded with N_2

Two data analysis methods were used during this thesis: pictures and videos were taken.

Picture analysis:

Pictures were taken during the whole freezing process at certain temperatures. The first one was taken when no droplets are frozen. The last one at a temperature where all droplets are frozen. In every single picture, the number of frozen droplets per picture/temperature were counted and noted. To get the number of frozen droplets per temperature Equation 15 was applied.

$$frozen\ droplets\ (T)[\%] = \frac{n_T}{n_{total}} * 100$$

Equation 15

n_T ..... Number of frozen droplets up to temperature T

n_{total} ..... Total number of frozen droplets

Figure 29 displays the sample droplets at different temperatures. Depending on the state of aggregation, droplets scatter light differently. Frozen droplets appear dark, liquid ones bright.

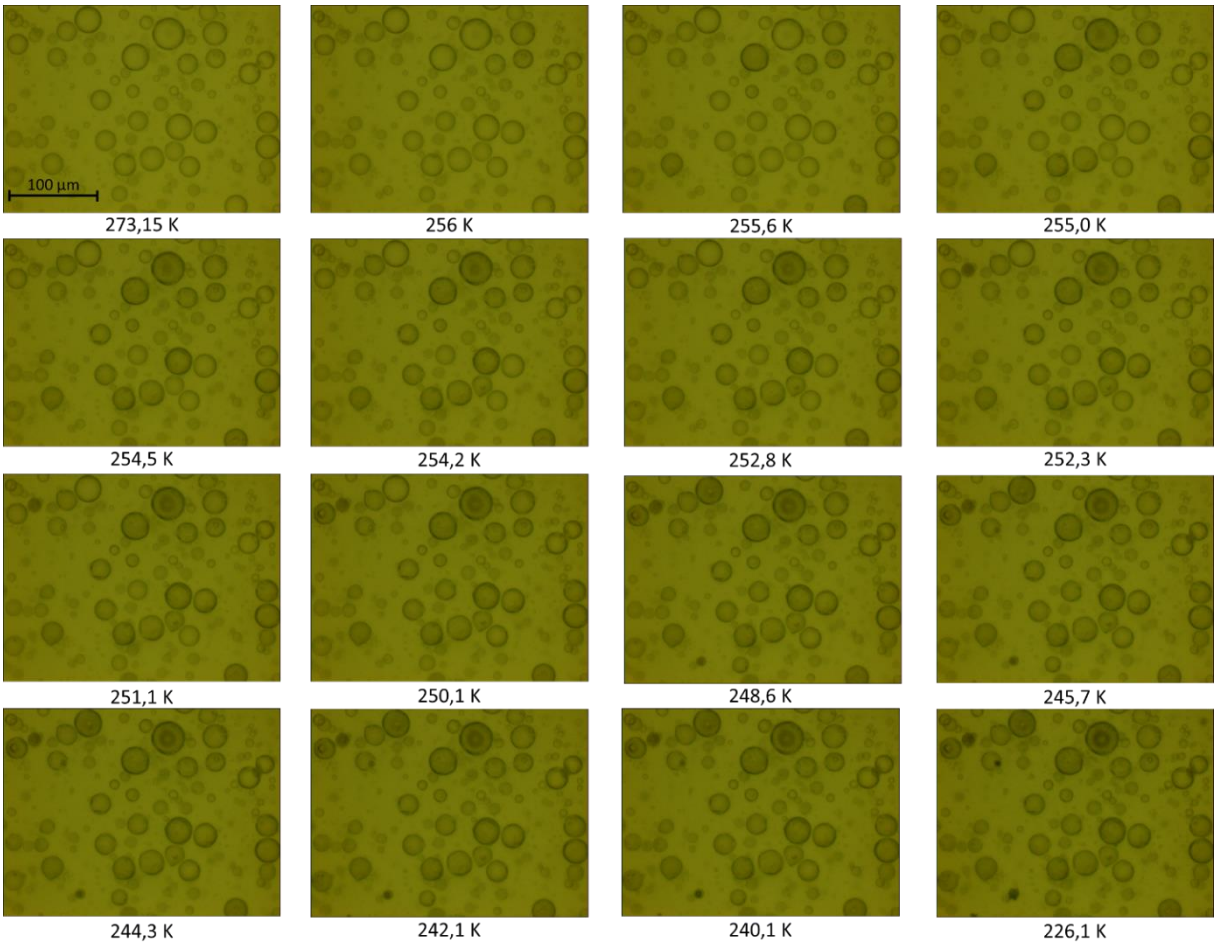

Figure 29: BP-WW droplets at different temperatures. The dark droplets are frozen, the bright ones are still liquid.

Video analysis:

The videos were observed in slow motion to detect at which temperature droplets froze. The evaluation of the frozen droplet fraction was done analog to the picture analysis. For the evaluation, droplets in the size range of 10 to 50 µm were counted. The fraction of frozen droplets was then plotted against the respective temperature resulting in a freezing curve. Figure 30 displays the freezing curve of ultra-pure water.

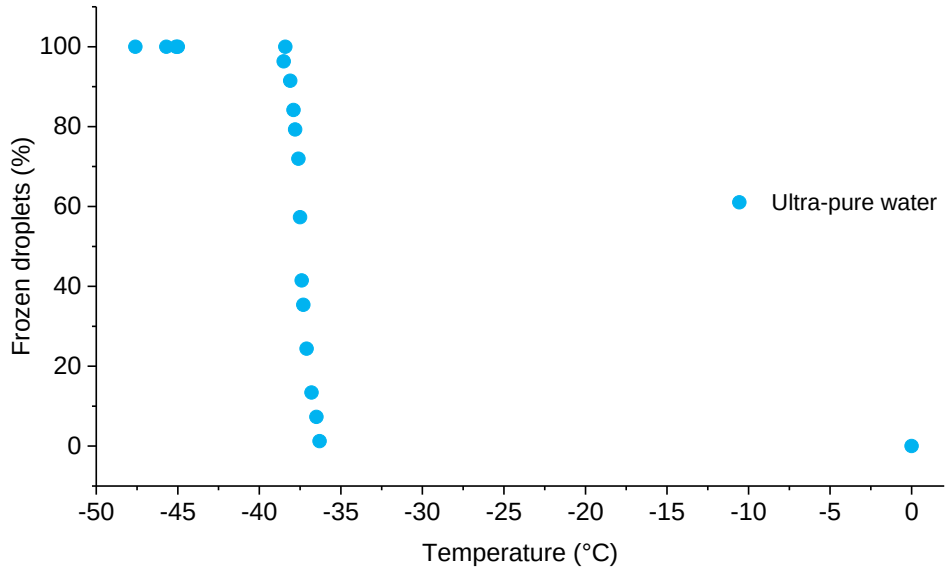

Figure 30: Freezing curve of ultra-pure water.

Before the measurements of samples, an ultra-pure water (specific resistivity: 18,2 MΩcm (25°C)) emulsion was analyzed to make sure the setup was working properly.

To be able to compare ice nucleation activity of different samples, the median freezing temperature (T_{50} value) has been used. The T_{50} shows the temperature at which half of the droplets are frozen. For samples where droplets froze homogeneously as well as heterogeneously just the heterogeneously frozen part was used for the calculation of the T_{50} value.

3.5. Solid phase extraction

SPE was used to reduce sample complexity of BP-WW using fractionated elution from analytes adsorbed to C_{18} material. Obtained fractions were further analyzed for ice nucleation activity (INA) with the VODCA setup as described in chapter 2.1 and 3.4.

Procedure:

- Conditioning: 1,5 ml ultra-pure water (UHQ) were pipetted into the cartridge containing C_{18} material. By applying vacuum, the UHQ passed slowly through the sorbens (One drop per second). It was ensured that the sorbens did not run dry.

- Flow through: 500 µl BP-WW + 1 ml UHQ were mixed and then pipetted into the same cartridge used in the conditioning step. Again, by carefully applying vacuum, the sample slowly passed through the sorbens. It was ensured that the sorbens did not run dry. The fraction was collected in a plastic vessel.
- Fraction 1: 1,5 ml 20 vol% MeOH were pipetted into the prepared cartridge. Analytes were eluted by applying vacuum. Again, it was ensured that the sorbens did not run dry. The fraction was collected in a plastic vessel.

The procedure for the next fractions was analog to the one described above, but different solvent compositions with increasing concentrations of organic solvent were used:

- Fraction 2: 1,5 ml 40 vol% MeOH
- Fraction 3: 1,5 ml 60 vol% MeOH
- Fraction 4: 1,5 ml 100 vol% MeOH
- Fraction 5: 1,5 ml 100 vol% n-hexane

The solvent of the collected fractions (flow through – fraction 5) was evaporated using the vacuum centrifuge for approx. 5 hours. Each remaining residue was dissolved in 250 µl UHQ and further used for ice nucleation testing. Figure 31 displays a schematic illustration of the SPE of BP-WW.

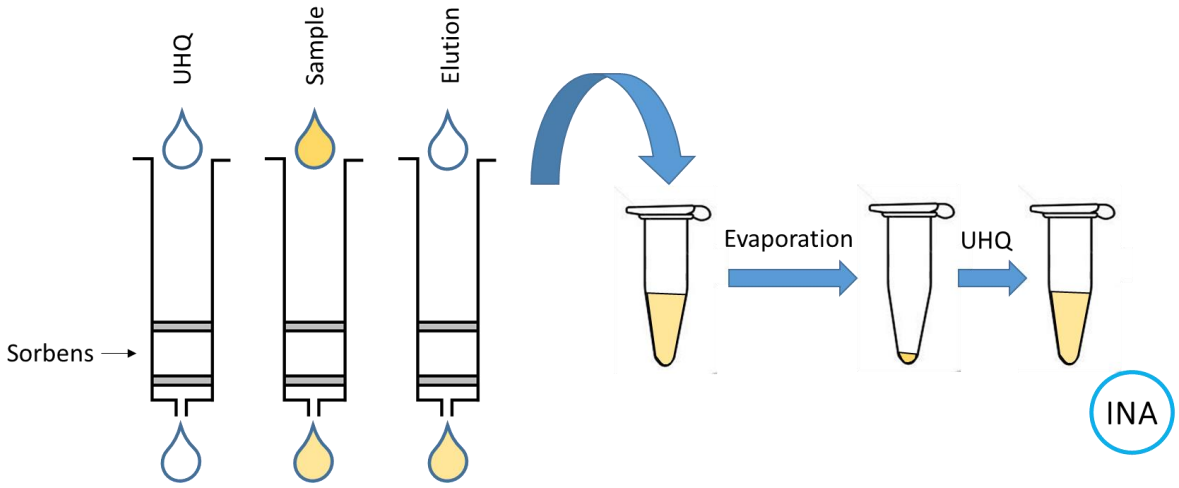

Figure 31: Schematic illustration of solid phase extraction of BP-WW.

Materials and instruments used for SPE are listed in chapter 3.1 and 3.2.

3.6. UV/Vis spectroscopy

Absorption spectra of BP-WW and SPE fractions were recorded using an *Implen* Nanophotometer.

For the measurements 70 µl UV-cuvettes as well as a sub microliter cell (nanodrop) were used. The samples were diluted 1:40 (2 µl sample + 78 µl UHQ).

Procedure cuvettes:

- The photometer and the computer were turned on
- The program *PVC Nano Photometer* is opened
- A water blank (70 µl UHQ) was measured, followed by the measurements of the diluted samples
- The spectra obtained were opened with the program *PVC Viewer* and exported as *.csv and further edited in *Origin Pro 9.1*

The procedure for the sub microliter cell was done analog, however instead of 70 µl, 2 µl were used. A schematic illustration of the sub microliter cell is pictured in Figure 32.

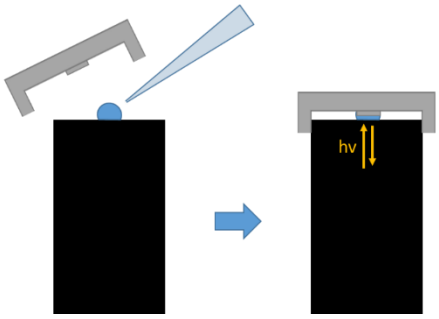

Figure 32: Schematic illustration for the UV/Vis absorption measurements using the sub microliter *cell (nanodrop).*

Details about materials and instrumentation are listed in chapter 3.1 and 3.2.

3.7. Centrifugal filtration

Single centrifugal filtration was performed on the one hand to gain information about the size of IN and on the other hand to separate IN from substances which are not ice nucleation active. Therefore, filters for different molecular weight cut-offs (MWCO) were used. Furthermore, repeated filtration (washing steps with UHQ) was performed for further purification.

3.7.1. Single filtration

3, 30, 100 and 300 kDa MWCO Pall Nanosep® centrifugal device filters with the filter material Omega™ membrane consisting of modified polyethersulfone on a polyethylene substrate were used.

Procedure:

- 350 µl of BP-WW were pipetted onto the spin filter and the tube was weighed (starting weight)
- The filter was put into the centrifuge and rotated at specific parameters (Table 4)
- The filtrate was transferred into a plastic tube and the retentate was weighed again (end weight)
- The difference between the starting and the end weight was calculated
- According to the calculated mass difference, UHQ was added to the retentate to get the same volume as in the beginning. The volume from the retentate and filtrate was then compareable.
- The filtrate and retentate were further analyzed for ice nucleation activity

Parameters used for respective MWCO filters are listed in Table 4.

Table 4: Parameters for single centrifugal filtration of BP-WW.

Filter cut-off	Rcf [*xg*]	Temperature [°C]	Time [min]	Sample name	
				Retentate	Filtrate
3 kDa	9000	15	60	*3 kDa Retentate I*	*3 kDa Filtrate I*
30 kDa	9000	15	10	*30 kDa Retentate I*	*30 kDa Filtrate I*
100 kDa	9000	15	1	*100 kDa Retentate I*	*100 kDa Filtrate I*
300 kDa	4000	15	1,5	*300 kDa Retentate I*	*300 kDa Filtrate I*

3.7.2. Repeated filtration (n=3)

For further reduction of sample complexity and purification *3, 30 and 100 kDa Retentate I* was filtrated again using 3, 30 and 100 kDa MWCO filters (see Figure 33).

Procedure:

- 250 µl of each *Retentate I* were pipetted onto new MWCO filters (details seeTable 5) and weighed (starting weight). (*3 kDa Retentate I* on a new 3 kDa MWCO filter, *30 kDa Retentate I* on a new 30 MWCO kDa filter etc.)
- 250 µl UHQ were added
- The samples were centrifuged according to paramters given in Table 5
- After centrifugation, the filtrate was separately collected in a plastic tube. 500 µl UHQ were added to the retentate and centrifugation was repeated. In total, three filtrates were collected (a schematic scheme of the procedure is showed in Figure 33)
- Finally, the retentate was weighed again (end weight) and the difference between starting and end mass was calculated
- According to this mass difference, UHQ was added to the retentate
- Only the third retentate and filtrate (denoted as *x kDa Retentate II* and *x kDa Filtrate II.3*) were further analyzed for ice nucleation activity

In order to be able to compare the retentates with the filtrates and BP-WW, the volume of the retentate was filled up to its starting volume to prevent concentration.

Table 5: Parameters for repeated centrifugal filtration of 3 kDa-, 30 kDa- and 100 kDa Retentate I.

Filter cut-off	Rcf [*xg*]	Temperature [°C]	Time [min]	Sample name	
				Retentate	Filtrate
3 kDa	9000	15	40	3 kDa *Retentate II*	3 kDa *Filtrate II.3*
30 kDa	9000	15	10	30 kDa *Retentate II*	30 kDa *Filtrate II.3*
100 kDa	9000	15	0,5	100 kDa *Retentate II*	100 kDa *Filtrate II.3*

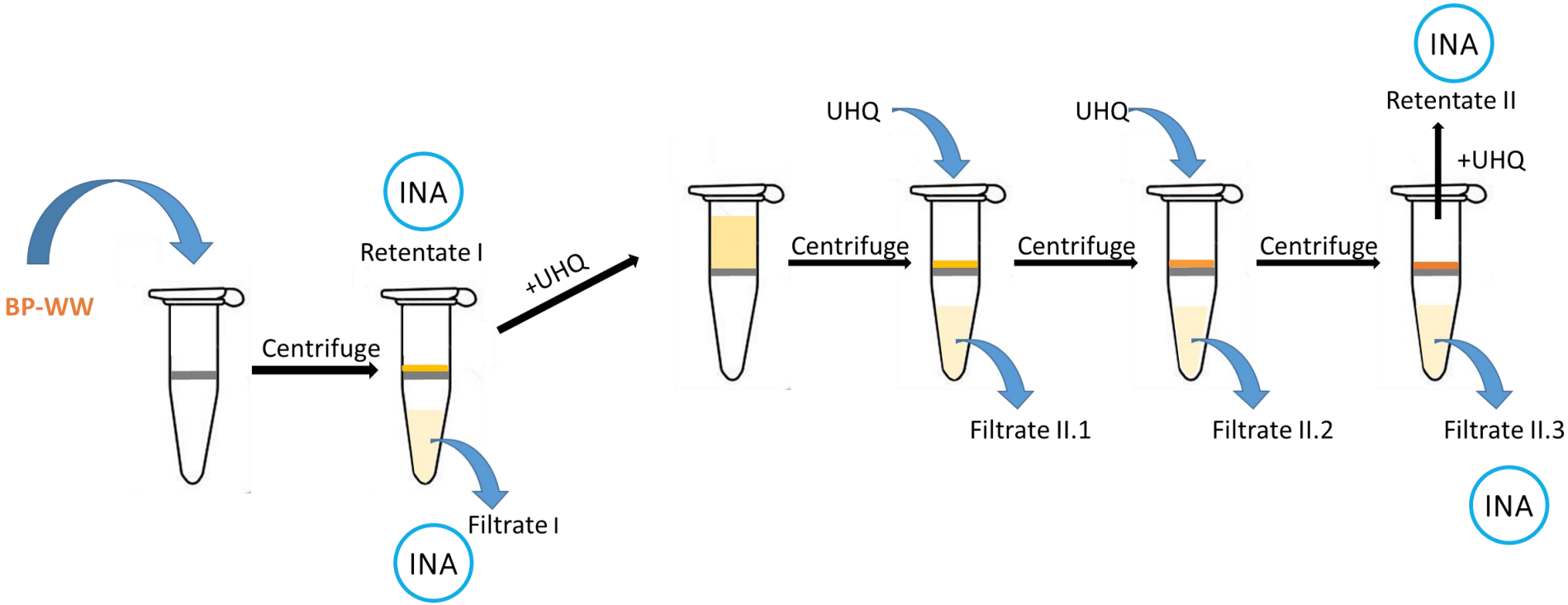

Figure 33: Schematic illustration of performed centrifugal filtration of BP-WW. Spin tube filters pictured have the same cut-off (either 3-, 30-, 100- or 300 kDa MWCO filter). Compounds marked with INA are analyzed for ice nucleation activity.

3.8. Capillary electrophoresis

Fractions obtained from SPE and samples after MWCO filter separation were analyzed by capillary electrophoresis (CE). 1,2 µl aliquots of each SPE fraction (chapter 3.5) and 4,8 µl filtrate and respective retentate (chapter 3.7) were used for analysis.

The materials used are listed in chapter 3.1. The parameters for the measurements are shown in Table 6.

Table 6: Parameters for capillary electrophoresis.

Capillary	Fused silica Inner diameter: 50 µm Outer diameter: 360 µm
Temperature	22,5°C
Electric field strength	33 kV/m
Background electrolyte (BGE)	200 mM sodium borate with 10 mM SDS, pH=8,4
Detector	UV/Vis

Preparation of the background electrolyte (BGE):

100 ml of a 200 mM sodium borate buffer pH 8,4 with 10mM SDS was prepared.

- 3 M NaOH solution for pH adjustment: 1,2 g of sodium hydroxide pellets were dissolved in 10 ml UHQ
- 200mM boric acid solution containing 10mM SDS:
  1,2366 g of boric acid (H_3BO_3) and 0,2884 g SDS were weighed in a glass bottle and dissolved in 80 ml of UHQ. The pH was adjusted to 8,4 with 3M NaOH and UHQ was added to reach 100 ml. Before use the buffer was filtered with a cellulose acetate syringe filter (pore size 0,2 µm).

As EOF markers, benzoic acid and dimethyl sulfoxide (DMSO) were used. The concentrations of the markers are listed in Table 7.

Table 7: EOF markers.

EOF marker	concentration
Benzoic acid	400 ug/ml
DMSO	5,5 mg/ml

For the measurements, a blank, a standard and samples were prepared as provided in Table 8 and Table 9. Each mixture had a total volume of 12 µl. Table 8 shows the pipetting scheme for analysis of the fractions obtained from SPE and Table 9 for the analysis of the samples obtained from centrifugal filtration.

Table 8: Pipetting scheme for SPE samples.

Blank	Standard	Sample
10,8 µl BGE 1,2 µl UHQ	9,6 µl BGE 1,2 µl UHQ 0,6 µl benzoic acid 0,6 µl DMSO	9,6 µl BGE 1,2 µl sample 0,6 µl benzoic acid 0,6 µl DMSO

Table 9: Pipetting scheme for centrifugal filtration samples.

Blank	Standard	Sample
7,2 µl BGE 4,8 µl UHQ	5,8 µl BGE 4,8 µl UHQ 0,6 µl benzoic acid 0,6 µl DMSO	5,8 µl BGE 4,8 µl sample 0,6 µl benzoic acid 0,6 µl DMSO

The instrument *Agilent G1600AX* capillary electrophoresis system was used for the measurements.

Figure 34: Agilent G1600AX capillary electrophoresis system.

Autosampler:

450 µl of 1 M NaOH, UHQ and three BGE were filled in different vials. One vial was left empty (waste). The vials were then put into the autosampler of the CE in a specific order. Figure 35 shows the sequence of the vials in the autosampler.

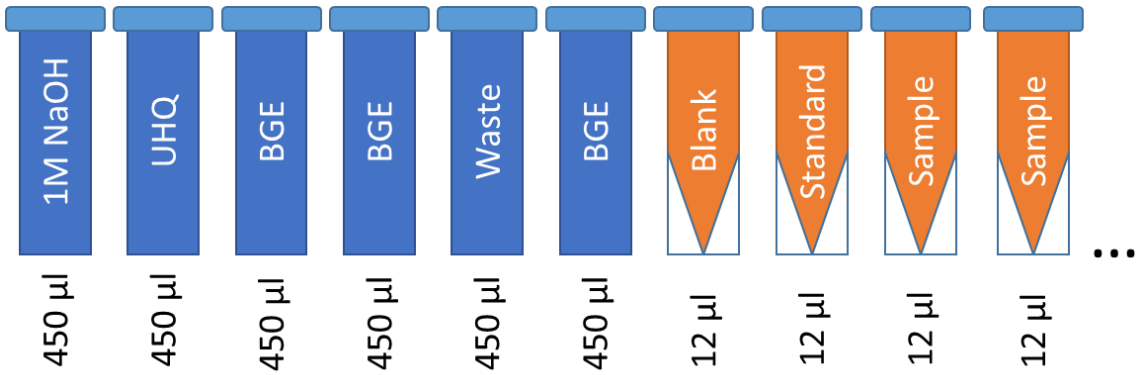

Figure 35: Sequence of vials in the autosampler (CE).

Procedure measurements:

- The CE system and the PC were started
- The program *Agilent 3D-CE ChemStation (Instrument online)* was opened
- In the beginning, the system needed to be initialized (Instrument/ System INIT)
- To check if the system was leakproof, UHQ was flushed through the capillary
- Before the measurements, the capillary was flushed with 1M NaOH followed by UHQ and BGE
- The system was then ready for analysis and samples could be measured

For detection a UV/Vis detector was used. The data evaluation was done in *Agilent 3D-CE ChemStation (Instrument offline)*. The spectra were then exported as *.csv and opened and edited with *Origin Pro 9.1*.

After the analysis, the capillary was flushed with UHQ for 5 min.

3.9. *Agilent* Bioanalyzer P80 Assay

For further analysis of BP-WW, the *Agilent* Bioanalyzer P80 kit was used. Components of the kit and reagents used are displayed in Figure 36.

Protein 80 Kit (reorder number 5067-1515)	
Protein Chips	**Protein 80 Reagents (reorder number 5067-1516) & Supplies**
25 Protein Chips	● (red) Protein 80 Gel-Matrix (4 vials) in box labelled Part I. Store at 4 °C
1 Electrode Cleaner	● (blue) Protein 80 Dye Concentrate* in box labelled Part I. Store at 4 °C
	❍ (white) Protein 80 Sample Buffer (4 vials) in box labelled Part II. Store at -20 °C
Syringe Kit	● (yellow) Protein 80 Ladder in box labelled Part II. Store at -20 °C
1 Syringe	4 Spin Filters

Figure 36: Reagents used, working with the Agilent Bioanalyzer P80 kit.[2]

Preparation of the Gel-Dye Mix:

- 650 µl of Protein 80 Gel-Matrix were transferred to a spin filter and centrifuged at 2500 *xg* for 15 min
- 25 µl of the well vortexed fluorescent dye were added to the filtrated and centrifuged gel and mixed for 20 s with the vortexer

Preparation of the destaining solution:

- 650 µl of Protein 80 Gel-Matrix were transferred to a spin filter and centrifuged at 2500 *xg* for 15 min

Preparation of the denaturing solution:

- 1 µl of dithiothreitol (DDT) were added to 28,6 µl sample buffer and vortexed for 5 s

The sample analyzed with the *Agilent* Bioanalyzer 2100 was concentrated BP-WW (initial concentration: 250 mg/ml).

Preparation of the samples and the ladder:

- 4 µl of the sample and 2 µl denaturing solution were mixed in a 0,5 ml vial
- Samples and the protein ladder were heated up to 95°C for 5 min using the thermomixer
- After the solutions were cooled down, the vials were centrifuged for 15 s
- To each sample/ladder 84 µl UHQ were added and vortexed

[2] http://www.agilent.com/cs/library/usermanuals/Public/G2938-90062_Protein80_AG_KG.pdf

Cleaning procedure of the Bioanalyzer:

Before measurements, the electrodes of the Bioanalyzer were cleaned. Therefore, a cleaning chip was filled with 380 µl UHQ and placed into the instrument. The lid was closed for 5 minutes. After opening the lid, the chip was removed and the lid was left open for 30 s.

Chip Priming Station:

- The priming station needed to be at position A. The syringe clip must be adjusted to the middle position

Loading of the chip:

- A new chip was placed on the chip priming station
- 12 µl of the gel-dye-mix were pipetted into well G (upper right-hand corner)
- The plunger was put at 1 ml and the chip priming station was closed.
- The plunger was pressed until it is held by the clip and after 60 s of waiting the clip was released
- After 5 s waiting, the plunger was pulled back to 1 ml and the priming station was opened again
- 12 µl of gel-dye-mix were pipetted into all “G” labeled wells
- 12 µl of destaining solution were pipetted into well “DS”
- 6 µl of the protein ladder were pipetted into the well labeled with the ladder symbol
- Lastly, 6 µl of each sample were pipetted into the 10 remaining wells

Figure 37: Chip used for protein analysis with the Agilent Bioanalyzer.

After the chip was loaded, it was placed in the Bioanalyzer. To start the run, the program *Agilent 2100 Expert* was used. The electropherogram was exported as a csv. file and further edited in *Origin Pro 9.*1.

3.10. LC-ESI-MS/MS^n

The flow through obtained from SPE (see chapter 3.5) and filtered samples, *3kDa Filtrate II.3* and *3 kDa Retentate II* (description in chapter 3.7) were measured by LC-ESI-MS. Furthermore, MS/MS and MS^3 were carried out for structural characterization of selected analytes detected in BP-WW. For the measurements, the samples were not diluted and used as they were prepared in chapter 3.5 and 3.7.

3.10.1. HPLC separation

Details about the instrument and column used are described in chapter 3.2. The parameters for the measurements with HPLC are listed in Table 10.

Table 10: Chromatography parameters used in HPLC for measuring the samples.

Parameter	Setting
Flow rate	0,400 µl/min
Injection volume	10 µl
Oven temperature	30°C
Mobile Phase A	Water containing 12 mM formic acid
Mobile Phase B	Acetonitrile containing 12 mM formic acid
UV/Vis Detector	205 nm

For the analysis, the mobile phase gradient shown in Figure 38 was used.

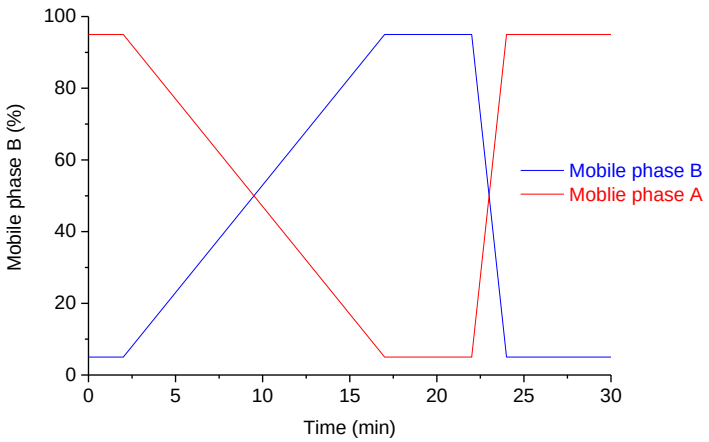

Figure 38: Mobile phase gradient used for HPLC measurements

Table 11 displays the mobile phase gradient in numbers.

Table 11: Mobile phase gradient used for HPLC measurements.

Time [min]	Mobile phase A [%]	Mobile phase B [%]
0	95	5
2	95	5
17	5	95
22	5	95
24	95	5
30	95	5

Solvents used for HPLC are described in chapter 3.1. To ensure that substances bind to the stationary phase, the separation starts with an isocratic profile of 2 min for 5% mobile phase B. In accordance with SPE, the high organic content is kept constant for 5 min to ensure complete elution of analytes from the column. Finally, the gradient decreases to the initial level, 5 % mobile phase B and 95 % mobile phase A.

3.10.2. ESI-QIT parameters and settings

For ESI-QIT analysis, four different methods were developed (denoted as method 1 to 4). The parameters and settings are listed in Table 12, Table 13, Table 14 and Table 15.

Table 12: Parameters and setting for ESI-QIT measurements (Method 1).

Unity	Parameter	Setting
Source	Nebulizer	17,0 psi
	Dry gas	12,0 l/min
	Dry temperature	300°C
	Polarity	Positive
	Target mass	1600 *m/z*
Trap	Scan mode	Standard normal
	Smart target	20000
	Max. accu time	400 ms
	Scan range	100 – 2000 *m/z*
	Ramp range	From - 4500 V to - 1500V
	Collision gas	Helium

Table 13: Parameters and setting for ESI-QIT measurements (Method 2).

Unity	Parameter	Setting
Source	Nebulizer	16,0 psi
	Dry gas	10,0 l/min
	Dry temperature	300°C
	Polarity	Positive
	Target mass	200 *m/z*
Trap	Scan mode	Standard normal
	Smart target	20000
	Max. accu time	200 ms
	Scan range	50 – 1500 *m/z*
	Ramp range	From - 4500 V to - 1500V
	Collision gas	Helium

Table 14: Parameters and setting for ESI-QIT measurements (Method 3).

Unity	Parameter	Setting
Source	Nebulizer	10,0 psi
	Dry gas	10,0 l/min
	Dry temperature	300°C
	Polarity	Negative
	Target mass	900 *m/z*
Trap	Scan mode	Standard normal
	Smart target	10000
	Max. accu time	200 ms
	Scan range	100 – 2000 *m/z*
	Ramp range	From - 4500 V to - 1500V
	Collision gas	Helium

Table 15: Parameters and setting for ESI-QIT measurements (Method 4).

Unity	Parameter	Setting
Source	Nebulizer	16,0 psi
	Dry gas	10,0 l/min
	Dry temperature	300°C
	Polarity	Negative
	Target mass	150 *m/z*
Trap	Scan mode	Standard normal
	Smart target	10000
	Max. accu time	200 ms
	Scan range	50 – 1500 *m/z*
	Ramp range	From - 4500 V to - 1500V
	Collision gas	Helium

Since unknown compounds were analyzed, samples were measured in both, positive and negative ion mode and the developed methods show high sensitivity for different m/z ranges. As scan mode “standard normal” with an average scan speed of 13.000 amu /s and a FWHM of 0,6 was used. The “smart target” defines the maximum number of ions trapped in the QIT during one cycle. Both, HPLC and MS, were operated by *Bruker Daltonics Esquire* software. For the data evaluation, the program *Data Analysis™ Version 3.2* was used.

BP-WW (50 mg/ml) was used for further structural analysis LC-ESI-MS, and infusion experiments by ESI-MS/MS and ESI-MS^3. The fragmentation amplitude was between 0,2 and 1 V. As a collision gas, helium was used.

4. Results and discussion

4.1. Birch pollen washing water

4.1.1. Freezing curve

The freezing behavior of BP-WW was analyzed with the cryo-microscopy setup VODCA as described in chapter 2.1 and 3.4. The preparation of the BP-WW sample is described in chapter 3.3. Figure 39 displays the freezing curve of ultra-pure water and BP-WW.

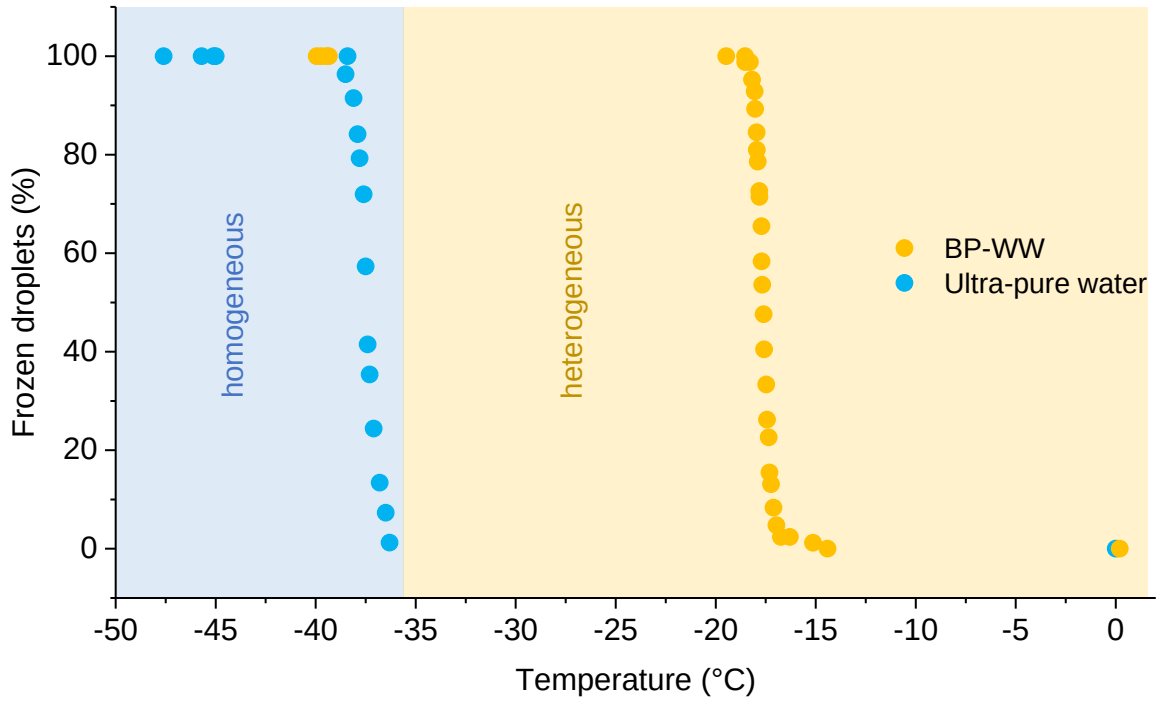

Figure 39: Freezing curve of ultra-pure water and BP-WW. Ultra-pure water freezes homogeneously, BP-WW heterogeneously.

As discussed in chapter 1.4, homogeneous freezing starts at temperatures between -36°C and -38°C. The graph above shows, that ultra-pure water freezes homogeneously. In contrast, BP-WW freezes heterogeneously. The T_{50} value for BP-WW is -17, 5°C which is comparable with literature (Pummer et al., 2012, Dreischmeier et al., 2017). Pummer et al. (2012) reported a median freezing temperature (T_{50}) of -18°C and Dreischmeier et al. (2017) a T_{het} of -18°C and -22°C.

4.1.2. UV/Vis spectrum

An absorption spectrum (wavelength from 200 to 900 nm) of BP-WW was recorded as described in chapter 3.6.

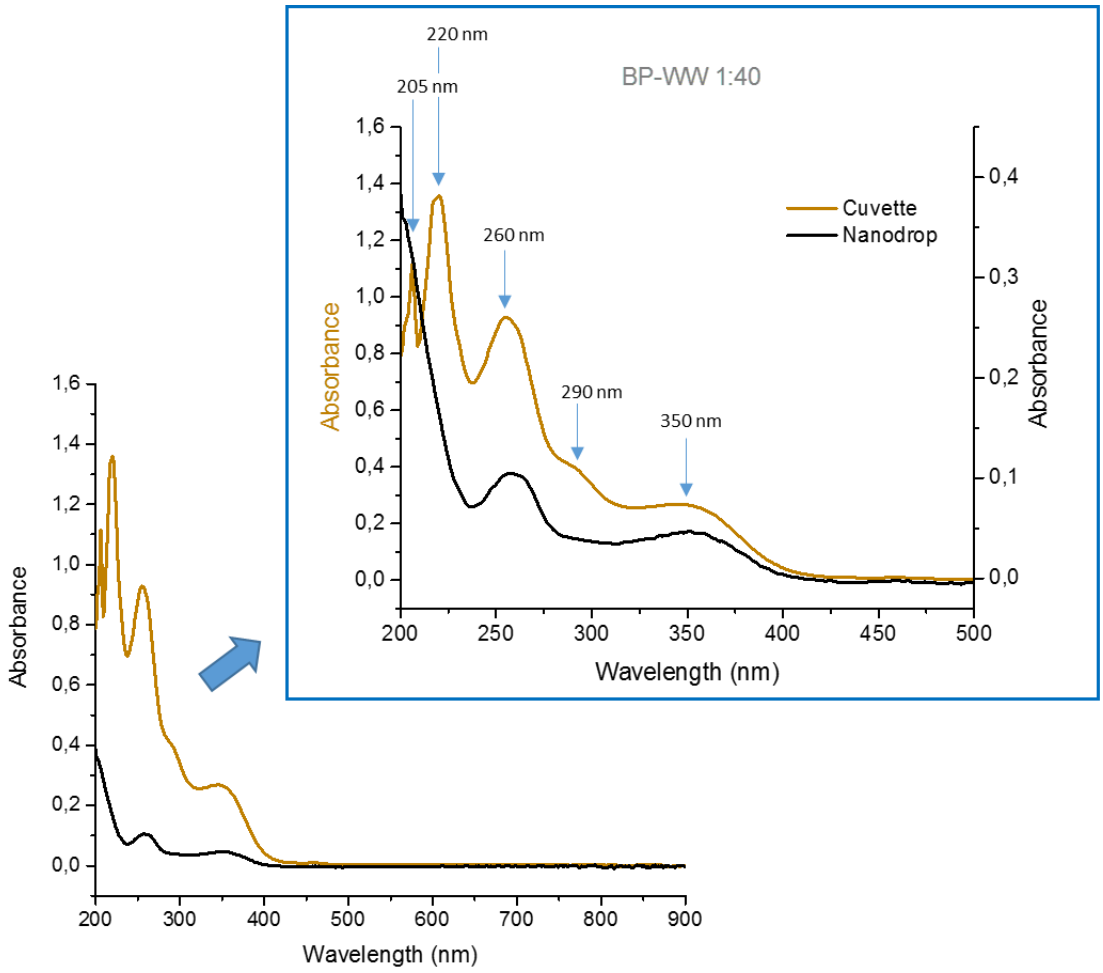

Figure 40: UV/Vis wave scans (200 – 900 nm) of BP-WW, 1:40 diluted with ultra-pure water (c=1,25 mg/ml). The brown curve displays the absorption bands when measuring with a plastic cuvette, the black curve when measuring with a sub microliter cell (nanodrop).

For the measurements, a plastic cuvette as well as a sub microliter cell (nanodrop) was used. In Figure 40, the brown curve represents the absorption spectrum of BP-WW using the cuvette, the black curve using the nanodrop. When comparing the absorption spectra, more bands are visible for the measurements carried out with the cuvette. There, BP-WW shows five absorption maxima at 205, 220, 260, 290 and 350 nm. These maxima indicate different substances within the BP-WW. However, the cuvette has a low transmission from 200 to around 210 nm. Thus, the maxima at 205 nm and 220 nm are pseudo maxima. In contrast to the cuvette, the nanodrop does not have a cut-off at 210 nm. There, maxima at 260 nm and

350 nm are visible. Further, a signal at 290 nm is seen for the measurements with the cuvette, but not for the one recorded with the nanodrop.

4.1.3. *Agilent* Bioanalyzer P80 Assay

To get information about potentially present protein species and the size of such compounds in BP-WW, the *Agilent* Bioanalyzer P80 Assay was used as described in chapter 2.1.2 and 3.9. The electropherogram recorded is displayed in Figure 41.

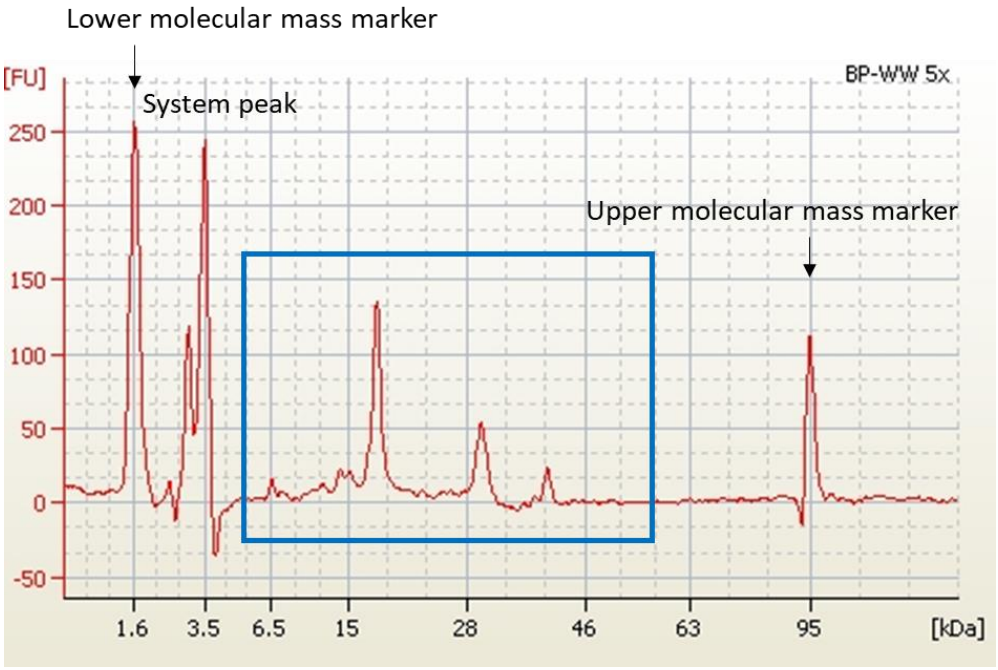

Figure 41: Electropherogram of BP-WW (250 mg/ml) analyzed with the Agilent Bioanalyzer P80 Assay. The first peak (1,6 kDa) displays the lower molecular mass marker, whereas the last peak (95 kDa) shows the upper molecular mass marker. Peaks at 2,6, 3,1 and 3,5 kDa and the negative followed are so-called system peaks. Peaks resulted from BP-WW are surrounded in blue.

The *Agilent* Bioanalyzer P80 Assay is normally used for the analysis of proteins. However, migrating substances seen in Figure 41 do not have to be necessarily of proteinaceous origin, because all compounds which interact with SDS can be analyzed with this method. A more detailed picture of the electropherogram of BP-WW is shown in Figure 42.

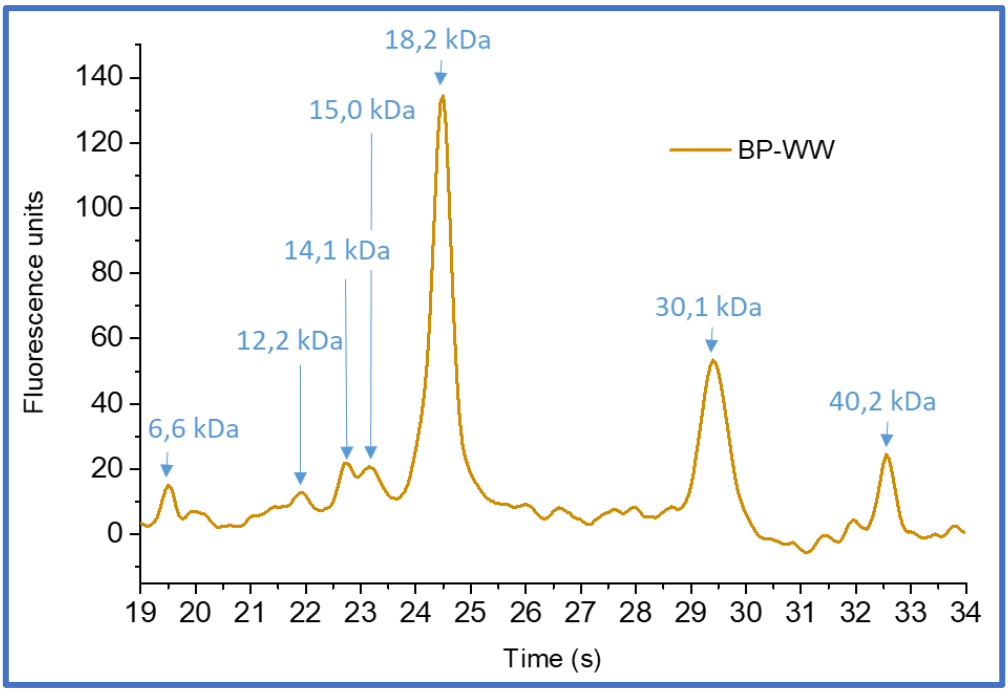

Figure 42: Section of the electropherogram of BP-WW (250 mg/ml) analyzed with the Agilent Bioanalyzer P80 Assay.

Compounds with sizes between 6,6 and 40,2 kDa were found. The most intense peak is at a migration time of 24,5 s, displaying the size of 18,2 kDa. It is known that birch pollen contain the allergen Bet v1 (Ipsen and Lowenstein, 1983). The size of the allergen protein is about 17 kDa (Hoffmann-Sommergruber et al., 1997, Spangfort et al., 1996, Swoboda et al., 1995). Since a deviation of up to 15% of the determined molecular weight is possible using this method, it is likely that the 17 kDa peak represents Bet v1. However, previous results from our working group showed that Bet v1 is not ice nucleation active. Hence, it was concluded that the allergen is no IN.

4.2. Solid phase extraction

To reduce the sample complexity of BP-WW, SPE, as described in chapter 2.3 and 3.5, was used. Fractions obtained after elution of compounds with increasing methanol concentration as well as n-hexane from C_{18} SPE cartridges were further analyzed for ice nucleation activity, using the setup VODCA as described in chapter 2.1 and 3.4. The obtained freezing curves are shown in Figure 43.

4.2.1. Freezing curves

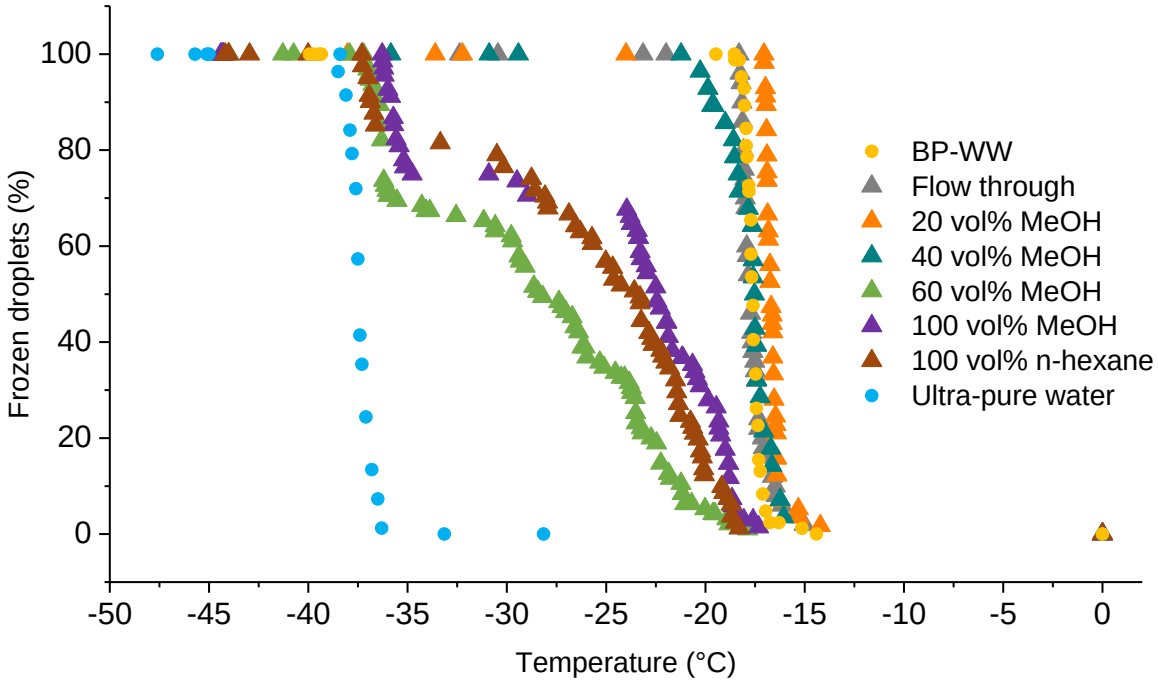

Figure 43: Freezing curves of the fractions obtained from SPE, BP-WW (50 mg/ml) and ultra-pure water.

The median freezing temperatures (T_{50} values) are summarized in Table 16.

Table 16: T_{50} values of the fractions obtained from SPE.

Sample	T_{50} [°C]
BP-WW	-17,5
Flow through	-17,8
20 vol% MeOH	-16,7
40 vol% MeOH	-17,5
60 vol% MeOH	-25,3
100 vol% MeOH	-21,4
100 vol% n-hexane	-23,6

To the far left in blue in Figure 43, the freezing curve of ultra-pure water can be seen, which represents homogeneous ice nucleation. The freezing curve of BP-WW (50 mg/ml) is pictured in yellow. Both, the ultra-pure water and BP-WW, were not treated with SPE and serve as references. Furthermore, the freezing curves of the flow through, the 20 vol%- and 40 vol% MeOH fraction have the same onset temperature of freezing as BP-WW. In addition, the T_{50} values for these fractions indicate that their ice nucleation ability is about the same. Nonetheless, the 20 vol% MeOH fraction has a lower T_{50} value as the remaining factions. The

60 vol%-, 100 vol%- MeOH fraction and the 100 vol% n-hexane fraction show a flattened curve compared to the freezing curves of the fractions mentioned before. Previous research results in our working group showed that the flattening of freezing curves correlates with a decrease in the number of IN. Further, 20-30% of droplets froze homogeneously. However, the majority of the droplets froze within the heterogeneous area. Thus, those fractions are still ice nucleation active.

For the elution, different concentrations of the polar MeOH as well as the non-polar n-hexane was used. All fractions obtained showed ice nucleation activity i.e. every fraction contains IN. Since IN interact with both the polar MeOH and the non-polar n-hexane, it is thought that IN may have amphiphilic properties.

4.2.2. CE

Fractions obtained from SPE were further analyzed with CE as described in chapter 2.4 and 3.8. The electropherograms of all fractions are shown from Figure 44 to Figure 50. Figure 44 displays the electropherogram of BP-WW.

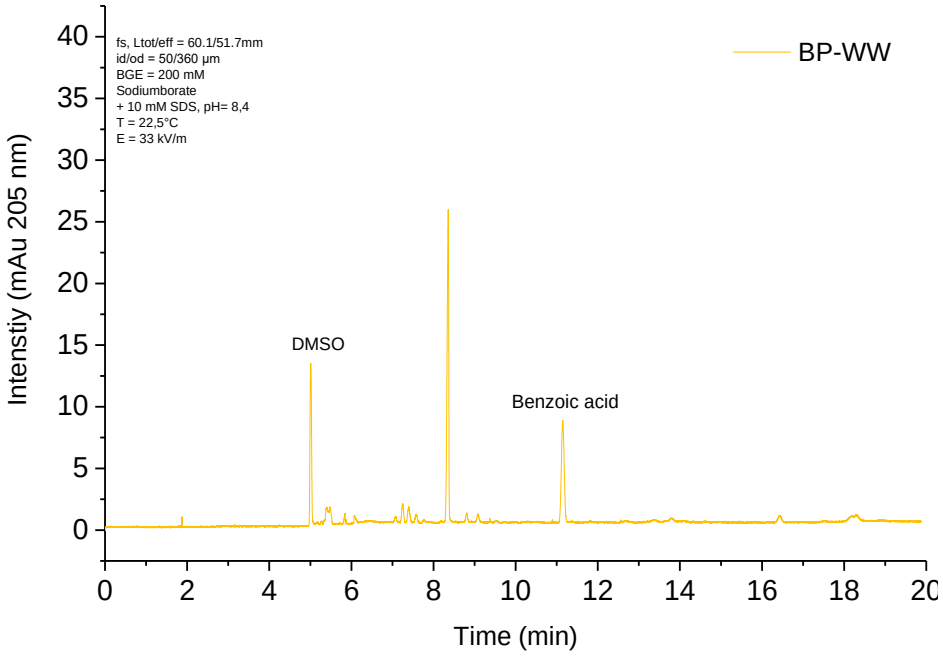

Figure 44: Electropherogram of BP-WW analyzed with capillary electrophoresis. DMSO and benzoic acid were used as EOF markers.

DMSO and benzoic acid serve as EOF markers. There is one peak which is outstanding with its high intensity at a migration time of 8,4 min. The electropherogram of the flow through is pictured in Figure 45.

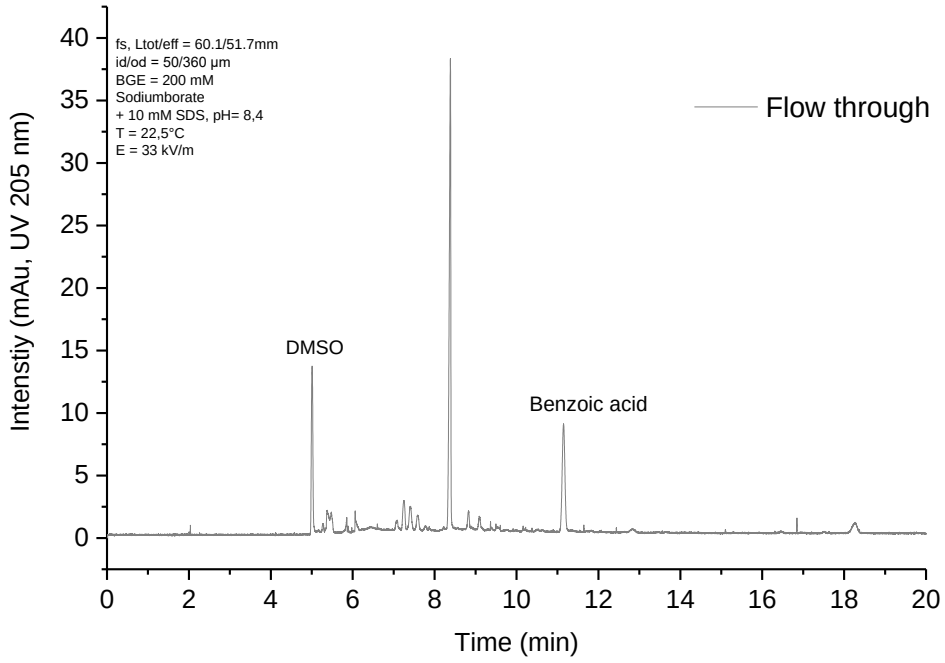

Figure 45: Electropherogram of the flow through analyzed with capillary electrophoresis. DMSO and benzoic acid were used as EOF markers.

Comparing the electropherogram of the BP-WW and the flow through, peaks are more intense for the flow through (excluding the marker peaks). Looking at the highest peak at a migration time of 8,4 min, it has an intensity of 26 mAu for BP-WW and 38 mAu for the flow through. The reason for this lies in the SPE treatment of the flow though. The solvent of the collected flow through was evaporated after the SPE. The residue was then dissolved in half of the volume from the beginning. Since BP-WW was not treated with SPE, no concentration was made. Thus, the signals of the flow through are higher than of BP-WW. The electropherogram of the 20 vol% MeOH fraction is pictured in Figure 46.

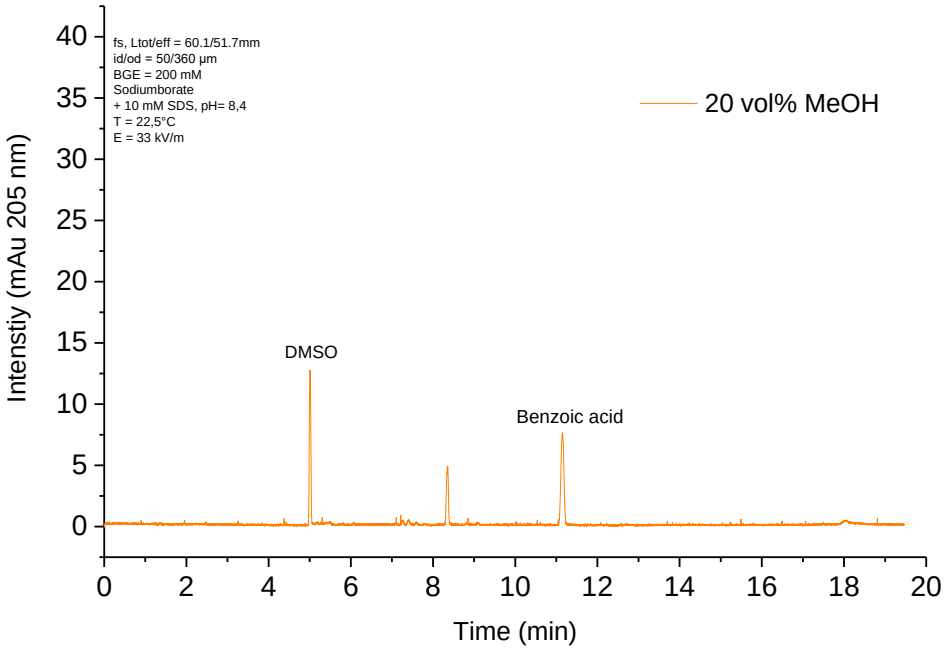

Figure 46: Electropherogram of the 20 vol% MeOH fraction analyzed with capillary electrophoresis. DMSO and benzoic acid were used as EOF markers.

The intensity of the peaks has decreased significantly compared to the electropherograms of BP-WW (Figure 44) and the flow through (Figure 45). Basically, there is just one peak at a migration time of 8,4 min. The electropherogram of the 40 vol% MeOH fraction is pictured in Figure 47.

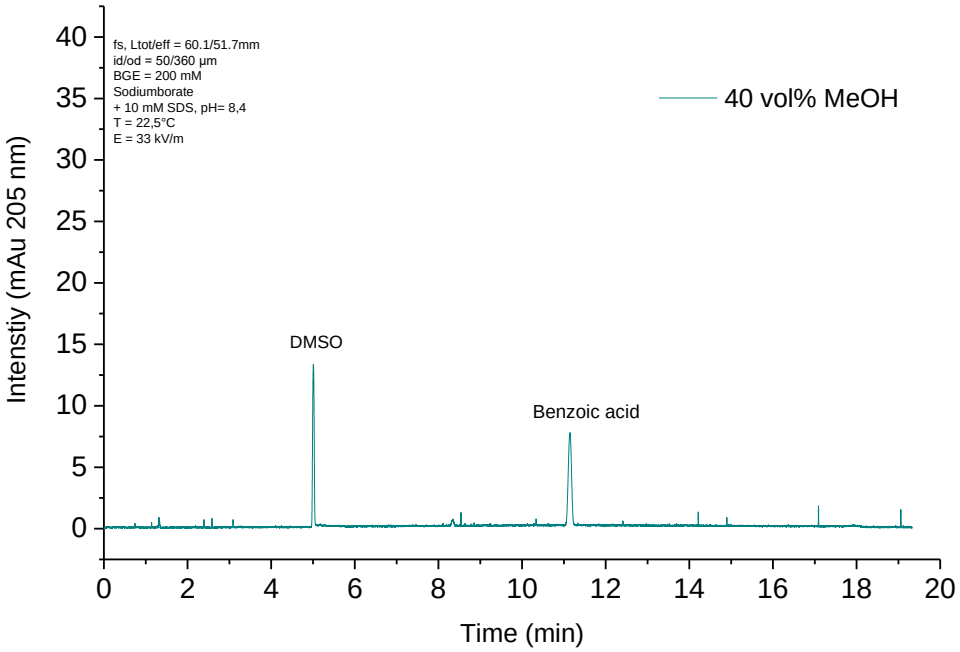

Figure 47: Electropherogram of the 40 vol% MeOH fraction analyzed with capillary electrophoresis. DMSO and benzoic acid were used as EOF markers.

In the electropherogram of the 40 vol% fraction nearly no signal below 1 mAu is visible. Just one small peak at 8,4 min migration time.

Although freezing curves showed IN activity the following electropherograms showed no UV signals (205 nm) for SPE fractions eluted with 60 vol% (Figure 48) and 100 vol% MeOH (Figure 49) or with 100 vol% n-hexane (Figure 50) except the EOF markers.

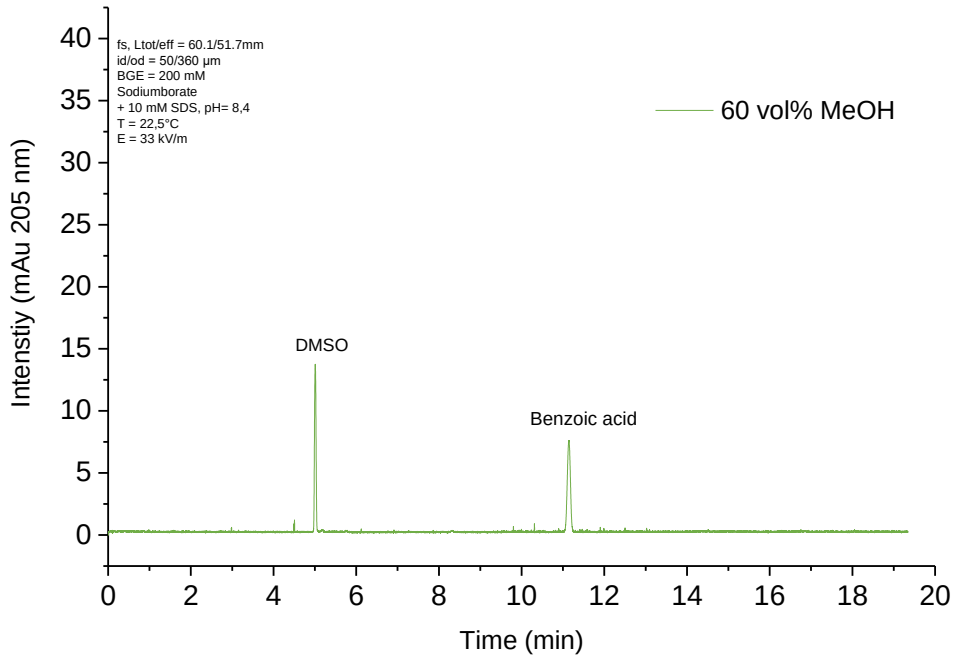

Figure 48: Electropherogram of the 60 vol% MeOH fraction analyzed with capillary electrophoresis. DMSO and benzoic acid were used as EOF markers.

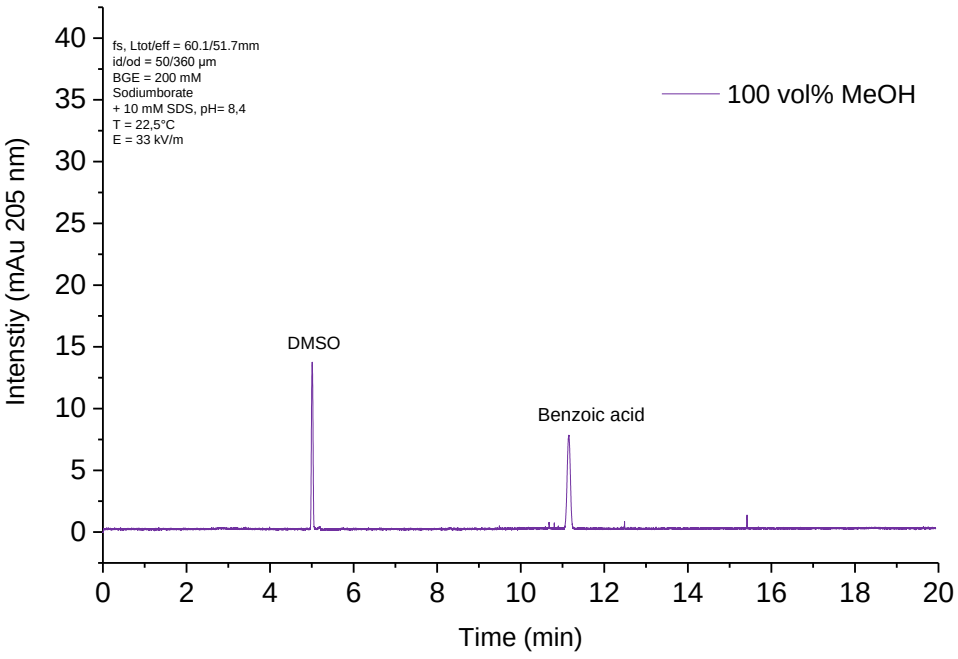

Figure 49: Electropherogram of the 100 vol% MeOH fraction analyzed with capillary electrophoresis. DMSO and benzoic acid were used as EOF markers.

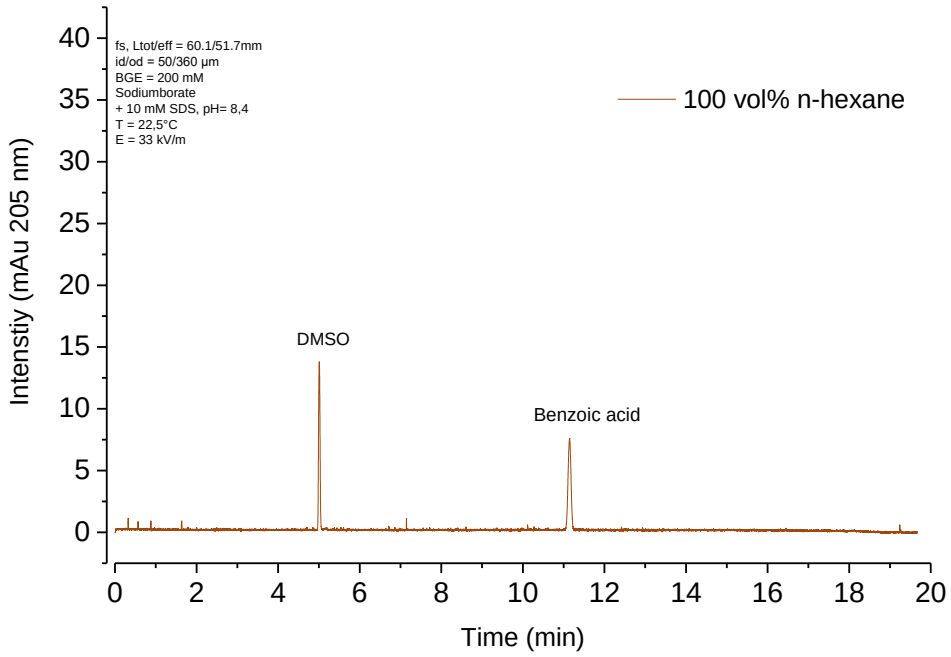

Figure 50: Electropherogram of the 100 vol% n-hexane fraction analyzed with capillary electrophoresis. DMSO and benzoic acid were used as EOF markers.

Although IN have to be present no signal except the EOF markers are observed. The reasons for this are manifold: (a) the concentration of the potentially UV active substances is too low, (b) the IN is not UV active at all or (c) does not absorb light at 205 nm.

4.2.3. UV/Vis spectra

Absorption spectra in the range from 200 to 900 nm were recorded from the fractions obtained from SPE. The experiment is described in detail in chapter 2.2 and 3.6.

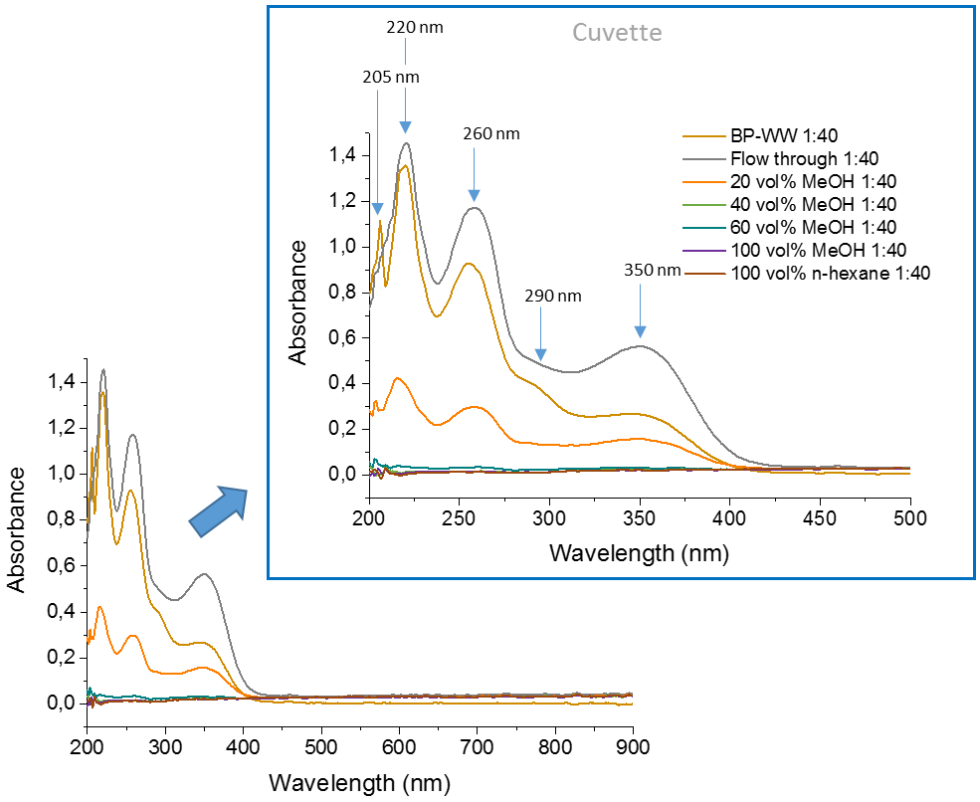

Figure 51: UV/Vis spectra of BP-WW (1:40 diluted with ultra-pure water; c=1,25 mg/ml) and SPE fraction 1-5 (1:40 diluted with ultra-pure water). Wave scan from 200 to 900 nm. Measurements were carried out with a 70 µl cuvette.

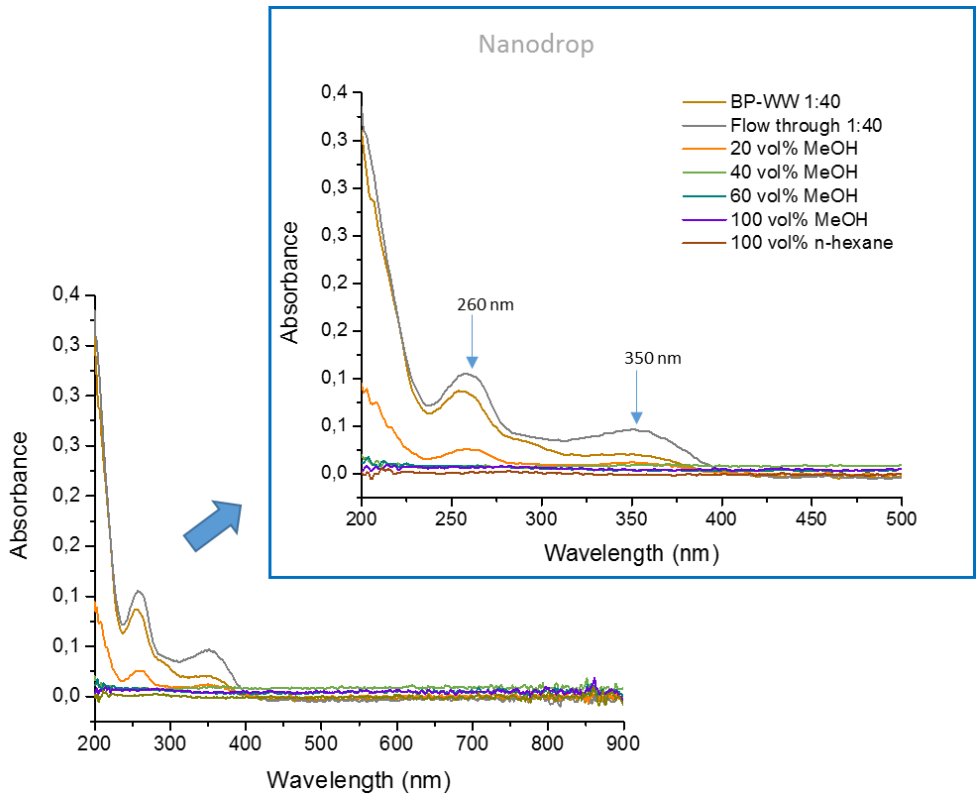

Figure 52: UV/Vis spectra of BP-WW (1:40 diluted with ultra-pure water; c=1,25 mg/ml) and SPE fraction 1-5 (1:40 diluted with ultra-pure water). Wave scan from 200 to 900 nm. Measurements were carried out with a sub microliter cell.

As already mentioned in 4.1.2, absorption spectra were recorded with both the cuvette and the sub microliter cell (nanodrop). In Figure 51, were the cuvette was used, the flow through fraction and BP-WW have the highest signals. The maxima of the flow through and the 20 vol% MeOH fraction are at 220, 260 and 350 nm. Since the cuvette has a cut-off at 210 nm, the 220 nm peak is a pseudo maximum. The UV/Vis spectrum using the nanodrop as well as the one recorded with CE (see Figure 68) confirms that no maximum at 220 nm is visible. The remaining fractions do not show significant maxima. The spectra in Figure 52 show the same tendency as before. For the BP-WW, the flow through and the 20 vol% MeOH fraction measured with the nanodrop, signals at 260 and 350 nm are visible.

Comparing the UV/Vis signals to the UV signal (measured at 205 nm) from CE (chapter 4.2.2), in both cases the flow through has the highest signals, followed by BP-WW. The reason for this lies in the SPE treatment of the flow though. The solvent of the collected flow through was evaporated after the SPE. The residue was then dissolved in half of the volume from the beginning. Since BP-WW was not treated with SPE, no concentration was made. Thus, the signals for the flow through are higher than for BP-WW. The 40 vol% MeOH fraction shows a small peak in the electropherogram measured with the CE. However, in the absorption spectrum recorded with the photometer, no signal is observed. The 60 vol%-, 100 vol% MeOH fraction and the 100 vol% n-hexane fraction do not show signals in both, the electropherograms of the CE and the absorption spectra. However, the freezing curves in Figure 43 show that all fractions are ice nucleation active. Hence, the IN from birch pollen may not be UV active or the concentration of IN, if UV active, is too low for detection.

4.3. Filtration

Single centrifugal filtration was performed on the one hand to gain information about the size of IN and on the other hand to separate IN from inactive substances using filters for different molecular weight cut-offs (MWCO). Furthermore, repeated filtration (washing steps with UHQ) was performed for further purification of IN. The experiment is described in chapter 3.7. A schematic scheme of the centrifugal filtration is displayed in Figure 33.

Fractions obtained from filtration were analyzed with CE (described in chapter 2.4 and 3.8). Furthermore, freezing curves were recorded using the setup VODCA as described in chapter 2.1 and 3.4.

4.3.1. Single filtration

The electropherograms analyzed with CE of *3 kDa Filtrate I* and *3 kDa Retentate I* are pictured in Figure 53.

- 3 kDa

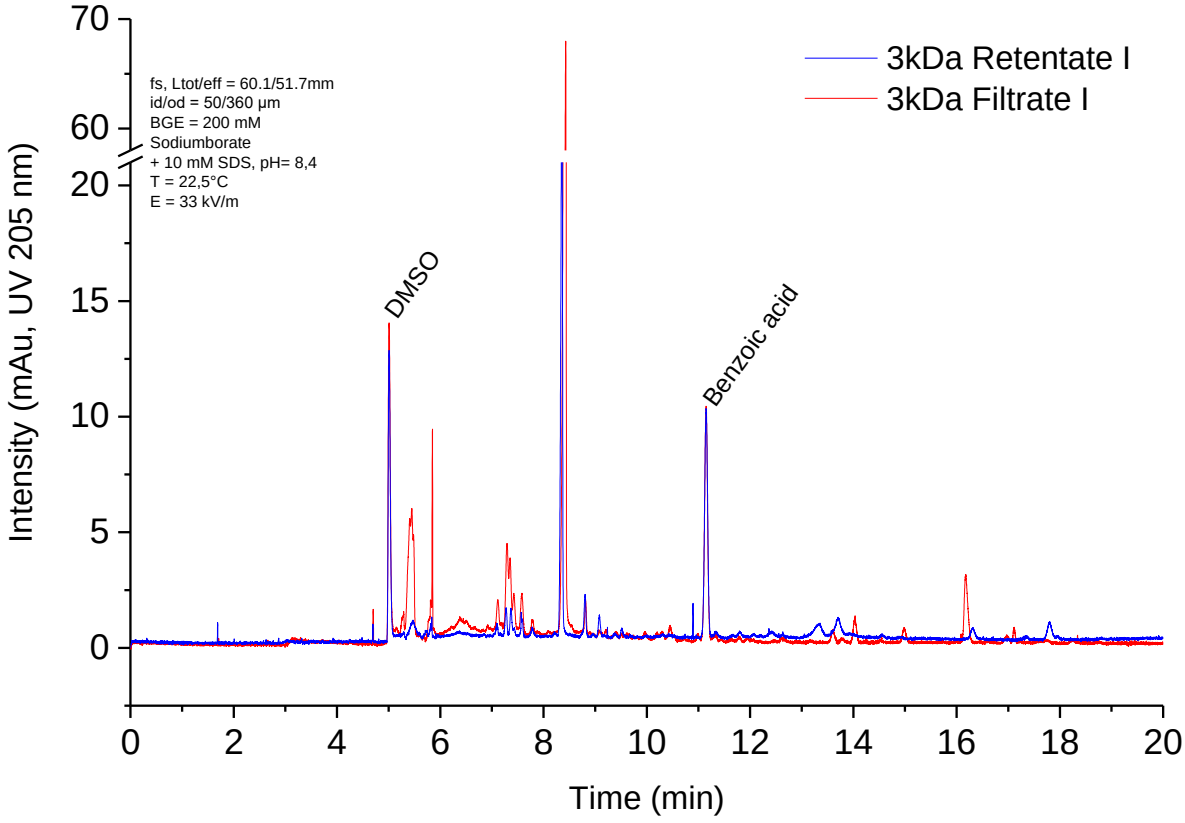

Figure 53: Electropherogram analyzed with CE of 3 kDa Filtrate I (red) and 3 kDa Retentate I (blue) obtained from centrifugal filtration.

Comparing the electropherograms of *3 kDa Retentate I* and *3 kDa Filtrate I*, peaks are more intense for *3 kDa Filtrate I* than for *3 kDa Retentate I*. However, at a migration time of 13,3 min and 17,8 min, peaks are just seen for *3 kDa Retentate I*, which are not visible for *3 kDa Filtrate I*. The freezing curves of *3 kDa Retentate I* and *3 kDa Filtrate I* are summarized in Figure 54.

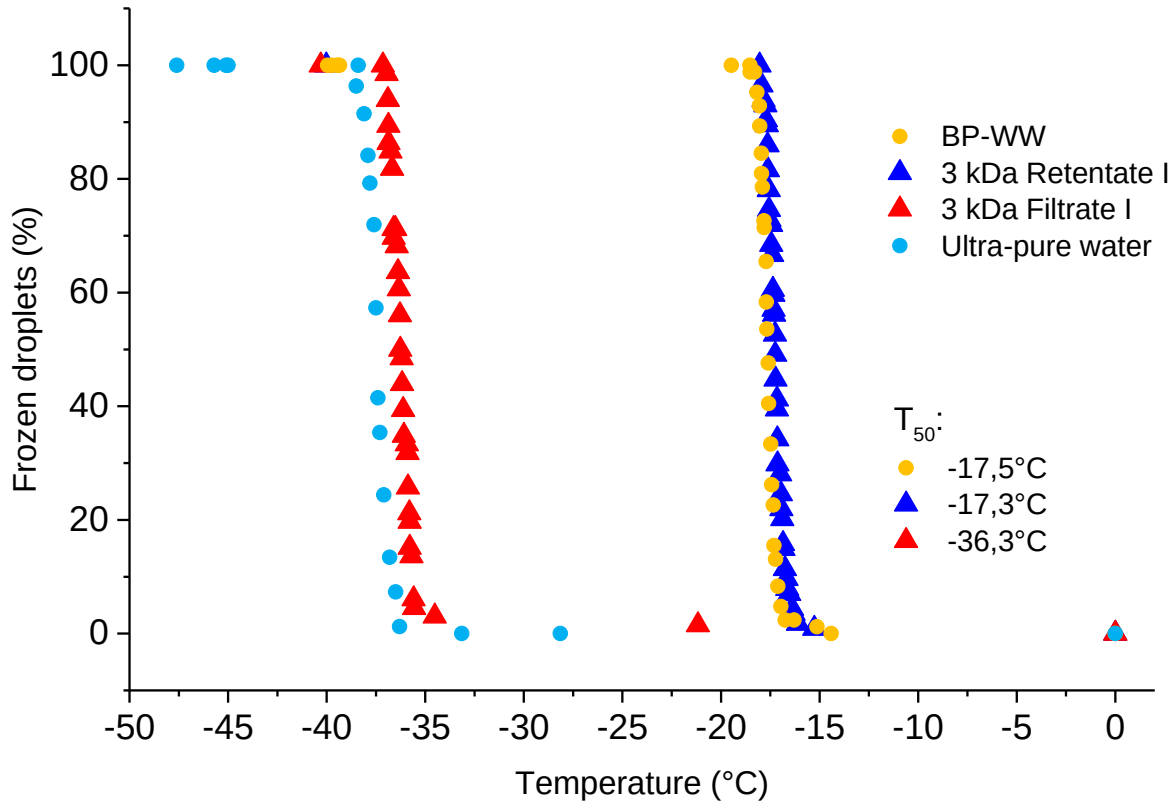

Figure 54: Freezing curves of 3 kDa Filtrate I (red) and 3 kDa Retentate I (blue) obtained from centrifugal filtration. Further, the freezing curves of ultra-pure water and BP-WW (both untreated) are used as references.

In Figure 54, freezing occurs homogeneously for *3 kDa Filtrate I* (red curve). This indicates that no IN are in *3 kDa Filtrate I*. However, the freezing curve of *3 kDa Retentate I* (blue) displays that freezing happens heterogeneously with the same onset temperature of freezing for BP-WW. In addition, *3 kDa Retentate I* has a median freezing temperature (T_{50}) of -17,3°C, which is comparable with BP-WW. Thus, IN are present in *3 kDa Retentate I.*

- 30 kDa

The electropherograms of *30 kDa Filtrate I* and *30 kDa Retentate I* are displayed in Figure 55.

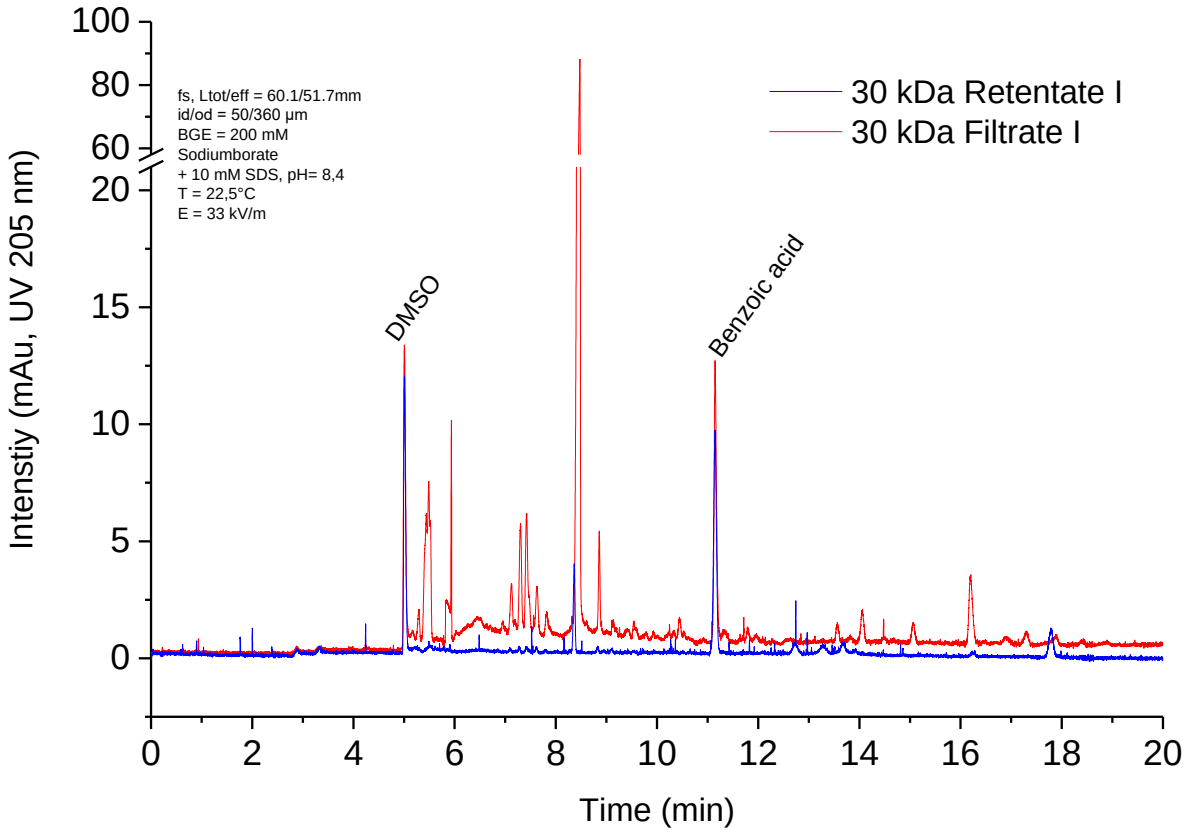

Figure 55: Electropherogram analyzed with CE from 30 kDa Filtrate I (red) and 30 kDa Retentate I (blue) obtained from centrifugal filtration.

Comparing *30 kDa Filtrate I* (red) and *30 kDa Retentate I* (blue), a difference in the signals appears clearly. The signals of *30 kDa Filtrate I* are appreciably higher. Some substances have been enriched in *30 kDa Filtrate I*. Peaks at 12,8, 13,3 and shortly before 18 min are just seen in *30 kDa Retentate I.* The freezing curves of *30 kDa Filtrate I* and *30 kDa Retentate I* are shown in Figure 56.

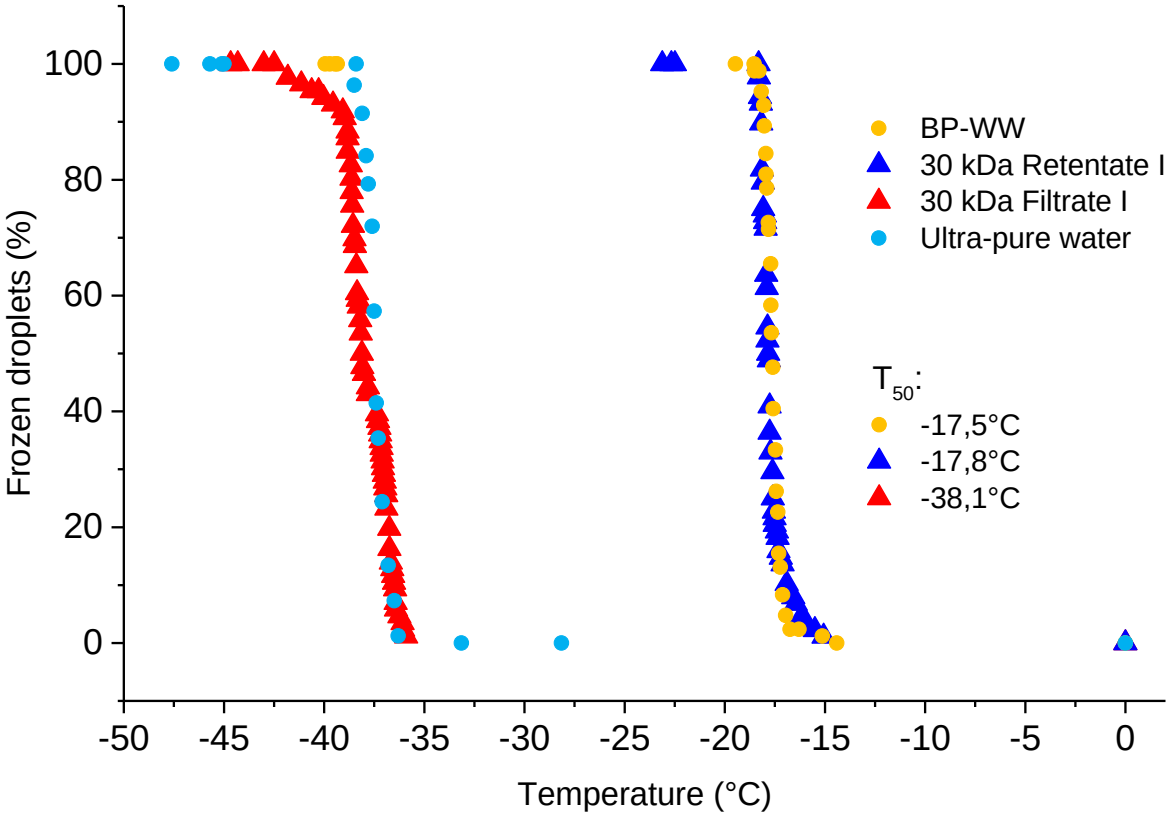

Figure 56: Freezing curves of 30 kDa Filtrate I (red) and 30 kDa Retentate I (blue) obtained from centrifugal filtration. Further, the freezing curves of ultra-pure water and BP-WW (both untreated) are used as references.

The freezing curves clearly show that *30 kDa Filtrate I* freezes homogeneously, whereas *30 kDa Retentate I* freezes heterogeneously. Similar to the freezing curves of the *3 kDa Filtrate I* and *3 kDa Retentate I* (see Figure 54). *30 kDa Retentate I* has a median freezing temperature of -17,8°C which is similar to BP-WW. Hence, *30 kDa Filtrate I* is not ice nucleation active, but *30 kDa Retentate I* is active. Thus, the IN is present in *30 kDa Retentate I.*

- 100 kDa

The electropherograms of *100 kDa Filtrate I* and *100 kDa Retentate I* are shown in Figure 57.

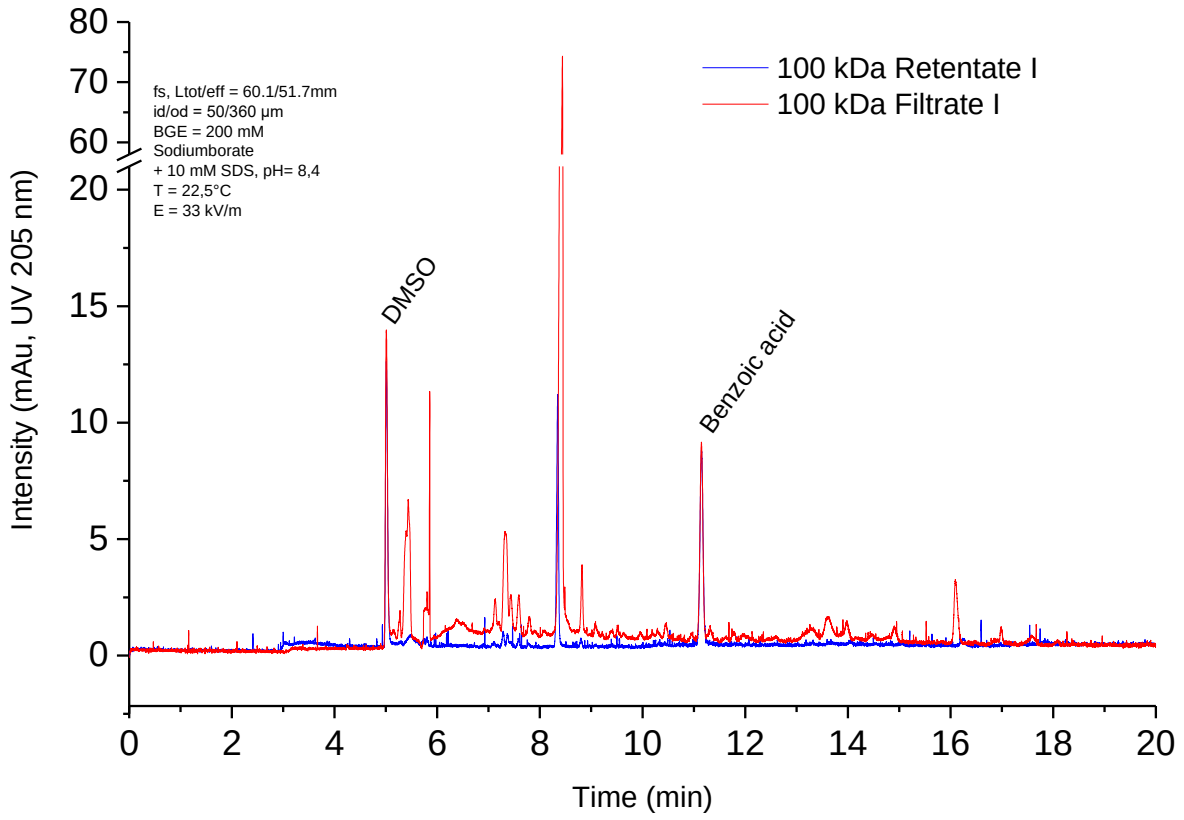

Figure 57: Electropherogram analyzed with CE from 100 kDa Filtrate I (red) and 100 kDa Retentate I (blue) obtained from centrifugal filtration.

Analog to the electropherograms of *30 kDa Filtrate I* and *30 kDa Retentate I* (see Figure 55), the electropherograms in Figure 57 show that the signals are more intense for *100 kDa Filtrate I*, compared to *100 kDa Retentate I*. Substances at migration times of 5,7 min, between 7 and 8 min and 8,4 min are seen in both fractions. Between 13 and 18 min different substances are enriched in the *100 kDa Filtrate I* fraction. The following freezing curves of both fractions, *100 kDa Filtrate I* and *100 kDa Retentate I* contain information about the freezing behavior (Figure 58).

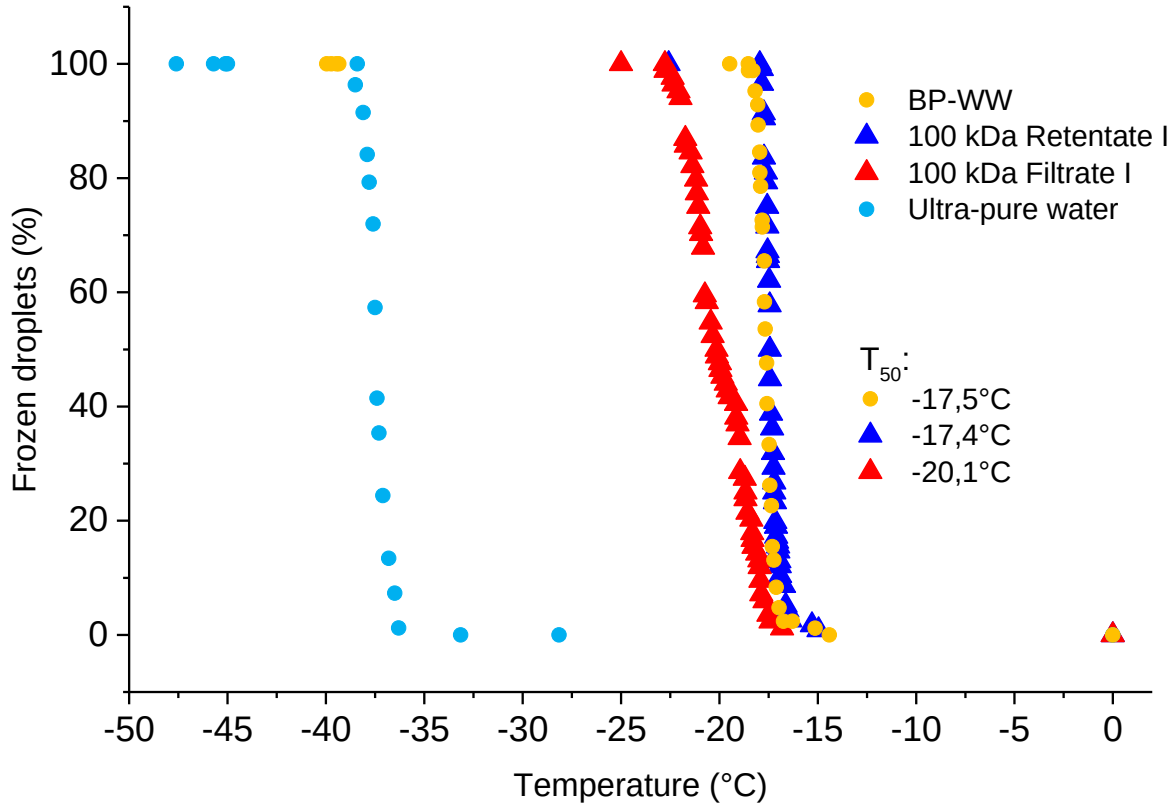

Figure 58: Freezing curves of 100 kDa Filtrate I (red) and 100 kDa Retentate I (blue) obtained from centrifugal filtration. Further, the freezing curves of ultra-pure water and BP-WW (both untreated) are used as references.

In contrast to the freezing curves shown before (Figure 54 and Figure 56), where *3 kDa- and 30 kDa Filtrate I* and *3 kDa- and 30 kDa Retentate I* were displayed, both *100 kDa Filtrate I* and *100 kDa Retentate I* are ice nucleation active. The onset temperature of freezing of *100 kDa Retentate I* is the same as for BP-WW. Furthermore, the T_{50} value for *100 kDa Retentate I* is -17,4°C. In addition, the curve progressions of *100 kDa Retentate I* and BP-WW are similar. Hence, *100 kDa Retentate I* is as ice nucleation active as BP-WW. For *100 kDa Filtrate I*, the onset temperature is a little bit lower compared to BP-WW. Further, the slope of the freezing curve is less steep for *100 kDa Filtrate I*. Additionally, the T_{50} is 2,6°C lower for *100 kDa Filtrate I* than for BP-WW. Hence, *100 kDa Filtrate I* is ice nucleation active, but not as active as BP-WW.

- 300 kDa

The electropherograms of *300 kDa Filtrate I* and *300 kDa Retentate I* are shown in Figure 59.

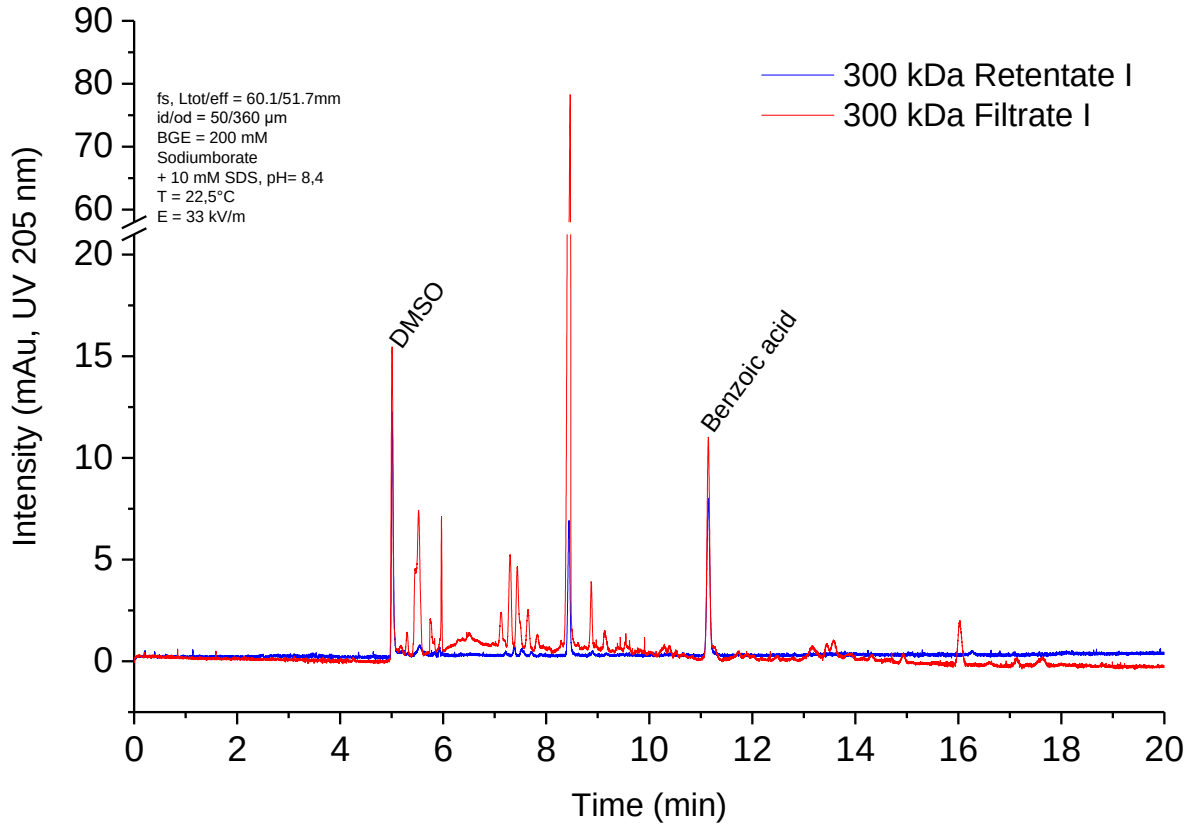

Figure 59: Electropherogram analyzed with CE from 300 kDa Filtrate I and 300 kDa Retentate I obtained from centrifugal filtration.

The electropherograms look similar to the ones in Figure 57. Many substances are enriched in *300 kDa Filtrate I*. Just a few signals (5,7 min, between 7 and 8 min) are present in both fractions. The freezing curves of *300 kDa Filtrate I* and *300 kDa Retentate I* (filter cut-off: 300 kDa) are shown in Figure 60.

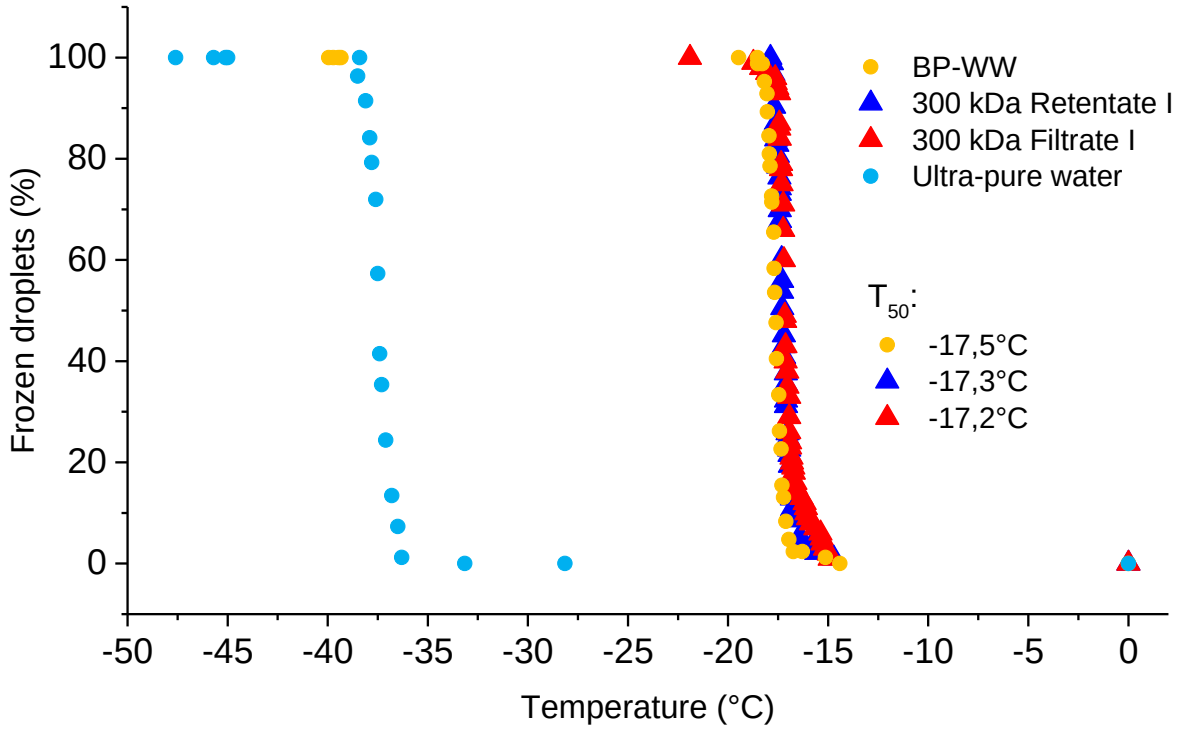

Figure 60: Freezing curves of 300 kDa Filtrate I (red) and 300 kDa Retentate I (blue) obtained from centrifugal filtration. Further, the freezing curves of ultra-pure water and BP-WW (both untreated) are used as references.

In the graph, both fractions, *300 kDa Retentate I* and *300 kDa Filtrate I*, are ice nucleation active. Freezing starts for both fractions at the same temperature as for BP-WW. The T_{50} value for *300 kDa Retentate I* is -17,3°C and for *300 kDa Filtrate I* -17,2°C. Moreover, the freezing curves of *300 kDa Retentate I* and *300 kDa Filtrate I* have the same curve progression as BP-WW. Thus, both fractions are ice nucleation active and IN are in both *300 kDa Retentate I* and *300 kDa Filtrate I.*

A summary of the T_{50} values for all fractions from single filtration are listed in Table 17.

Table 17: T_{50} values for 3-, 30-, 100- and 300 kDa Retentate I and Filtrate I. The active fractions are shown in bold.

Sample		T_{50} [°C]
3 kDa	*Retentate I*	***-17,3***
	Filtrate I	*-36,3*
30 kDa	*Retentate I*	***-17,8***
	Filtrate I	*-38,1*
100 kDa	*Retentate I*	***-17,4***
	Filtrate I	***-20,1***
300 kDa	*Retentate I*	***-17,3***
	Filtrate I	***-17,2***

Table 17 gives information about the ice nucleation activity of different fractions. *3- and 30-kDa Filtrate I* are the only fractions which are not active. The electropherograms of the ice nucleation active *3 kDa Retentate I* (Figure 53) *and 30 kDa Retentate I* (Figure 55) show peaks at a migration time of 13,3 min and 17,8 min, which are not visible for the none-active *3 kDa Filtrate I and 30 kDa Filtrate I*. In the active *100 kDa Filtrate I* (Figure 57) different substances are enriched between a migration time of 13 and 18 min. For the *300 kDa Retentate I* (Figure 59) no peaks are visible between 13 min and 18 min, but between 7 min and 8 min.

When using a filter with a 3 kDa or 30 kDa cut-off, a separation of IN from an inactive fraction could be achieved. For futher purification of IN containing fractions, repeated filtration of the retentates (washing steps with UHQ) was performed.

4.3.2. Repeated filtration (n=3)

3-, 30-, and 100 kDa *Retentate I* were filtrated three times. The procedure of the centrifugal filtration is described in chapter 3.7. A schematic scheme of the centrifugal filtration is displayed in Figure 33.

The remaining retentate and filtrate (denoted as *x kDa Retentate II* and *x kDa Filtrate II.3*) were analyzed on the one hand with CE as described in chapter 2.4 and 3.8. and on the other hand with the setup VODCA (chapter 2.1 and 3.4) to gather information about the freezing behavior.

- 3kDa

The electropherograms of *3 kDa Filtrate II.3* and *3 kDa Retentate II* are pictured in Figure 61.

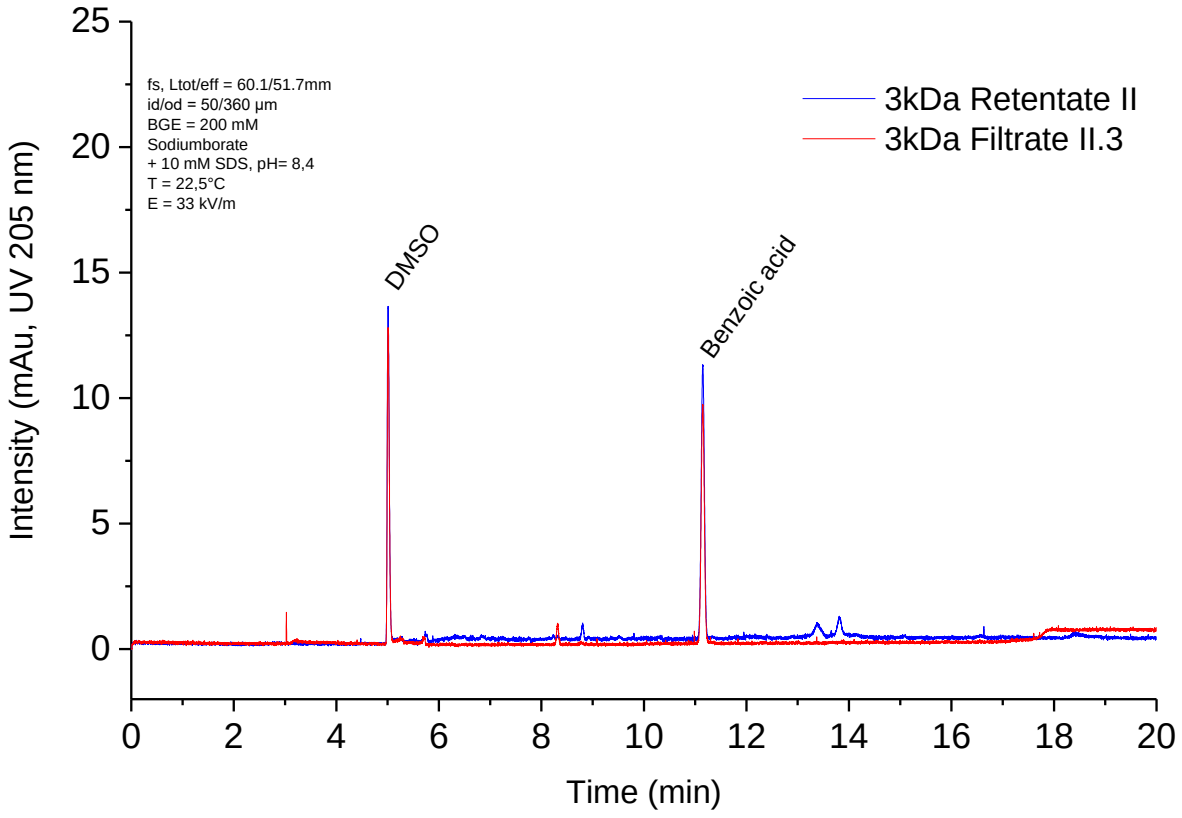

Figure 61: Electropherogram analyzed with CE of 3 kDa Filtrate II.3 (red) and 3 kDa Retentate II (blue) obtained from repeated centrifugal filtration of 3 kDa Retentate I (for a schematic illustration of the procedure see Figure 33).

Compared to the electropherograms of BP-WW, which was filtered once (see 4.3.1), not as many substances are visible in Figure 61. *3 kDa Filtrate II.3* shows a peak at a migration time of 8,4 min. In the electropherogram of *3 kDa Retentate II*, three peaks, one shortly before 9 min and two between 13 and 14 min, are visible. The freezing curves of *3 kDa Filtrate II.3* and *3 kDa Retentate II* are pictured in Figure 62.

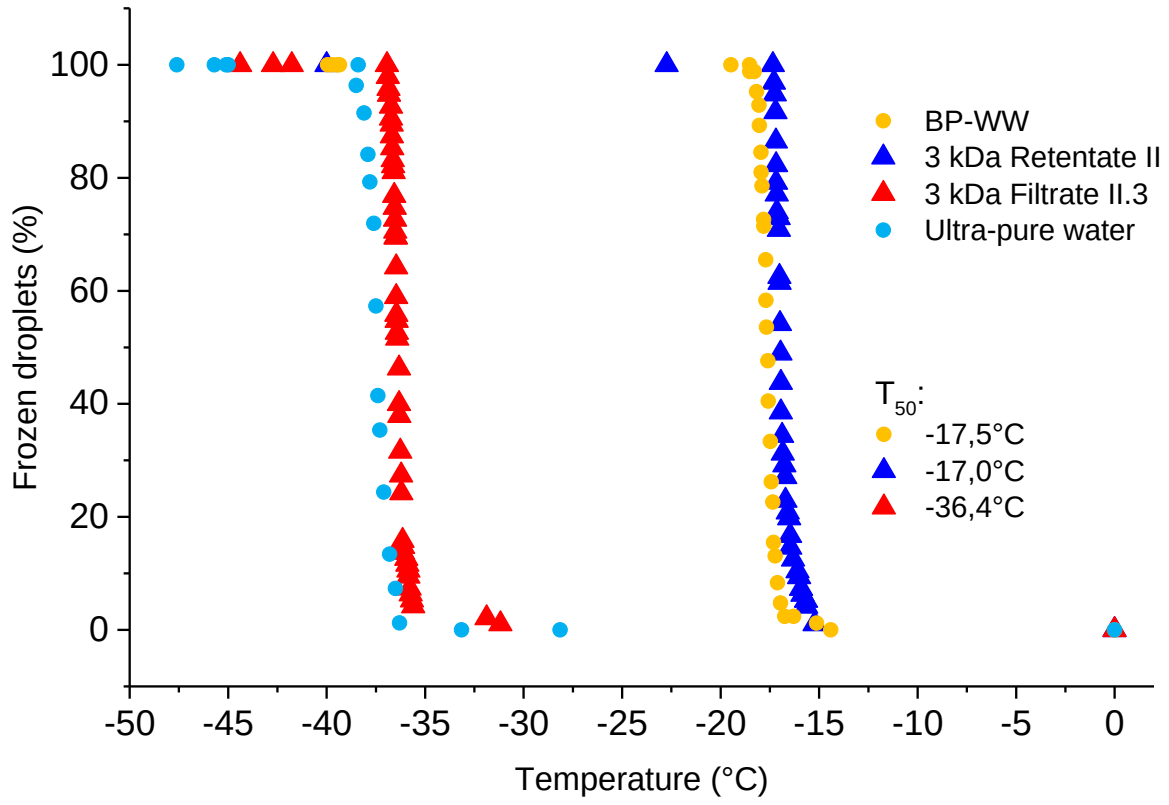

Figure 62: Freezing curves of 3 kDa Filtrate II.3 (red) and 3 kDa Retentate II (blue) obtained from repeated centrifugal filtration of 3 kDa Retentate I (for a schematic illustration of the procedure see Figure 33). The freezing curves of ultra-pure water and BP-WW (both untreated) are used as references.

In Figure 62, 3 *kDa Filtrate II.3* freezes homogeneously. In contrast, *3 kDa Retentate II* (T_{50}=-17,0°C) freezes heterogeneously, with the same onset temperature of freezing as BP-WW. Hence, *3 kDa Filtrate II.3* is not ice nucleation active. Thus, the substance, represented by the peak at 8,4 min migration time (see the electropherogram in Figure 61), does not seem to be an IN. When comparing the freezing behavior of *3 kDa Retentate II* and *3 kDa Filtrate II.3* to the *3 kDa Retentate I* and *3 kDa Filtrate I*, a similarity in their T_{50} value can be observed. Table 18 shows the T_{50} values for just mentioned fractions.

Table 18: T_{50} values for 3 kDa Retentate I, Filtrate I, Retentate II and Filtrate II.3.

Sample		*T_{50} [°C]*
3 kDa	*Retentate I*	***-17,3***
	Filtrate I	*-36,3*
	Retentate II	***-17,0***
	Filtrate II.3	*-36,4*

The electropherogram of *3 kDa Retentate I* (Figure 53) shows peaks at a migration time of 13,3 min and 17,8 min. For the *3 kDa Retentate II* (Figure 61) peaks at 9 min, 13,4 min and 13,8 min are visible. One peak is visible for *3 kDa Filtrate II.3* at a migration time of 8,4 min. This peak is also seen in the electropherogram of *3 kDa Filtrate I*, beside others. Furthermore, the signals for *3 kDa Retentate II* and *3 kDa Filtrate II.3* are less intense than for *3 kDa Retentate I* and *3 kDa Filtrate I*. Since repeated filtration includes washing steps, the concentration of the fractions decreases and a decrease in the signals is visible.

- 30 kDa

The electropherograms of *30 kDa Filtrate II.3* and *30 kDa Retentate II* are shown in Figure 63.

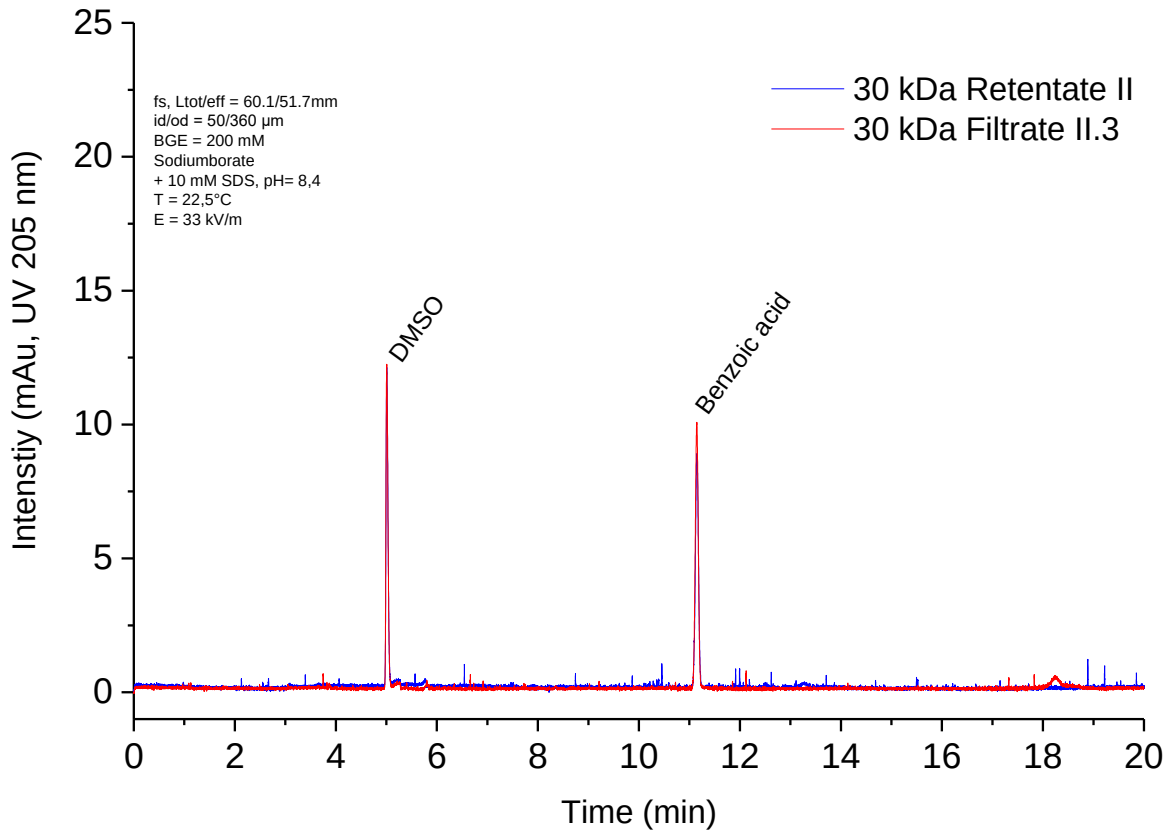

Figure 63: Electropherogram analyzed with CE of 30 kDa Filtrate II.3 (red) and 30 kDa Retentate II (blue) obtained from repeated centrifugal filtration of 30 kDa Retentate I (for a schematic illustration of the procedure see Figure 33).

Beside the EOF markers, no intense peaks are seen in the electropherogram of *30 kDa Filtrate II.3* and *30 kDa Retentate II*. Just one peak at 18,3 min is visible of *30 kDa Filtrate II.3*. The freezing curves of *30 kDa Filtrate II.3* and *30 kDa Retentate II* are displayed in Figure 64.

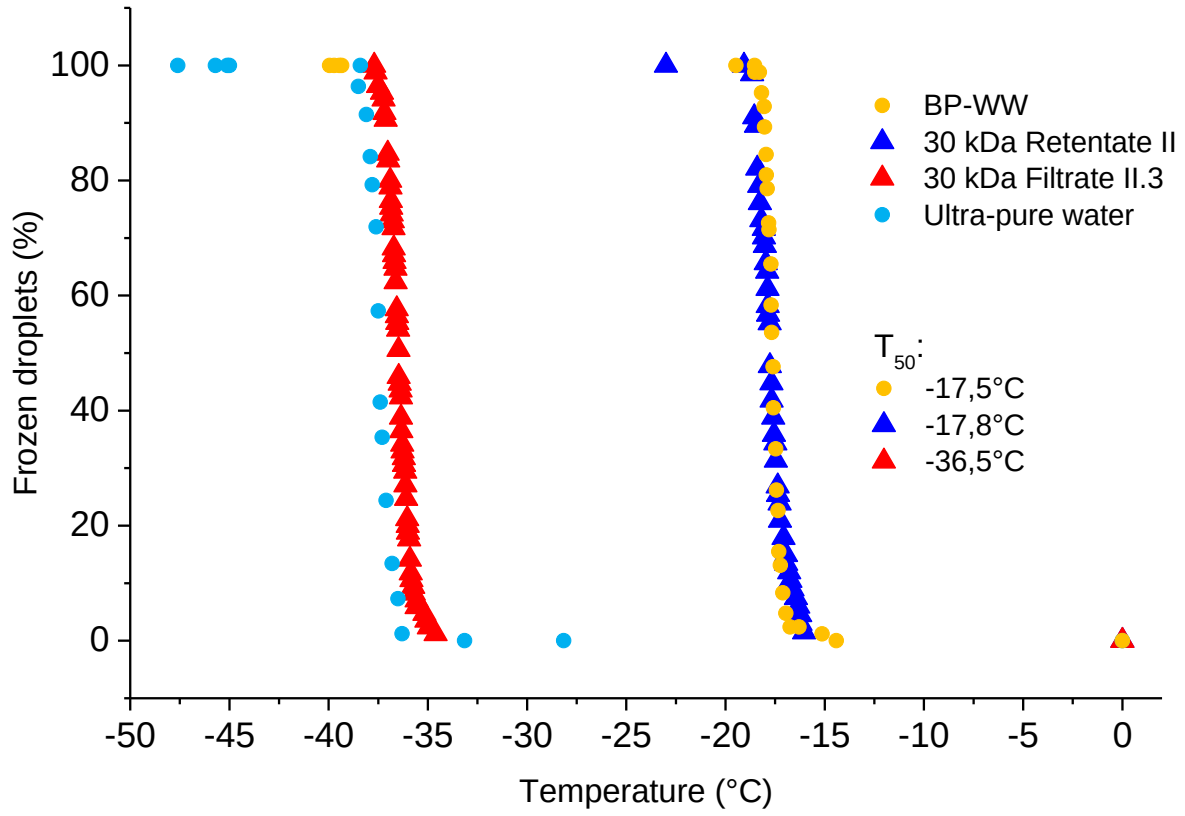

Figure 64: Freezing curves of 30 kDa Filtrate II.3 (red) and 30 kDa Retentate II (blue) obtained from repeated centrifugal filtration of 30 kDa Retentate I (for a schematic illustration of the procedure see Figure 33). The freezing curves of ultra-pure water and BP-WW (both untreated) are used as references.

It is clearly visible, that *30 kDa Filtrate II.3* freezes homogeneously and *30 kDa Retentate II* heterogeneously. *30 kDa Retentate II* has a T_{50} value of -17,8°C, which is comparable with BP-WW. Furthermore, the curve progression of *30 kDa Retentate II* and BP-WW are similar. Thus, *30 kDa Retentate II* is as ice nucleation active as BP-WW. When comparing the T_{50} values of *30 kDa Retentate II* and *30 kDa Filtrate II.3* to the ones for *30 kDa Retentate I* and *30 kDa Filtrate I*, a similarity is seen. Table 19 displays the T_{50} values for just mentioned fractions.

Table 19: T_{50} values for 30 kDa Retentate I, Filtrate I, Retentate II and Filtrate II.3.

Sample		T_{50} [°C]
30 kDa	*Retentate I*	***-17,8***
	Filtrate I	*-38,1*
	Retentate II	***-17,8***
	Filtrate II.3	*-36,5*

In Figure 63 the electropherogram of *30 kDa Filtrate II.3* displays a peak at 18,3 min. However, no peaks at this migration time are visible in *30 kDa Filtrate I* and *30 kDa Retentate I* (Figure 55).

- 100 kDa

The electropherograms of *100 kDa Filtrate II.3* and *100 kDa Retentate II* are pictured in Figure 65.

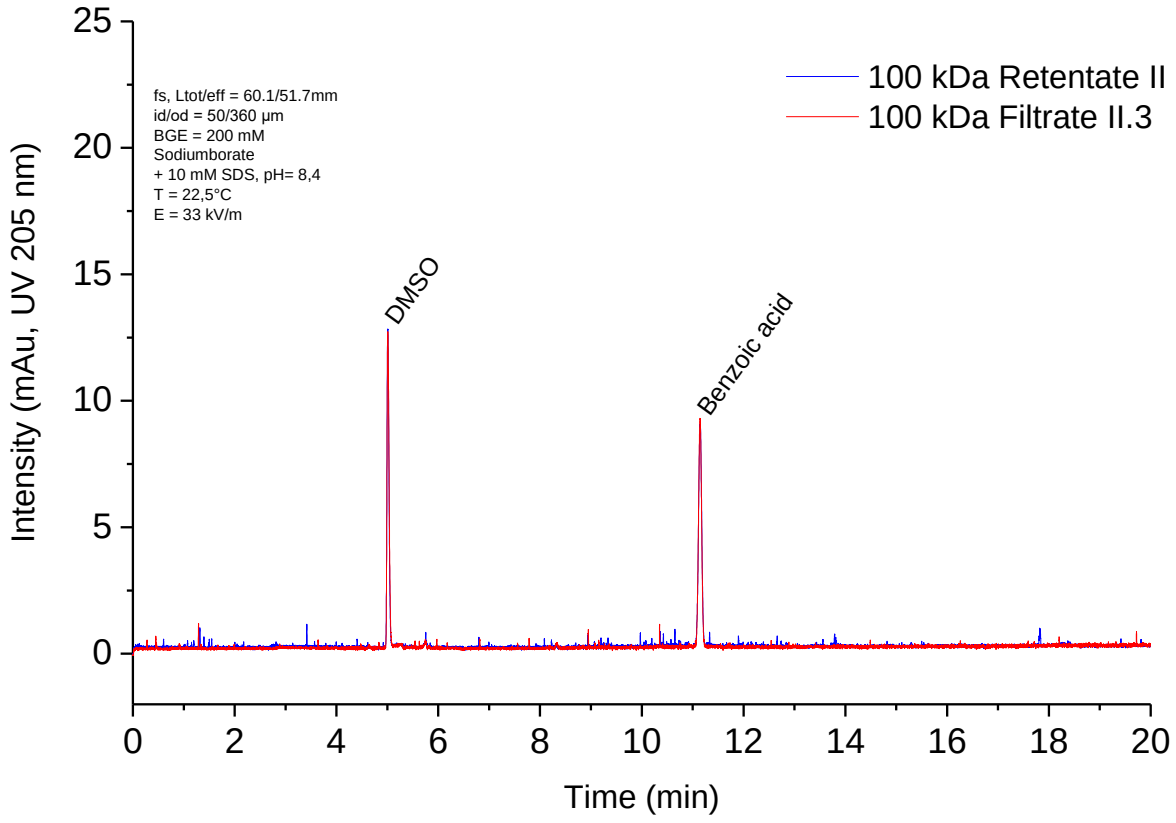

Figure 65: Electropherogram analyzed with CE of 100 kDa Filtrate II.3 (red) and 100 kDa Retentate II (blue) obtained from repeated centrifugal filtration of 100 kDa Retentate I (for a schematic illustration of the procedure see Figure 33).

In this picture, no signals except the EOF markers, are visible anymore. However, the freezing curves of *100 kDa Filtrate II.3* and *100 kDa Retentate II* show ice nucleation activity (see Figure 66).

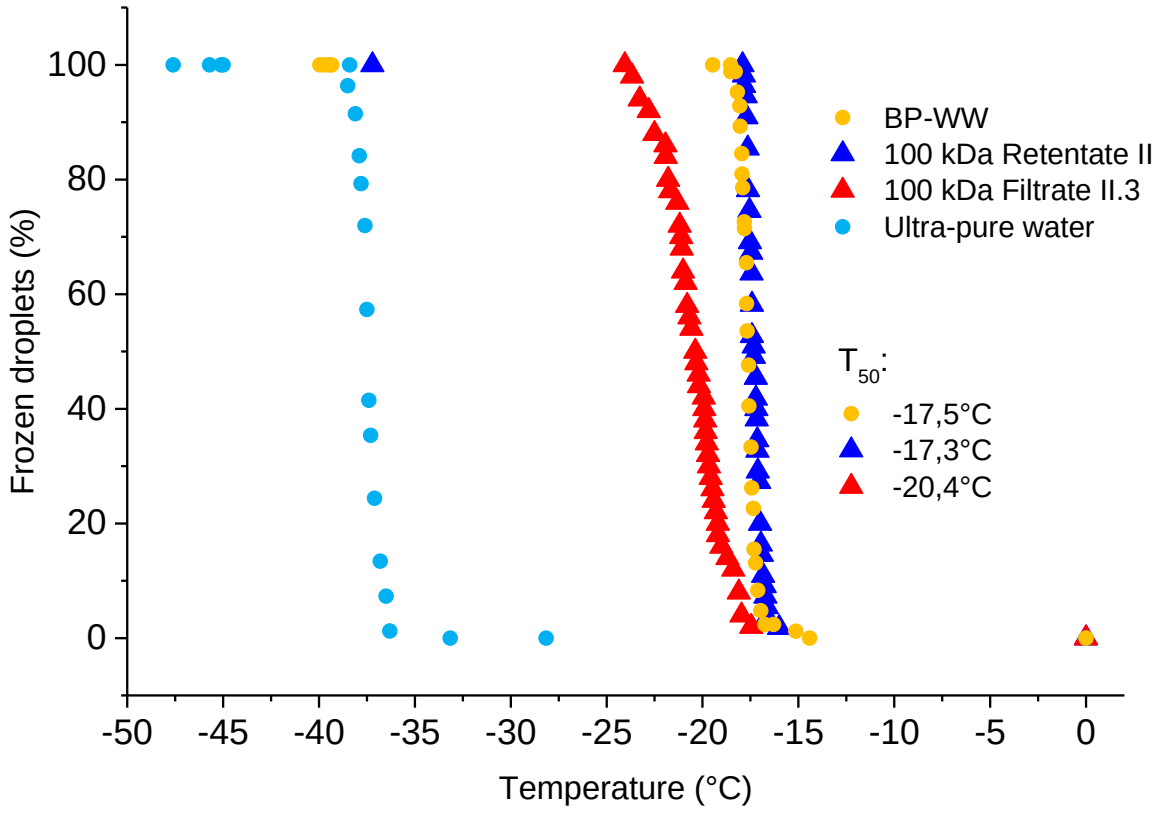

Figure 66: Freezing curves of 100 kDa Filtrate II.3 (red) and 100 kDa Retentate II (blue) obtained from repeated centrifugal filtration of 100 kDa Retentate I (for a schematic illustration of the procedure see Figure 33). The freezing curves of ultra-pure water and BP-WW (both untreated) are used as references.

In Figure 66 *100 kDa Retentate II* has the same curve progression as BP-WW. Moreover, the onset temperature of *100 kDa Retentate II* is slightly shifted compared to BP-WW. In addition, the T_{50} value for *100 kDa Retentate II* is -17,3°C. Thus, the fraction is ice nucleation active. The freezing curve of *100 kDa Filtrate II.3* is slightly flattened compared to BP-WW. Additionally, the T_{50} value for *100 kDa Filtrate II.3* is -20,4°C. Hence, *100 kDa Filtrate II.3* freezes heterogeneously but is not as ice nucleation active as BP-WW or *100 kDa Retentate II.* When comparing *100 kDa Retentate II* and *100 kDa Filtrate II.3* to the *100 kDa Retentate I* and *100 kDa Filtrate I*, they have nearly the same T_{50} value. Table 20 shows the T_{50} values for just mentioned fractions.

Table 20: T_{50} values for 100 kDa Retentate I, Filtrate I, Retentate II and Filtrate II.3.

Sample		T_{50} [°C]
100 kDa	*Retentate I*	***-17,4***
	Filtrate I	***-20,1***
	Retentate II	***-17,3***
	Filtrate II.3	***-20,4***

In contrast to the electropherogram of *100 kDa Retentate II* and *100 kDa Filtrate II.*3 (Figure 65), where no signals are visible, substances at migration times of 5,7 min, between 7 and 8 min and 8,4 min are seen for *100 kDa Retentate I* and *100 kDa Filtrate I* (Figure 57). Between 13 and 18 min, different substances are enriched in the *100 kDa Filtrate I* fraction.

4.3.3. Summary filtration experiment

Table 21 gives a summary of the ice nucleation activity of different fractions obtained from centrifugal filtration. Furthermore, the presence of the peak at a migration time of 8,4 min in the fractions is listed.

Table 21: Summary of filtration experiment, illustrating the T_{50} value of each fraction as well as the presence of the peak at 8,4 min migration time. The active fractions are shown in bold (n.a.: not analyzed).

Sample		T_{50} [°C]	Peak at 8,4 min
3 kDa	*Retentate I*	***-17,3***	yes
	Filtrate I	*-36,3*	yes
	Retentate II	***-17,0***	no
	Filtrate II.3	*-36,4*	yes
30 kDa	*Retentate I*	***-17,8***	yes
	Filtrate I	*-38,1*	yes
	Retentate II	***-17,8***	no
	Filtrate II.3	*-36,5*	no
100 kDa	*Retentate I*	***-17,4***	yes
	Filtrate I	***-20,1***	yes
	Retentate II	***-17,3***	no
	Filtrate II.3	***-20,4***	no
300 kDa	*Retentate I*	***-17,3***	yes
	Filtrate I	***-17,2***	yes
	Retentate II	n.a.	n.a.
	Filtrate II.3	n.a.	n.a.

The substance migrating at 8,4 min is seen in both, ice nucleation active and inactive fractions. When comparing the peaks at 8,4 min in the electropherograms (Figure 53) of the active *3 kDa Retentate I* and the inactive *3 kDa Filtrate I*, the intensity is higher for the inactive *3 kDa Filtrate I.* Thus, the concentration of the substance is higher in the inactive fraction. If this substance would be an IN, also the inactive *3 kDa Filtrate I* should be ice nucleation active. Since that is not the case, it is assumed that the substance migrating at 8,4 min is no IN. Furthermore, results from centrifugal filtration indicate that IN are larger than 30 kDa (± 10-

15%). In contrast to Pummer (2013) who showed that the size of IN is between 100 and 300 kDa. Table 22 displays the comparison between the single filtration parameters used in this thesis and in Pummer (2013).

Table 22: Comparison between single filtration parameters used in this thesis and in Pummer (2013).

	This thesis	Pummer (2013)
Filter	Pall Nanosep® centrifugal devices. Omega™ membrane: modified polyethersulfone on polyethylene substrate	Vivaspin® columns. Filter material: polyethersulfone
Centrifuge	Sigma 3-30K centrifuge	not stated
max. RCF	9000 *xg*	4000 *xg*
T [°C]	15	not stated

The difference in the results could be caused by the fact that different filters as well as different conditions for centrifugation were used.

When comparing the electropherograms of the fractions from single filtration with the fractions from repeated filtration, less signals with lower intensity are seen for the last mentioned. Repeated filtration was performed as a washing step to purify and enrich IN. The structure of IN from birch pollen grains is still not elucidated and IN could be e.g. aggregates which could change during the filtration process. The aggregation could decrease with increasing washing steps.

4.4. LC-ESI-MS/ MS^n

The flow through obtained from SPE (chapter 2.3 and 3.5) and filtrated samples (chapter 3.7.2) were analyzed with LC-ESI-MS. In addition, MS/MS and MS^3 were carried out for BP-WW.

4.4.1. LC-ESI-MS (Flow through)

The flow through obtained from SPE was analyzed with LC-ESI-MS with a focus on the substance at a retention time of 7,3 min for LC.

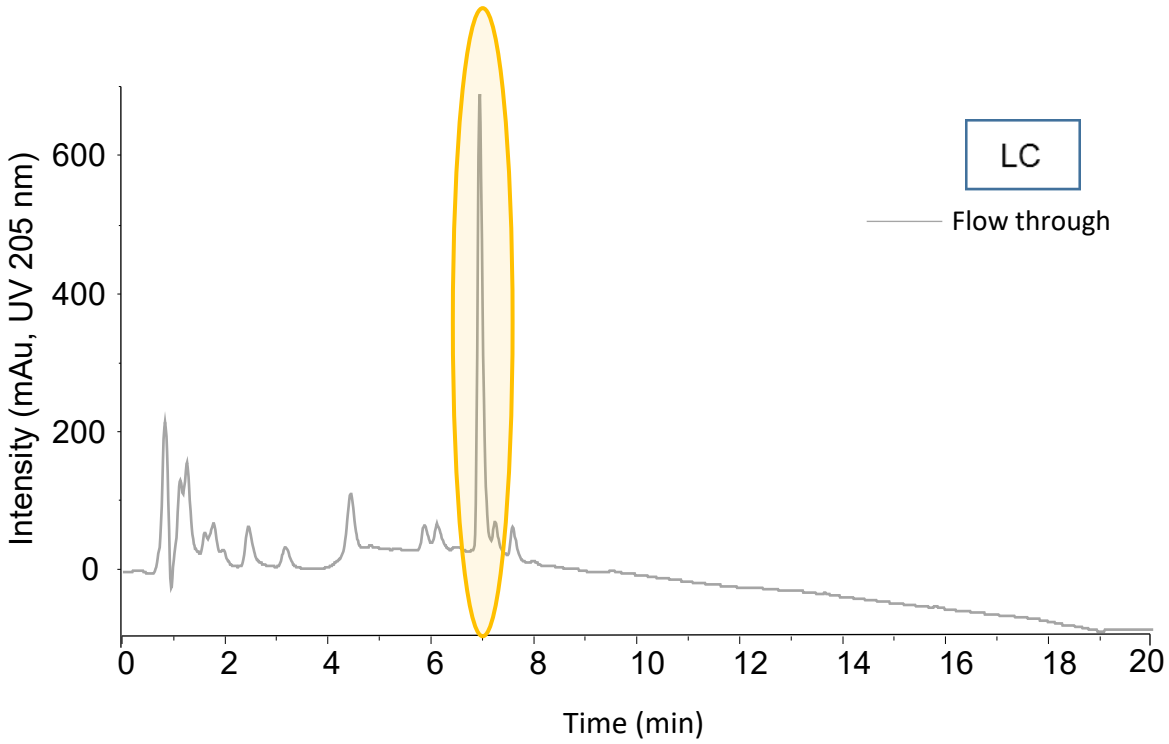

Figure 67: UV chromatogram of the flow through fraction (1:10 diluted with UHQ) obtained from SPE analyzed with LC

When comparing the UV signal obtained from LC (Figure 67) with the UV signal from CE (Figure 68) one peak is outstanding with its high intensity compared to all other detected signals. For the CE, it is the peak at 8,4 min migration time (which was mentioned already in chapter 4.3) and for LC the one at 7,3 min retention time. The peak of interest is highlighted yellow.

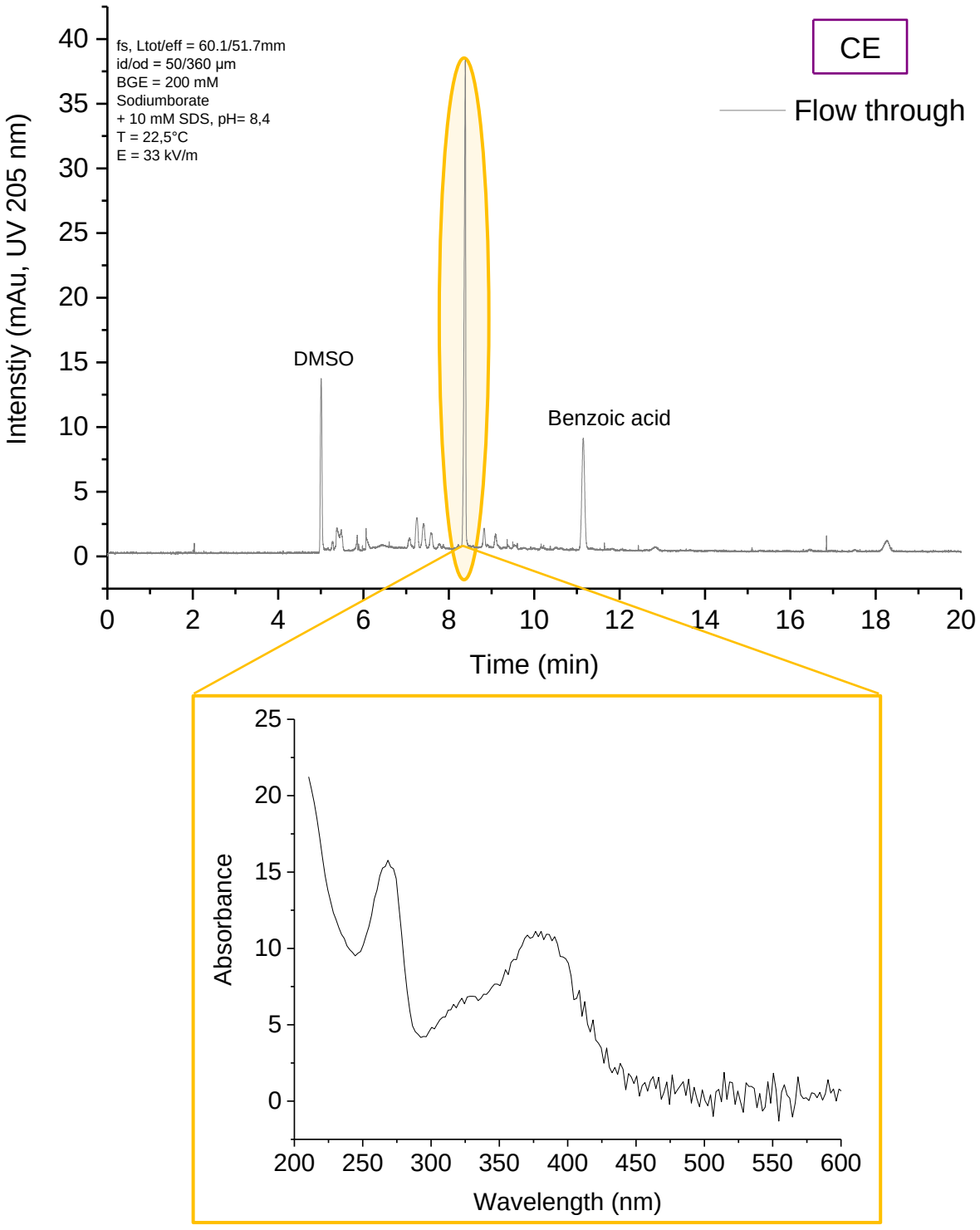

Figure 68: Electropherogram of the flow through (1:2,5 diluted) obtained from SPE, measured with CE. DMSO and benzoic acid are used as EOF markers. The graph on the bottom shows the UV/Vis spectrum for the substance migrating at 8,4 min.

The highlighted peak is around 10 times higher than the remaining peaks in both, the UV chromatogram (LC) and the electropherogram (CE). It is assumed that this peak represents the same substance. To be certain, the entire UV/Vis spectra of both the eluting substance at

7,3 min for LC and the substance migrating at 8,4 min for CE should be compared. However, within this thesis just for CE an entire UV/Vis spectrum for the substance migrating at 8,4 min was recorded but not for the substance eluting at 7,3 min for LC.

The base peak chromatogram (BPC) and the UV chromatogram (LC) from the flow through as well as the mass spectrum of the substance eluting at 7,3 min is shown in Figure 69.

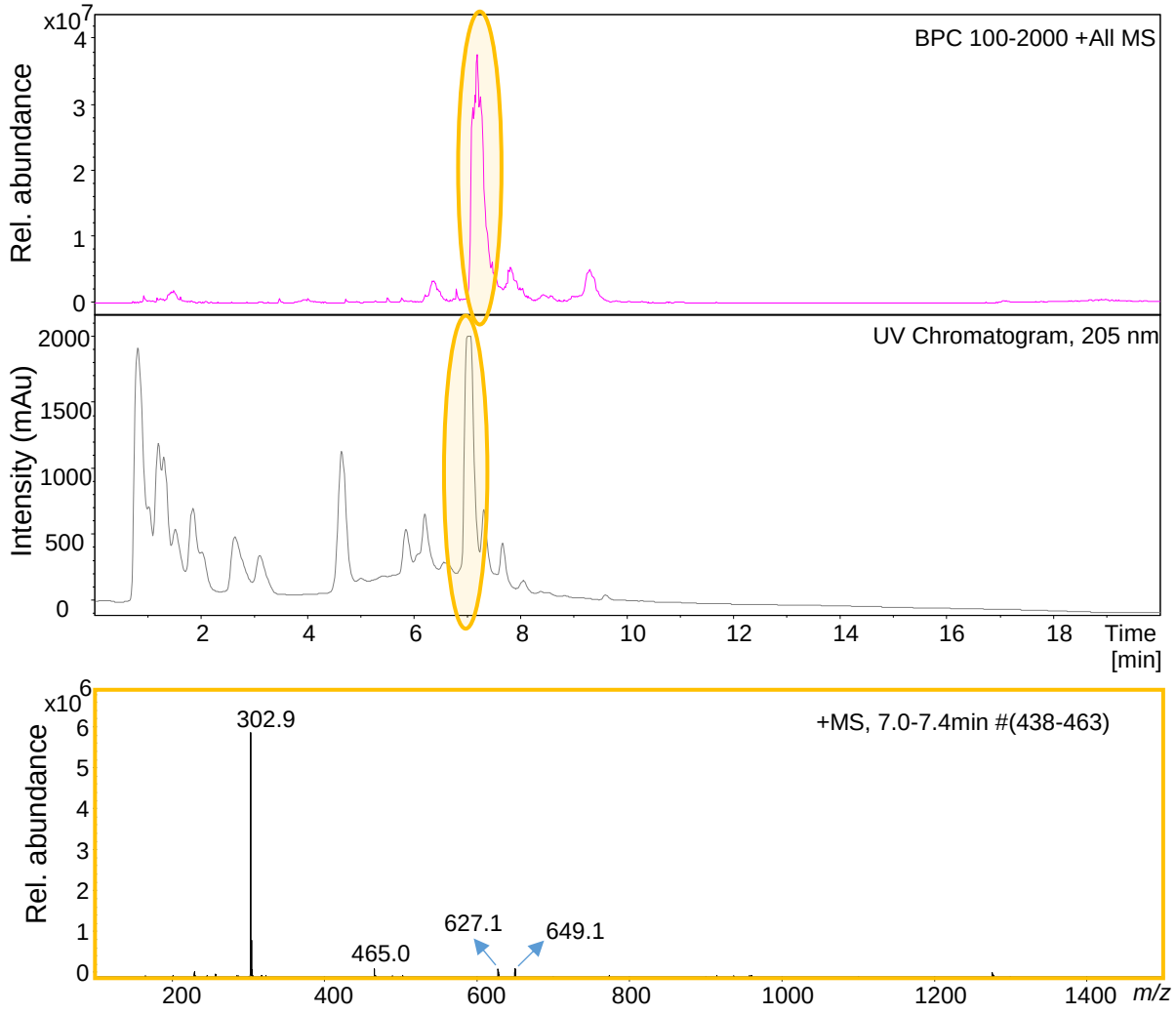

Figure 69: BPC and UV chromatogram recorded with LC of the flow through obtained from SPE as well as the mass spectrum (positive ion mode; method 1, see Table 12) of the substance eluting at 7,3 min. All m/z are singly charged.

The measurements were carried out in a positive ion mode. Method 1 (see Table 12) was used. When comparing the highlighted peaks, where it is assumed that they represent the same substance, the one in the BPC is slightly shifted to a higher retention time, compared to the UV chromatogram. The reason lies in the instrumental setup. The connection from the LC to the ESI-QIT is a few centimeters long. Hence, the sample is first analyzed in the LC and

afterwards in the ESI-QIT. Thus, the detection is not occurring simultaneously and a shift in the chromatograms is visible.

The mass spectrum above shows different $[M+H]^+$, whereas *m/z* 302,9 is dominating the spectrum with the highest relative abundance. Furthermore, *m/z* 627,1 and *m/z* 649,1 are also present. The flow through was further analyzed in a negative ion mode (Method 3, see Table 14).

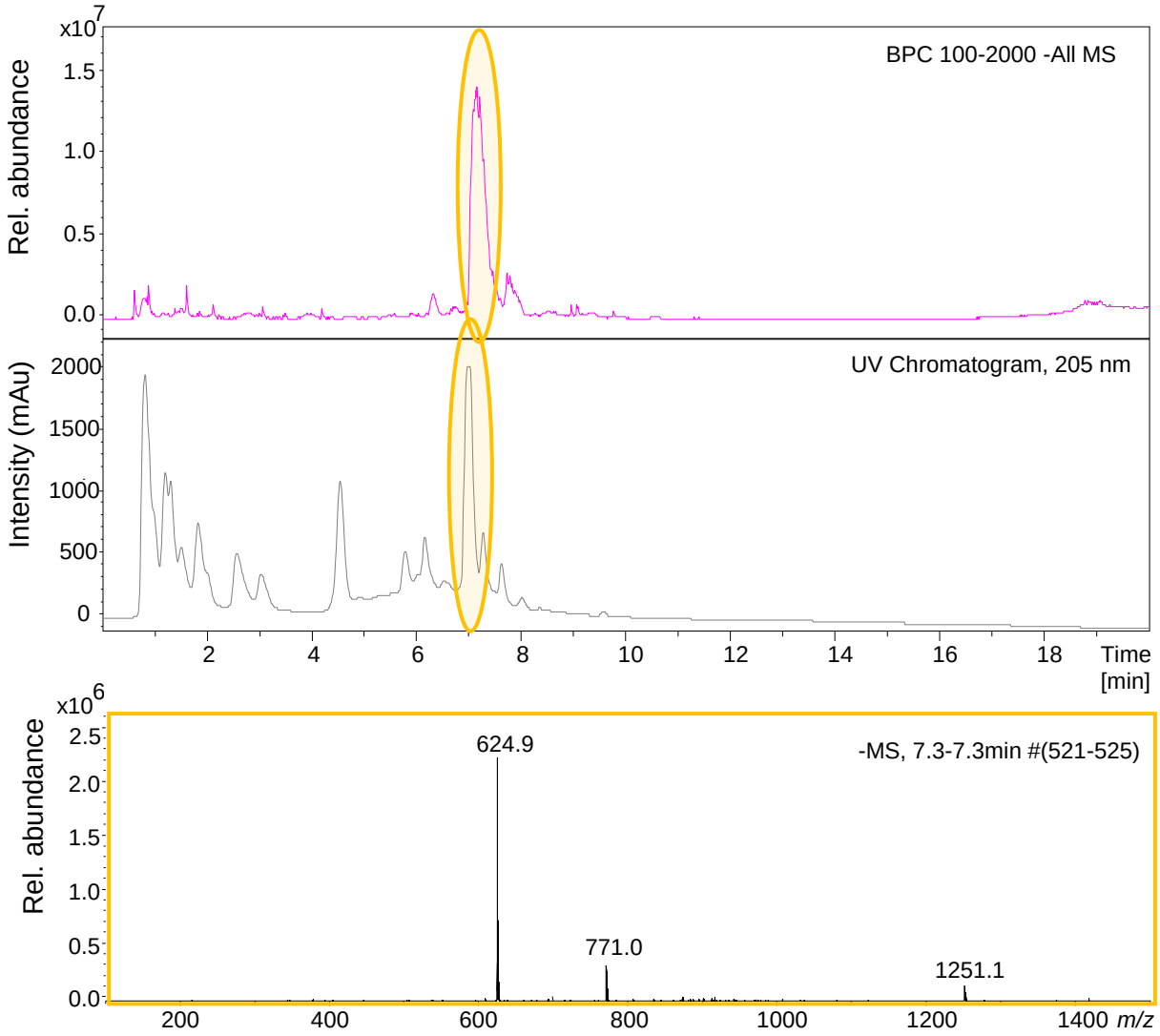

Figure 70: BPC and UV chromatogram recorded with LC of the flow through obtained from SPE as well as the mass spectrum (negative ion mode; method 3, see Table 14) of the substance eluting at 7,3 min. All m/z are singly charged.

As discussed before (Figure 69), a shift of the peaks is visible again. The mass spectrum shows different molecular ions ($[M-H]^-$). The *m/z* 624,9 has the highest relative abundance, followed by *m/z* 771,0 and *m/z* 1251,1. Results, using method 2 and 4 (see Table 13 and Table 15) are pictured in the Appendix (Figure 76 and Figure 77).

4.4.2. MS/MS and MS^3 (BP-WW)

To get more information about the substance, eluting at 7,3 min, MS/MS and MS^3 were carried out. However, for the structure elucidation experiments by collision induced dissociation not the flow through but BP-WW was used, because of higher concentration and continuous feeding of sample.

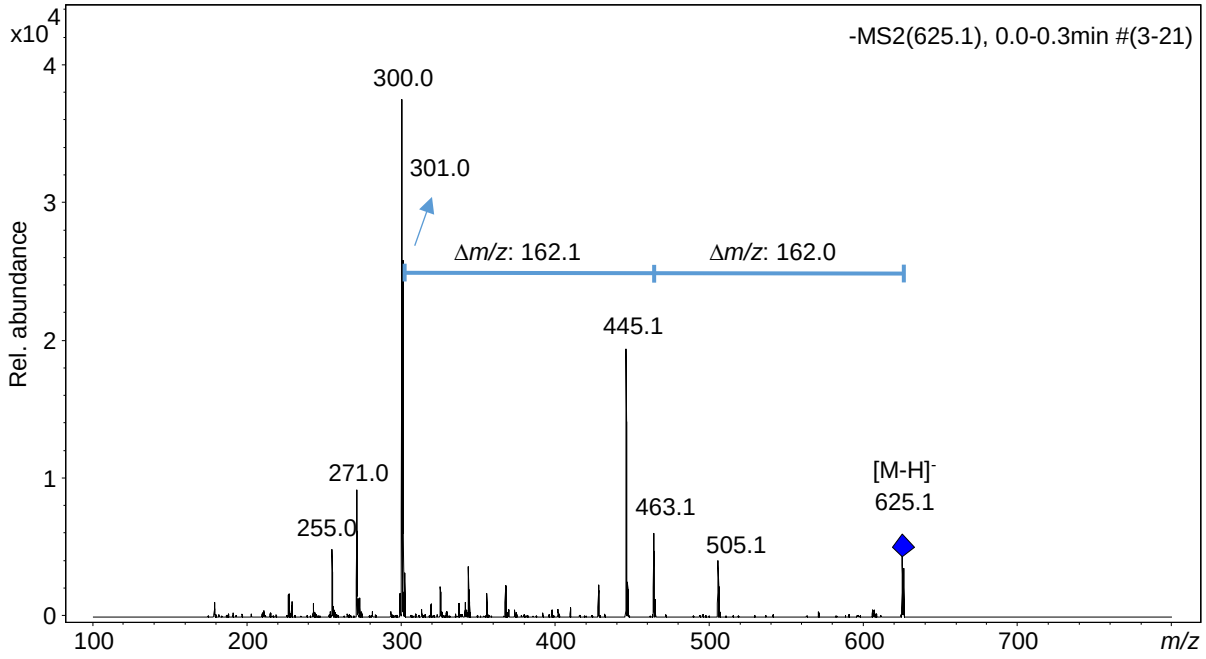

Figure 71: ESI-MS/MS spectrum of BP-WW (50 mg/ml).

The MS/MS spectrum of BP-WW (Figure 71) shows the fragmented precursor ion *m/z* 625,1 and its product ions. The mass difference between the precursor ion and *m/z* 463,1 is 162,0. This mass difference of *m/z* 162 indicates a loss of a hexose sugar moiety. Further, between *m/z* 463,1 and *m/z* 301,0 again a difference of *m/z* 162,1 is visible, indicating another hexose. In addition, MS^3 was carried out for m/z 301,0. Figure 72 displays the MS^3 spectrum.

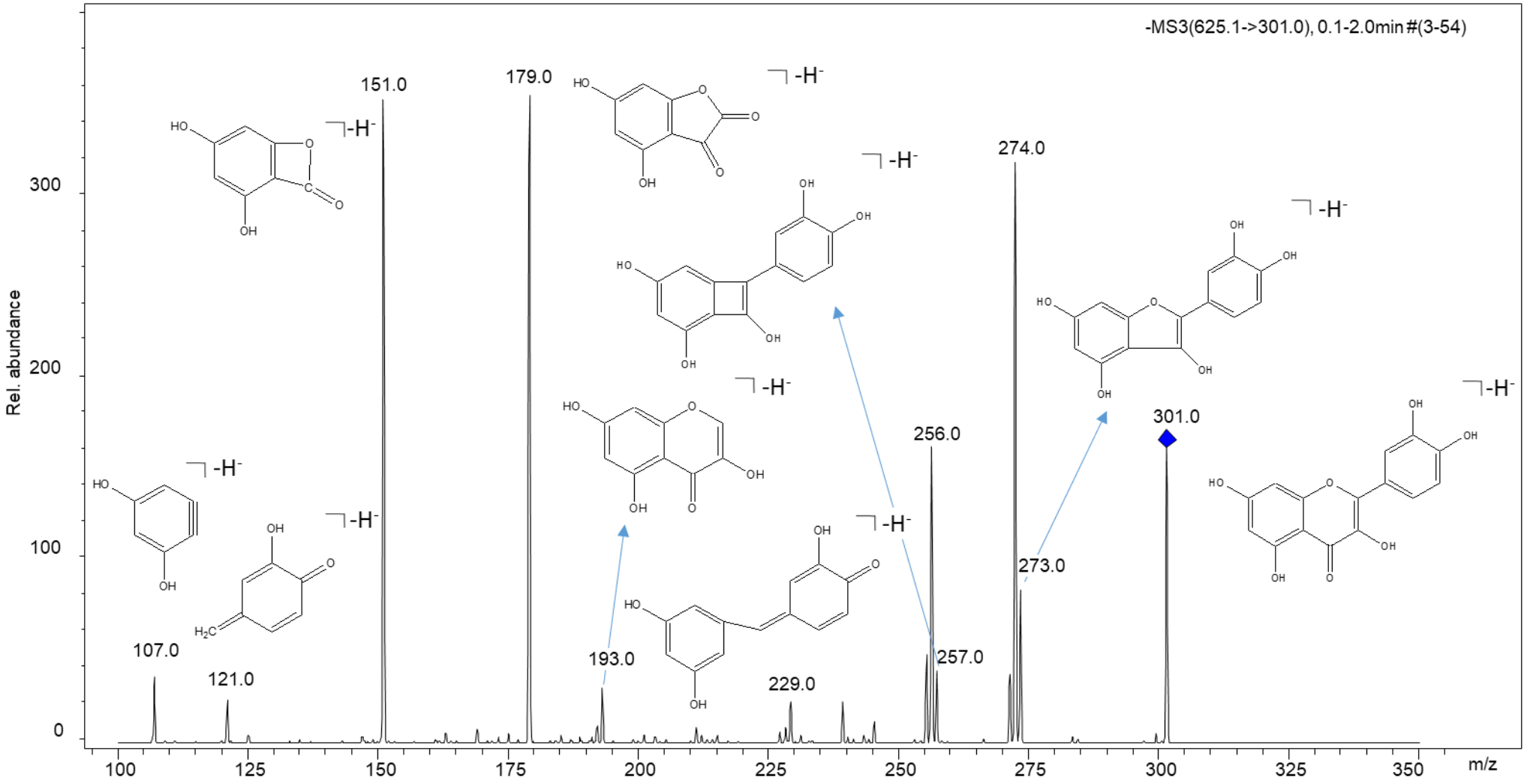

Figure 72: ESI-MS^3 spectrum of BP-WW (50 mg/ml) in a negative ion mode. The annotation of the structures of fragments is done with (Fabre et al., 2001).

The MS^3 spectrum obtained (Figure 72) was compared to data from literature. Fabre et al. (2001) determined flavonoids working with LC-ESI-MS/MS in a negative ion mode. When comparing the ESI-MS/MS spectrum of the flavanol quercetin (see Figure 73) in Fabre et al. (2001) with the MS^3 spectrum in Figure 70, fragmentation occurred similar.

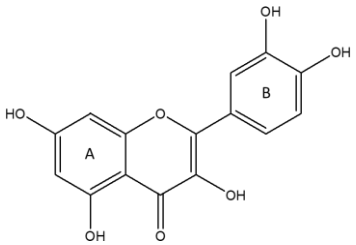

Figure 73: Chemical structure of quercetin.

The possible fragmentation pathways are shown in Figure 74.

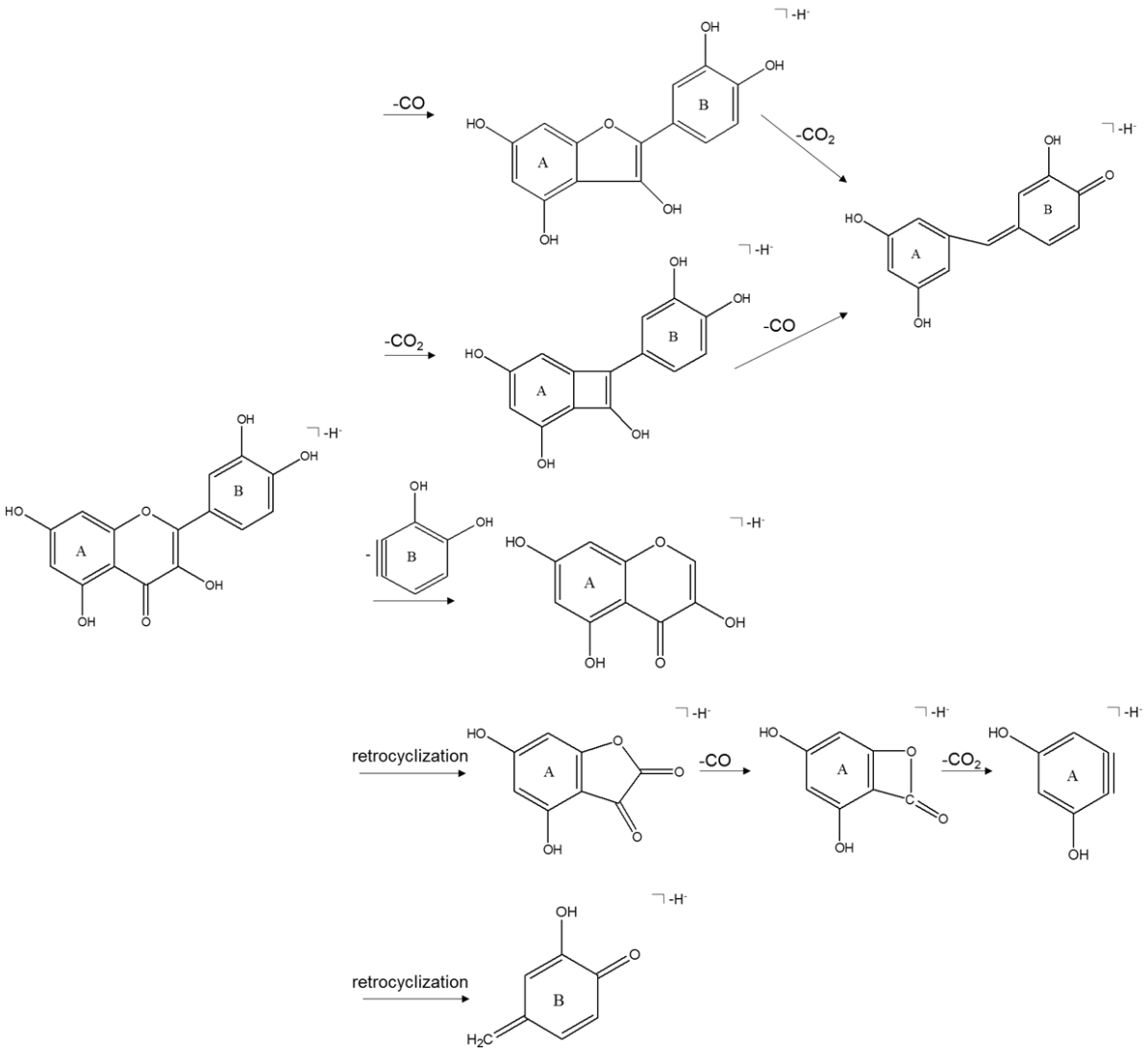

Figure 74: Proposed fragmentation from the pseudomolecular anion quercetin. (adapted from Fabre et al. (2001))

These results from LC-ESI-MS and Tandem-MS indicate that the substance eluting at 7,3 min is quercetin coupled with two hexoses. The presence of glycosylated flavonoids in birch pollen has already been reported in the literature e.g. Seutter Von Loetzen et al. (2014) showed that quercetin-3-O-sophoroside is a physiological ligand of Bet v1 in birch pollen, protecting the DNA from UV damage.

One major question that arises is if the glycosylated quercetin is an IN from birch pollen grains or not?

4.4.3. LC-ESI-MS (Filtration samples)

The ice nucleation active *3 kDa Retentate II* and the inactive *3 kDa Filtrate II.3* obtained from repeated centrifugal filtration were analyzed with LC-ESI-MS. Results are summarized in Figure 75.

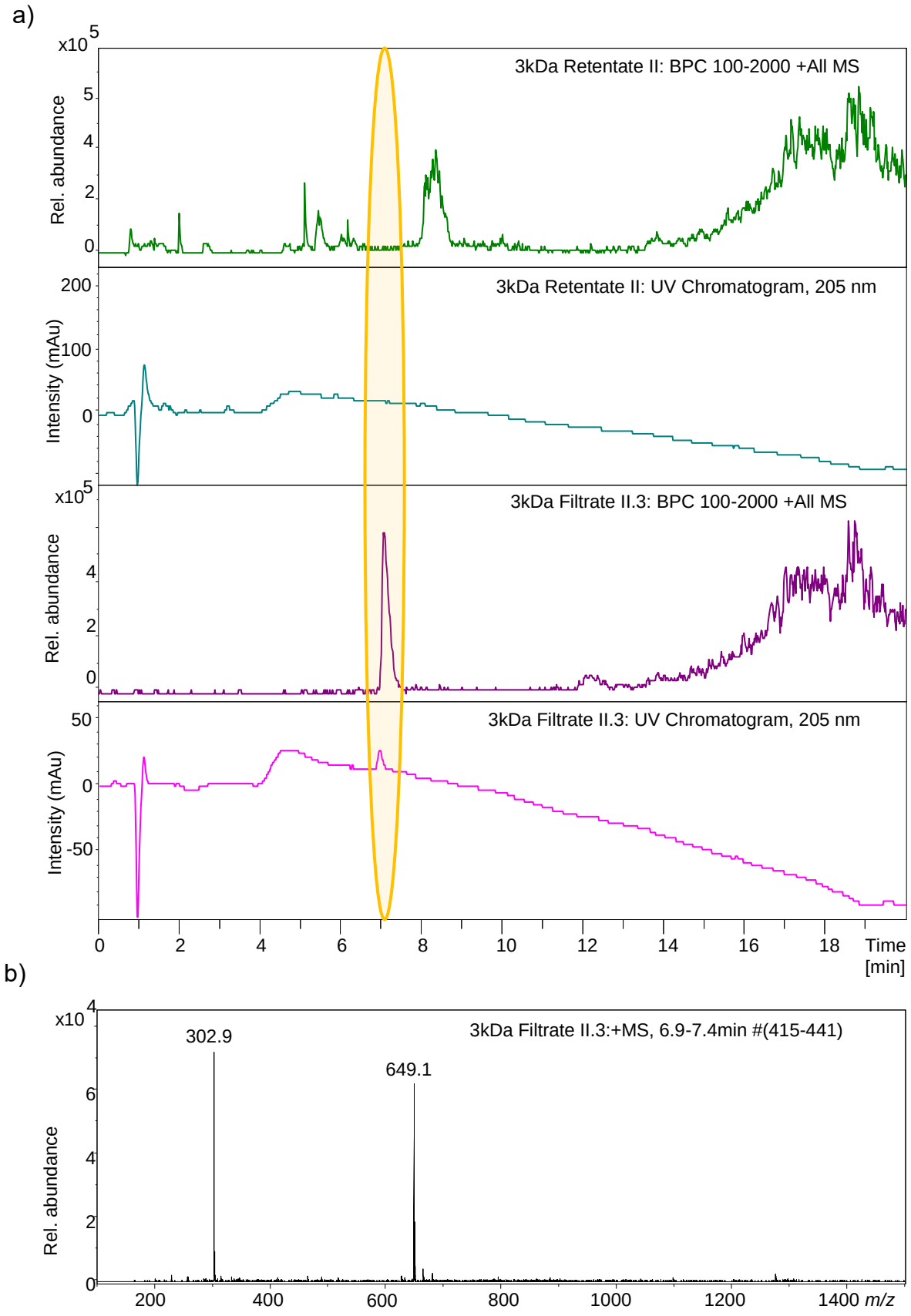

Figure 75: Results from filtrated BP-WW samples measured with LC-ESI-MS (method 1, see Table 12). a) BPC and UV chromatogram recorded with LC of 3 kDa Filtrate II.3 and 3 kDa Retentate II obtained from repeated centrifugal filtration, b) mass spectrum of 3 kDa Filtrate II.3 at a retention time between 6,9 and7,4 min.

As seen before in the UV chromatogram (LC) of the flow through (see Figure 69 and Figure 70), also for *3 kDa Filtrate II.3* a high signal in the UV chromatogram at a retention time between 6,9 and 7,4 min is visible. However, this substance is not present in *3 kDa Retentate II*.

In chapter 4.4.1 and 4.4.2, it is discussed that the glycosylated quercetin is represented by the peak at 7,3 min retention time for LC and 8,4 min migration time for CE. When comparing the UV chromatogram of *3 kDa Retentate II* and *3 kDa Filtrate II.3* (Figure 75) to the electropherograms recorded with CE (see Figure 61), just for *3 kDa Filtrate II.3* the peak at 8,4 min is visible. Thus, the glycosylated quercetin is represented by the peaks mentioned above. As seen in Figure 75, the substance is not present in *3 kDa Retentate II* but in *3 kDa Filtrate II.3*. The freezing curves of the *3 kDa Filtrate II.3* and *3 kDa Retentate II* (Figure 62) show that *3 kDa Filtrate II.3* is not ice nucleation active, but *3 kDa Retentate II* is. Since the flavone glycoside is present in the ice nucleation inactive *3 kDa Filtrate II.3* and not present in the active *3 kDa Retentate II*, we assume that this substance is no IN from birch pollen grains.

Beside *m/z* 302,9, *m/z* 649,1 (positive mode) and *m/z* 625,1 (negative mode) at a retention time of 7,3 min, many more *m/z* values at different retention times were observed. However, up until now only the one peak at 7,3 min was studied in detail.

5. Conclusion

The aim of this work was to characterize IN from *Betula pendula* birch pollen grains. The freezing curve of BP-WW showed that the T_{50} value is comparable with the one found in the literature (Pummer et al., 2012) indicating that freezing experiments were carried out properly. Results from SPE showed that all fractions obtained are ice nucleation active i.e. every fraction contains IN. For the elution, different concentrations of the polar MeOH as well as the non-polar n-hexane was used. Since IN interact with both the polar MeOH and the non-polar n-hexane, it is thought that IN may have amphiphilic properties. The measurements of the fractions obtained from SPE with CE illustrate that the UV signal of the flow through is higher than the one for BP-WW. The same is seen in the absorption spectra carried out with a photometer. The UV signal in the CE decreases with the fractions starting from the 20 vol% MeOH fraction to 100 vol% n-hexane fraction (fractions 2-5). Again, the same trend was seen for the absorption spectra recorded with the photometer. Thus, these results indicate that IN may not be UV active. However, it could be that the concentration of the IN, if UV active, is too low to be detected. The results from centrifugal filtration illustrate that IN are larger than 30 kDa. However, MWCO filters are not working strictly at 30 kDa but an uncertainty of 10-20 % has to be considered, depending on the physico-chemical properties of the analytes. Further, it can't be said for sure that IN are larger than 30 kDa since it has to be taken into consideration, that IN could interact with e.g. the filter material. Furthermore, IN could be e.g. aggregates which could change during the filtration process. The aggregation could decrease with increasing washing steps. The substance migrating in the CE at 8,4 min and eluting at 7,3 min for LC seems to be a dye of the birch pollen grain. LC-ESI-MS, MS/MS and MS^3 results point out that the natural pigment flavanol glycosylated quercetin is present in the birch pollen. However, ice nucleation experiments showed that the flavonoid is not the IN from *Betula* birch pollen grains.

In conclusion, many properties and characteristics of the IN from *Betula* birch pollen grains were found. However, the IN is still not elucidated and more research needs to be carried out.

6. Outlook

Reverse phase SPE of BP-WW showed that IN may have amphiphilic properties. However, since all fractions remained ice nucleation active, no purification of the IN was achieved. Dreischmeier et al. (2017) and Pummer et al. (2015) claimed that polysaccharides may play a crucial role for ice nucleation activity of BP-WW. Dreischmeier et al. (2017) specifies it to anionic polysaccharides. Therefore, it could be tested if purification of IN is achieved with anion exchange SPE.

ESI-MS/MS and ESI-MS^3 experiments indicated the presence of a flavanol coupled with two hexose sugars in BP-WW. According to our filtration experiments separation between the flavanol and the IN substance could be achieved. The IN substance remained on the filter. For future investigations, the supernatant containing IN could be used.

Furthermore, substances which frequently occur in pollen could be tested for ice nucleation activity. If active, it could be tried to purify the corresponding substance from BP-WW (if present).

7. References

Agranovski, I. 2010. *Aerosols: Science and Technology*, Wiley-VCH Verlag GmbH & Co. KGaA**,** 463.

Ahrens, C. D. 2007. *Meteorology Today: An Introduction to Weather, Climate, and the Environment*, Thomson Brooks/Cole.

Arrhenius, S. 1896. XXXI. On the influence of carbonic acid in the air upon the temperature of the ground. *Philosophical Magazine,* 41**,** 237-276.

Birdi, K. S. 2014. Colloidal Electrokinetic Processes. *Surface Chemistry Essentials.* CRC Press Taylor & Francis Group**,** 187-189.

Bousse, L., Mouradian, S., Minalla, A., Yee, H., Williams, K. & Dubrow, R. 2001. Protein Sizing on a Microchip. *Analytical Chemistry,* 73**,** 1207-1212.

Bowers, R. M., Mccubbin, I. B., Hallar, A. G. & Fierer, N. 2012. Seasonal variability in airborne bacterial communities at a high-elevation site. *Atmospheric Environment,* 50**,** 41-49.

Bruyn, V. D. 2012. *Cloud classification* [Online]. Available: https://commons.wikimedia.org/wiki/File:Cloud_types_en.svg [Accessed 06.08 2017].

Budzikiewicz, H. & Schäfer, M. 2012. Massenspektrometrie: Eine Einführung. *Sprayverfahren.* 6 ed. Weinheim, Germany: Wiley-VCH Verlag GmbH & Co. KGaA**,** 26-39.

D'amato, G., Liccardi, G. & Frenguelli, G. 2007. Thunderstorm-asthma and pollen allergy. *Allergy,* 62**,** 11-16.

Diehl, K., Matthias-Maser, S., Jaenicke, R. & Mitra, S. K. 2002. The ice nucleating ability of pollen: Part II. Laboratory studies in immersion and contact freezing modes. *Atmospheric Research,* 61**,** 125-133.

Diehl, K., Quick, C., Matthias-Maser, S., Mitra, S. K. & Jaenicke, R. 2001. The ice nucleating ability of pollen Part I : Laboratory studies in deposition and condensation freezing modes. *Atmospheric Research,* 58**,** 75-87.

Dole, M., Mack, L. L., Hines, R. L., Mobley, R. C., Ferguson, L. D. & Alice, M. B. 1968. Molecular Beams of Macroions. *The Journal of Chemical Physics,* 49**,** 2240-2249.

Dominguez, E., Mercado, J. A., Quesada, M. A. & Heredia, A. 1999. Pollen sporopollenin: degradation and structural elucidation. *Sexual Plant Reproduction,* 12**,** 171-178.

Dreischmeier, K., Budke, C., Wiehemeier, L., Kottke, T. & Koop, T. 2017. Boreal pollen contain ice-nucleating as well as ice-binding 'antifreeze' polysaccharides. *Science Report,* 7**,** 41890.

Fabre, N., Rustan, I., Hoffmann, E. & Quetin-Leclercq, J. 2001. Determination of flavone, flavonol, and flavanone aglycones by negative ion liquid chromatography electrospray

ion trap mass spectrometry. *Journal of the American Society for Mass Spectrometry,* 12**,** 707-715.

Fletcher, N. H. 1969. Active Sites and Ice Crystal Nucleation. *Journal of the Atmospheric Sciences,* 26**,** 1266-&.

Fourier, J. 1824. Remarques générales sur les températures du globe terrestre de des espace planétaires. *Annales de Chimie et de Physique,* 27**,** 136-167.

Gabler, R. E., Petersen, J. F. & Trapasso, L. M. 2007. *Essentials of Physical Geography, Eighth Edition,* Belmont, USA, Thomson Brooks/Cole**,** 658.

Gey, M. H. 2008a. Festphasenextraktion. *Instrumentelle Analytik und Bioanalytik.* 2 ed.: Springer-Verlag Berlin Heidelberg**,** 66-75.

Gey, M. H. 2008b. Molekülspektroskopie. *Instrumentelle Analytik und Bioanalytik.* 2 ed.: Springer-Verlag Berlin Heidelberg**,** 211-288.

Gey, M. H. 2008c. Theorie der Elektrophorese. *Instrumentelle Analytik und Bioanalytik.* 2 ed.: Springer-Verlag Berlin Heidelberg**,** 174-175.

Gutro, R. 2004. *NASA's ICESat Satellite Sees Changing World Affecting Many* [Online]. Available: https://www.nasa.gov/vision/earth/lookingatearth/icesat_light.html [Accessed 25.08. 2017].

Hiranuma, N., Möhler, O., Yamashita, K., Tajiri, T., Saito, A., Kiselev, A., Hoffmann, N., Hoose, C., Jantsch, E., Koop, T. & Murakami, M. 2015. Ice nucleation by cellulose and its potential contribution to ice formation in clouds. *Nature Geoscience,* 8**,** 273-277.

Hoffmann-Sommergruber, K., Vanek-Krebitz, M., Radauer, C., Wen, J., Ferreira, F., Scheiner, O. & Breiteneder, H. 1997. Genomic characterization of members of the Bet v 1 family: genes coding for allergens and pathogenesis-related proteins share intron positions. *Gene,* 197**,** 91-100.

Hoffmann, E. D. & Stroobant, V. 2007a. Electro-Optical Ion Detectors. *Mass Sepctrometry: Principles and Applications.* 3 ed. England: John Wiley & Sons Ltd**,** 181-182.

Hoffmann, E. D. & Stroobant, V. 2007b. Electrospray. *Mass Sepctrometry: Principles and Applications.* 3 ed. England: John Wiley & Sons Ltd**,** 43-55.

Hoffmann, E. D. & Stroobant, V. 2007c. Ion Trap Analyzer. *Mass Sepctrometry: Principles and Applications.* 3 ed. England: John Wiley & Sons Ltd**,** 100-122.

Huffman, J. A., Prenni, A. J., Demott, P. J., Pöhlker, C., Mason, R. H., Robinson, N. H., Fröhlich-Nowoisky, J., Tobo, Y., Després, V. R., Garcia, E., Gochis, D. J., Harris, E., Müller-Germann, I., Ruzene, C., Schmer, B., Sinha, B., Day, D. A., Andreae, M. O., Jimenez, J. L., Gallagher, M., Kreidenweis, S. M., Bertram, A. K. & Pöschl, U. 2013. High concentrations of biological aerosol particles and ice nuclei during and after rain. *Atmospheric Chemistry and Physics,* 13**,** 6151-6164.

Ipcc, Stocker, T. F., Qin, D., Plattner, G.-K., Tignor, M. M. B., Allen, S. K., Boschung, J., Nauels, A., Xia, Y., Bex, V. & Midgley, P. M. 2013. IPCC, 2013: Climate Change 2013: The Physical Science Basis. Contribution of Working Group I to the Fith Assessment Report of the Intergovernmental Panel on Climate Change. United Kingdom and New York, NY, USA**,** 1535.

Ipcc, Team, C. W., Pachauri, R. K. & Reisinger, A. E. 2007. Climate Change 2007: Synthesis Report. Contribution of Working Groups I, II and III to the Fourth Assessment Report of the Intergovernmental Panel on Climate Change. Geneva, Switzerland**,** 104.

Ipsen, H. & Lowenstein, H. 1983. Isolation and immunochemical characterization of the major allergen of birch pollen (Betula verrucosa). *Journal of Allergy and Clinical Immunology,* 72**,** 150-159.

Iribarne, J. V. & Thomson, B. A. 1976. On the evaporation of small ions from charged droplets. *The Journal of Chemical Physics,* 64**,** 2287-2294.

Kajava, A. V. & Lindow, S. E. 1993. A model of the three-dimensional structure of ice nucleation proteins. *J Mol Biol,* 232**,** 709-717.

Keeling, C. D. 1958. The concentration and isotopic abundances of atmospheric carbon dioxide in rural areas. *Geochimica et Cosmochimica Acta,* 13**,** 322-334.

Kicinski, H.-G. 1996. Festphasenextraktion zur Probenvorbereitung und Clean up. *CLB-Chemie in Labor und Biotechnik,* 47**,** 542-547.

Kiehl, J. T. & Trenberth, K. E. 1997. Earth's annual global mean energy budget. *Bulletin of the American Meteorological Society,* 78**,** 197-208.

Kishawi, I. 2008. *2100 Bioanalyzer* [Online]. Agilent Technologies. Available: https://www.agilent.com/cs/library/posters/Public/BioAnalyzer.PDF [Accessed 18.09. 2017].

Kiss, A. A. & Infante Ferreira, C. A. 2016. *Heat Pumps in Chemical Process Industry,* New York, USA, Taylor & Francis Inc.

Lehmann, T. 2009. *UV/VIS-Spektroskopie* [Online]. Freie Universität Berlin. Available: http://www.bcp.fu-berlin.de/chemie/chemie/studium/ocpraktikum/_Unterlagen_Spektroskopie/uv.pdf [Accessed 16.09. 2017].

Lohmann, U., Lüönd, F. & Mahrt, F. 2016a. *An Introduction of Clouds: From the Microscale to Climate*, Cambridge University Press.

Lohmann, U., Lüönd, F. & Mahrt, F. 2016b. Microphysical processes in cold clouds. *An Introduction of Clouds: From the Microscale to Climate.* Cambridge University Press**,** 218-250.

Lottspeich, F. & Engels, J. W. 2012a. Electrospray-Ionisation (ESI). *Bioanalytik.* 3 ed.: Springer-Verlag Berlin Heidelberg**,** 373-380.

Lottspeich, F. & Engels, J. W. 2012b. Elektrophoretische Verfahren. *Bioanalytik.* Springer-Verlag Berlin Heidelberg**,** 217-252.

Lottspeich, F. & Engels, J. W. 2012c. Kapillarelektrophorese. *Bioanalytik.* 3 ed.: Springer-Verlag Berlin Heidelberg**,** 253-284.

Lottspeich, F. & Engels, J. W. 2012d. Massenspektrometrie. *Bioanalytik.* 3 ed.: Springer-Verlag Berlin Heidelberg**,** 323-368.

Lottspeich, F. & Engels, J. W. 2012e. Spektroskopie. *Bioanalytik.* Springer-Verlag Berlin Heidelberg**,** 151-198.

Maki, L. R., Galyan, E. L., Chang-Chien, M.-M. & Caldwell, D. R. 1974. Ice nucleation induced by Pseudomonas syringae. *Applied Microbiology,* 28**,** 456-459.

March, R. E. 1997. An Introduction to Quadrupole Ion Trap Mass Spectrometry. *Journal of Mass Spectrometry,* 32**,** 351-369.

Marcolli, C. 2014. Deposition nucleation viewed as homogeneous or immersion freezing in pores and cavities. *Atmospheric Chemistry and Physics,* 14**,** 2071-2104.

Murray, B. J., O'sullivan, D., Atkinson, J. D. & Webb, M. E. 2012. Ice nucleation by particles immersed in supercooled cloud droplets. *Chemical Society Reviews,* 41**,** 6519-6554.

Nasa & Dunbar, B. 1996. *Atmospheric Aerosols: What Are They, and Why Are They So Important?* [Online]. Available: https://www.nasa.gov/centers/langley/news/factsheets/Aerosols.html [Accessed 16.10. 2017].

Niedermeier, D., Shaw, R. A., Hartmann, S., Wex, H., Clauss, T., Voigtländer, J. & Stratmann, F. 2011. Heterogeneous ice nucleation: exploring the transition from stochastic to singular freezing behavior. *Atmospheric Chemistry and Physics,* 11**,** 8767-8775.

Oxtoby, D. W. 1999. Nucleation and Surface Melting of Ice. *Ice Physics and the Natural Environment***,** 23-38.

Pielke, R. A. 2017. *Atmosphere* [Online]. Encyclopædia Britannica, inc. . Available: https://www.britannica.com/science/atmosphere [Accessed 23.09. 2017].

Pöhlker, C., Huffman, J. A., Förster, J. D. & Pöschl, U. 2013. Autofluorescence of atmospheric bioaerosols: spectral fingerprints and taxonomic trends of pollen. *Atmospheric Measurement Techniques,* 6**,** 3369-3392.

Pottiez, G. 2015. Introduction to Mass Spectrometry. *Mass Spectrometry: Developmental Approaches to Answer Biological Questions.* Springer International Publishing**,** 1-7.

Pruppacher, H. R., Klett, J. D. & Wang, P. K. 1997. *Microphysics of Clouds and Precipitation,* Dordrecht, NL, Kluwer Academic Publishers.

Pummer, B. 2013. *Ice nucleation activity of pollen and fungal spores.* Dissertation, TU Wien.

Pummer, B. G., Bauer, H., Bernardi, J., Bleicher, S. & Grothe, H. 2012. Suspendable macromolecules are responsible for ice nucleation activity of birch and conifer pollen. *Atmospheric Chemistry and Physics,* 12**,** 2541-2550.

Pummer, B. G., Budke, C., Augustin-Bauditz, S., Niedermeier, D., Felgitsch, L., Kampf, C. J., Huber, R. G., Liedl, K. R., Loerting, T., Moschen, T., Schauperl, M., Tollinger, M., Morris, C. E., Wex, H., Grothe, H., Poschl, U., Koop, T. & Frohlich-Nowoisky, J. 2015. Ice nucleation by water-soluble macromolecules. *Atmospheric Chemistry and Physics,* 15**,** 4077-4091.

Ramanathan, V., Crutzen, P. J., Kiehl, J. T. & Rosenfeld, D. 2001. Aerosols, climate, and the hydrological cycle. *Science,* 294**,** 2119-2124.

Rathnayake, C. M., Metwali, N., Jayarathne, T., Kettler, J., Huang, Y., Thorne, P. S., Amp, Apos, Shaughnessy, P. T. & Stone, E. A. 2017. Influence of rain on the abundance of bioaerosols in fine and coarse particles. *Atmospheric Chemistry and Physics,* 17**,** 2459-2475.

Reusch, W. 2013. *Visible and Ultraviolet Spectroscopy* [Online]. Available: https://www2.chemistry.msu.edu/faculty/reusch/virttxtjml/spectrpy/uv-vis/spectrum.htm [Accessed 26.09. 2017].

Schlesinger, W. H. & Bernhardt, E. 2013. *Biogeochemistry: An Analysis of Global Change,* Waltham, USA, Elsevier Inc.

Seinfeld, J. H. & Pandis, S. N. 2006. *Atmospheric Chemistry and Physics: From Air Pollution to Climate Change*, John Wiley & Sons, Inc.

Seutter Von Loetzen, C., Hoffmann, T., Hartl, Maximilian j., Schweimer, K., Schwab, W., Rösch, P. & Hartl-Spiegelhauer, O. 2014. Secret of the major birch pollen allergen Bet v 1: identification of the physiological ligand. *Biochemical Journal,* 457**,** 379-390.

Sigalotti, L. D. G., Klapp, J. & Sira, E. 2014. *Computional and Experimental Fluid Mechanics with Applications to Physics, Engineering and the Environment,* Switzerland, Springer.

Spangfort, M. D., Ipsen, H., Sparholt, S. H., Aasmul-Olsen, S., Larsen, M. R., Mortz, E., Roepstorff, P. & Larsen, J. N. 1996. Characterization of purified recombinant Bet v 1 with authentic N-terminus, cloned in fusion with maltose-binding protein. *Protein Expression and Purification,* 8**,** 365-373.

Swoboda, I., Jilek, A., Ferreira, F., Engel, E., Hoffmann-Sommergruber, K., Scheiner, O., Kraft, D., Breiteneder, H., Pittenauer, E., Schmid, E., Vicente, O., Heberle-Bors, E., Ahorn, H. & Breitenbach, M. 1995. Isoforms of Bet v 1, the Major Birch Pollen Allergen, Analyzed by Liquid Chromatography, Mass Spectrometry, and cDNA Cloning. *Journal of Biological Chemistry,* 270**,** 2607-2613.

Twell, D., Oh, S.-A. & Honys, D. 2006. Pollen Development, a Genetic and Transcriptomic View. *In:* Malhó, R. (ed.) *The Pollen Tube: A Cellular and Molecular Perspective.* Berlin, Heidelberg: Springer Berlin Heidelberg**,** 15-45.

Wesener, J. K. 2005. *UV-Spektroskopie* [Online]. Available: https://roempp.thieme.de/roempp4.0/do/data/RD-21-00864#Literatur [Accessed 03.10. 2017].

Wmo, W. M. O. 1975. *Manual on the observation of clouds and other meteors,* Geneva, Switzerland.

Zachariassen, K. E. & Kristiansen, E. 2000. Ice nucleation and antinucleation in nature. *Cryobiology,* 41**,** 257-279.

8. Appendix

8.1. LC-ESI-MS (Flow through)

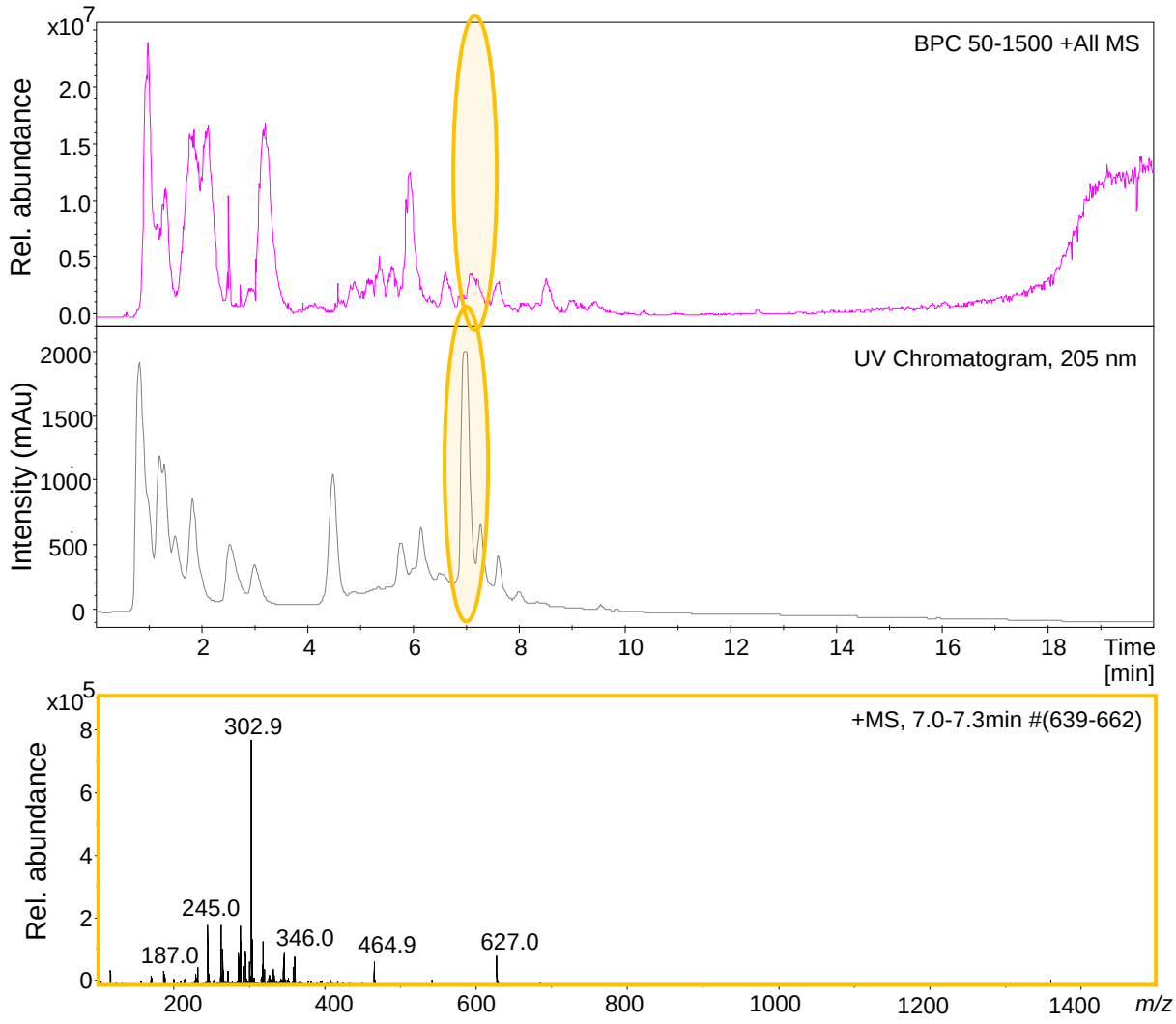

Figure 76: BPC and UV chromatogram recorded with LC of the flow through obtained from SPE as well as the mass spectrum (positive ion mode; method 2, see Table 12) of the substance eluting between 7,0 and 7,3 min. All m/z are singly charged.

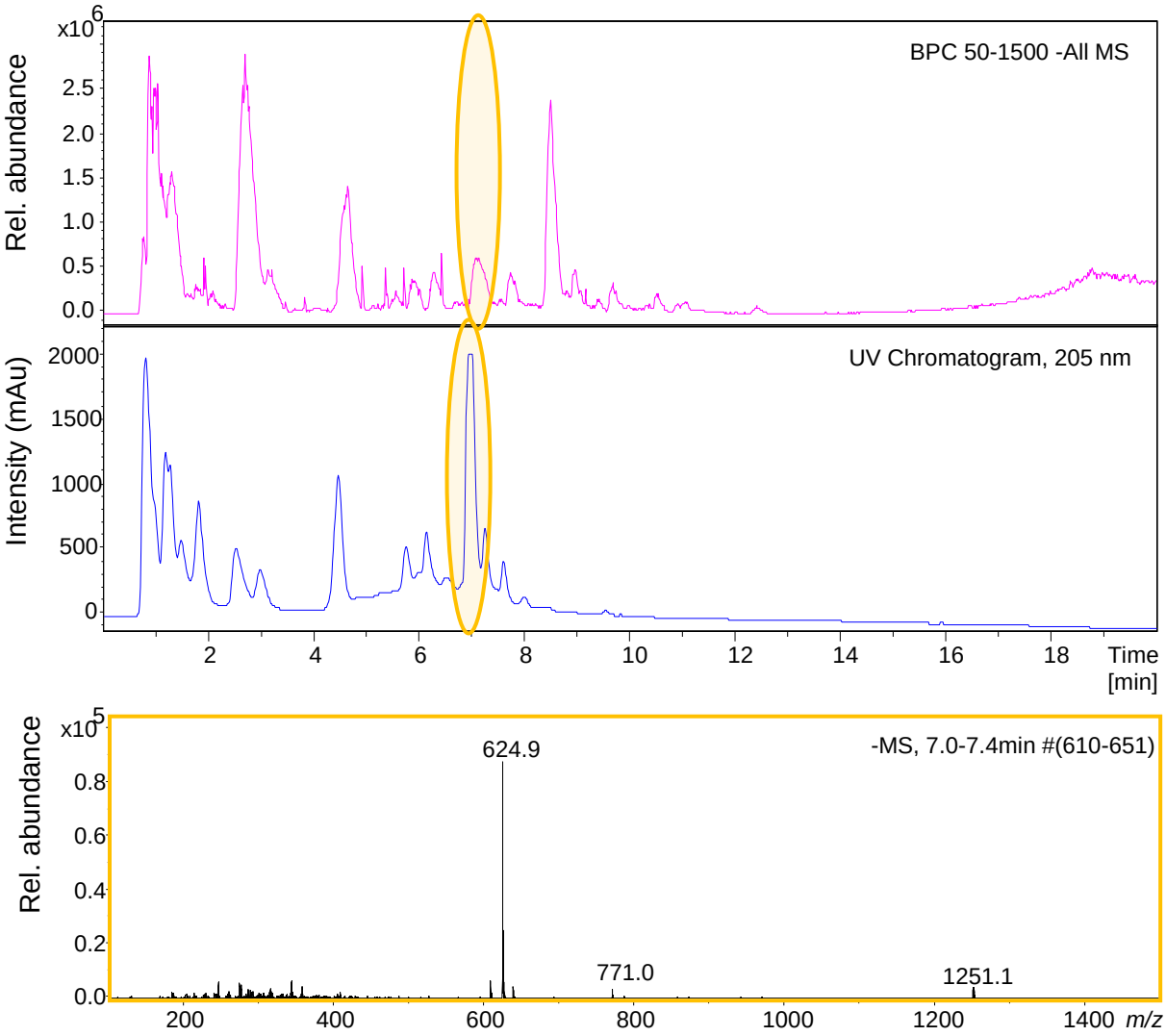

Figure 77: BPC and UV chromatogram recorded with LC of the flow through obtained from SPE as well as the mass spectrum (negative ion mode; method 4, see Table 15) of the substance eluting between 7,0 and 7,4 min. All m/z are singly charged.

8.2. LC-ESI-MS (Filtration samples)

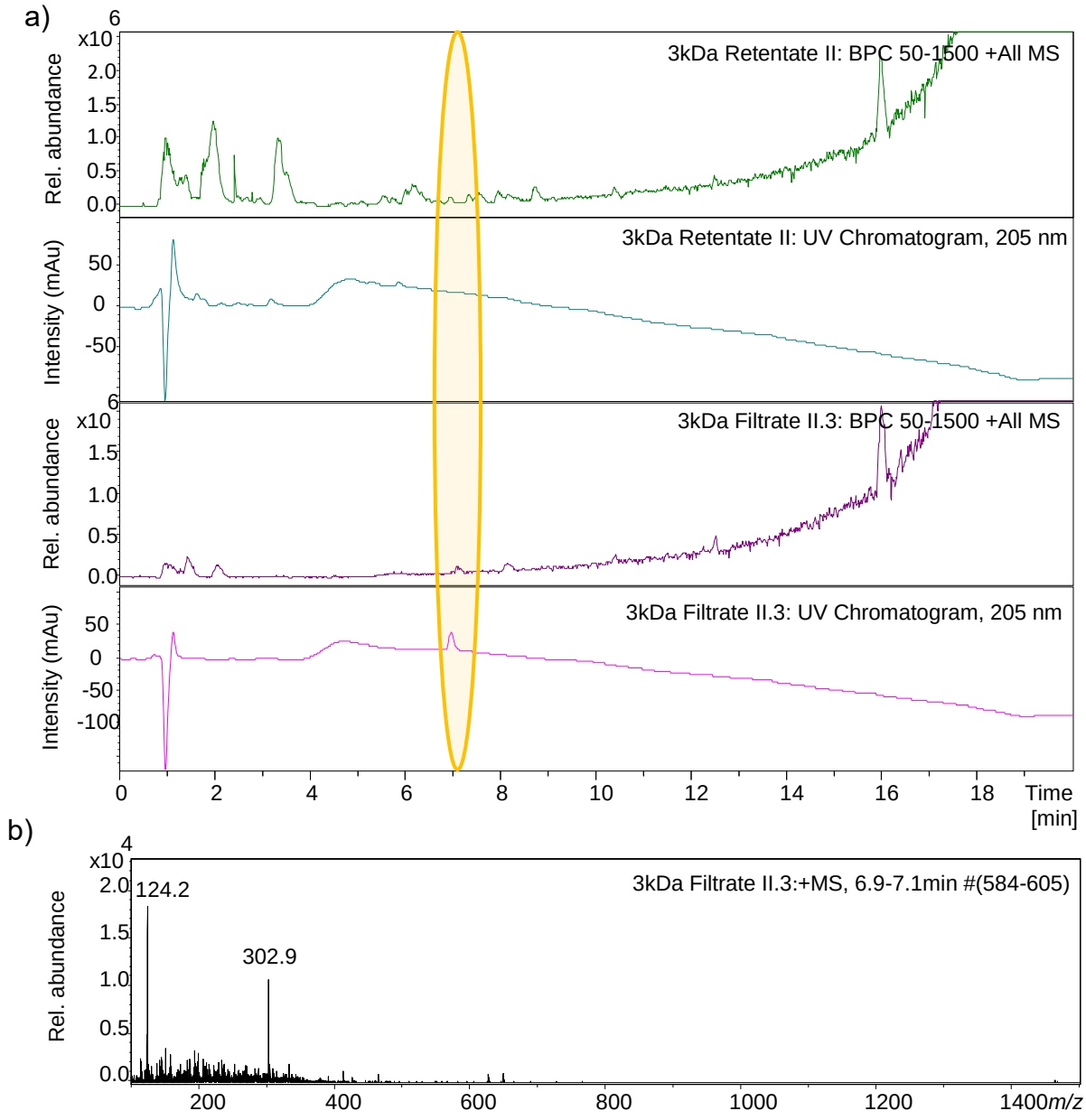

Figure 78: Results from filtrated BP-WW samples measured with LC-ESI-MS (method 2, see Table 13). a) BPC and UV chromatogram recorded with LC of 3 kDa Filtrate II.3 and 3 kDa Retentate II obtained from repeated centrifugal filtration, b) mass spectrum of 3 kDa Filtrate II.3 at a retention time between 6,9 and 7,1 min. All m/z are singly charged.

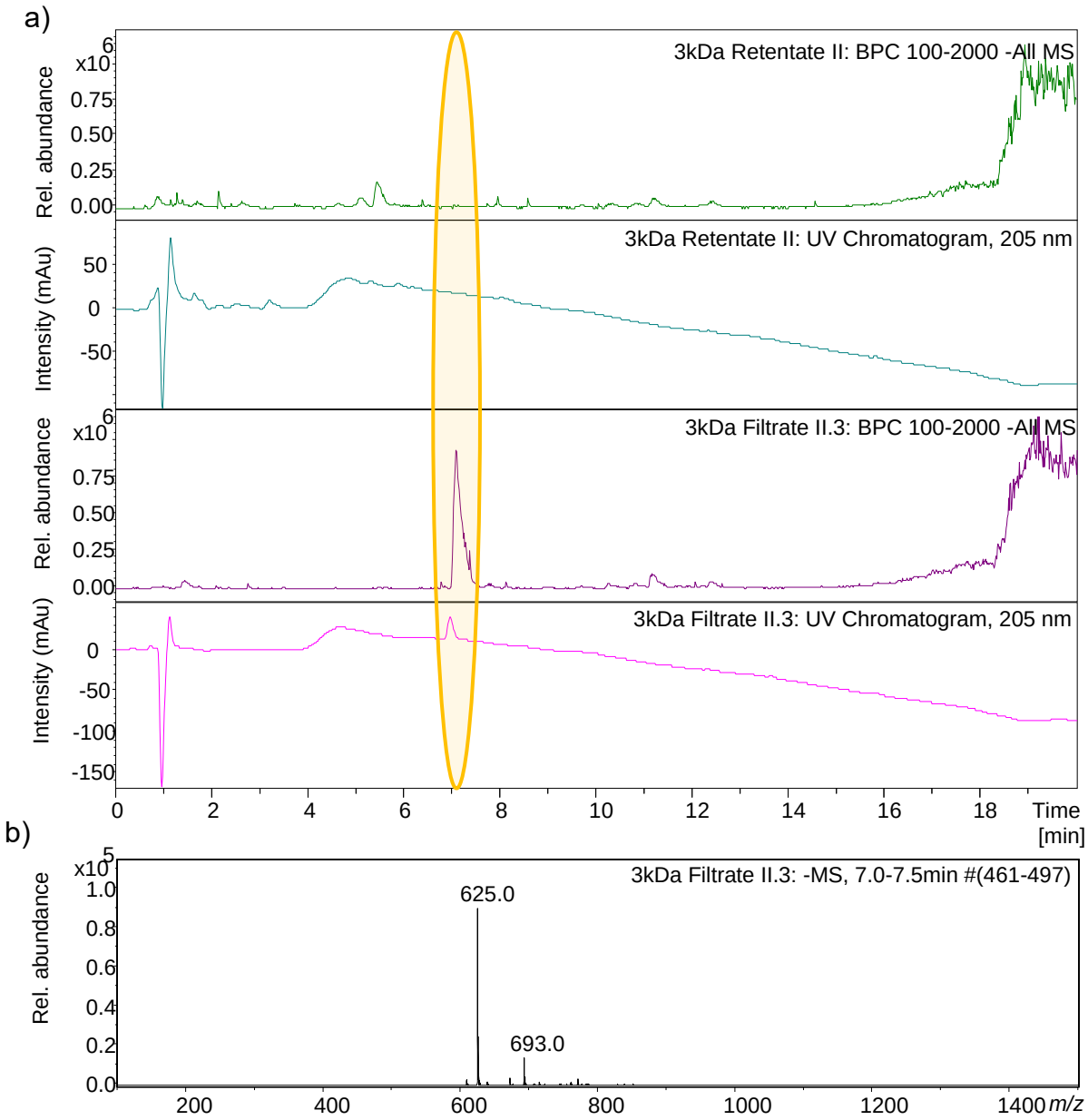

Figure 79: Results from filtrated BP-WW samples measured with LC-ESI-MS (method 3, see Table 14). a) BPC and UV chromatogram recorded with LC of 3 kDa Filtrate II.3 and 3 kDa Retentate II obtained from repeated centrifugal filtration, b) mass spectrum of 3 kDa Filtrate II.3 at a retention time between 7,0 and 7,5 min. All m/z are singly charged.

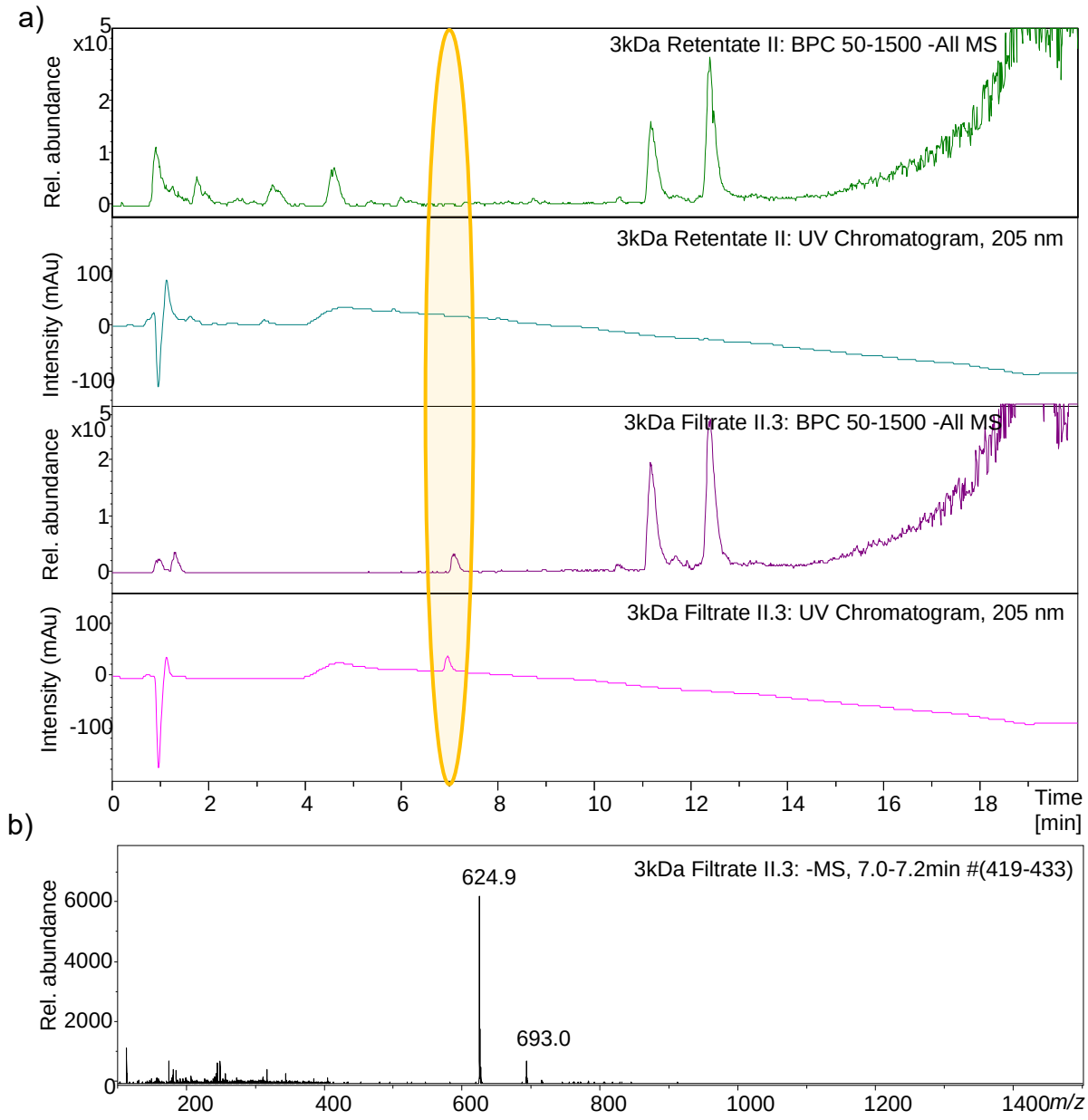

Figure 80: Results from filtrated BP-WW samples measured with LC-ESI-MS (method 4, see Table 15). a) BPC and UV chromatogram recorded with LC of 3kDa Filtrate II.3 and 3kDa Retentate II obtained from repeated centrifugal filtration, b) mass spectrum of 3kDa Filtrate II.3. All m/z are singly charged.